

# **PYROLYSIS OF HERB RESIDUES: THERMOGRAVIMETRIC ANALYSIS AND PELLET LEVEL MODELLING**

**HONGYU ZHU**

Doctor of Philosophy

**ASTON UNIVERSITY**

Mar 2022

© Hongyu Zhu, 2022

Hongyu Zhu asserts their moral right to be identified as the author of this thesis

This copy of the thesis has been supplied on condition that anyone who consults it is understood to recognise that its copyright belongs to its author and that no quotation from the thesis and no information derived from it may be published without appropriate permission or acknowledgement.

# **Declaration**

This thesis is the results of the author's original research. It has been composed by the author and has not been previously submitted for examination, which has led to the award of a degree.

The copyright of this thesis belongs to the author under the terms of the United Kingdom Copyright Acts as qualified by Aston University. Due acknowledgement must always be made of the use of any material contained in, or derived from, this thesis.

## **ACKNOWLEDGEMENTS**

I would like to show my deepest gratitude to my supervisor Dr. Xi Yu and Prof. Anthony V. Bridgewater for giving me the opportunity to undertake the research project and the assistances and guidance from him through each step of the research. I have also received a lot of help and guidance from Dr. Lin Lang from Guangzhou Institute of Energy Conversion and Prof. Junmeng Cai, who is the expert in researching the kinetics model of lignocellulosic biomass pyrolysis. Then, I would like to express my thanks to my parents for their supports and love. They give a lot of encouragement for my research. Finally, a big thank you goes to my friends and colleagues at university for making my time so enjoyable and memorable.

Best wishes to you all,

Hongyu Zhu

Mar 2022

## **PREVIOUSLY PUBLISHED WORK**

Hongyu Zhu, Lin Lang, Gang Fang, Dingying Na, Xiuli Yin, Xi Yu, Chuangzhi Wu, Anthony V. Bridgwater, "Thermogravimetric characteristics and kinetics of herb residues catalyzed by potassium carbonate," *Journal of Analytical and Applied Pyrolysis*, vol. 156, p. 105170, 2021/06/01/ 2021.

Hongyu Zhu, Zhujun Dong, Xi Yu, Grace Cunningham, Janaki Umashanker, Xingguang Zhang, Anthony V. Bridgwater, Junmeng Cai., "A predictive PBM-DEAM model for lignocellulosic biomass pyrolysis," *Journal of Analytical and Applied Pyrolysis*, vol. 157, p. 105231, 2021/08/01/ 2021.

Lin Lang, Hong-yu Zhu, Ying-na Ding, Xiu-li Yin, Chuang-zhi Wu, Xi Yu, and Anthony V. Bridgwater., "Mini-Review on Hot Gas Filtration in Biomass Gasification: Focusing on Ceramic Filter Candles," *Energy & Fuels*, vol. 35, no. 15, pp. 11800-11819, 2021/08/05 2021

## ABSTRACT

A series of alternative energy sources have been exploited to overcome the problem, including the solar energy, wave power, wind power, geothermal heat and so on. Among these energy sources, the biomass fuel has gained a lot of attention. The thermochemical conversion technique of the biomass has been considered as one of the most promising technologies for producing alternative energy fuel, especially the fast pyrolysis process. This thesis describes the experimental and modelling research of the pyrolysis of herb residues in terms of the kinetics analysis and the pyrolysis behaviour of single particle model. The general study of the characteristics of the biomass energy feedstock is reviewed, including the biomass classification and properties, the biomass particle morphology, and the thermochemical conversion behaviour.

The kinetic parameters of the herb residue pyrolysis are studied by the thermogravimetric characteristics. The master plot method is used to investigate the kinetic parameters and the reaction mechanism of herb residues pyrolysis. The optimized parameters are used in the numerical model and verified by experiment data. The catalytic behaviour of Chinese herbal medicine pyrolysis was also investigated by loading different amounts of potassium salts.

The pyrolysis behaviour of single pellet is investigated by experimental and numerical study. The finite volume approach is used for developing the numerical model. The methodology of developing the population balance model and single particle model for pyrolysis are investigated. The population balance approach is not widely applied into modelling the thermochemical conversion of biomass, but this method is good to improve the accuracy of the simulation. This research gives the method of simulating the thermally thick particle model ( $Bi > 1$ ) for fast pyrolysis.

# Table of Contents

|  |    |
|--|----|
| ACKONWLEDGEMENTS .....   | 3  |
| PREVIOUSLY PUBLISHED WORK.....                                     | 4  |
| ABSTRACT.....  | 5  |
| NOMENCLATURE .....   | 13 |
| Chapter 1. Introduction.....                                       | 16 |
| 1.1 Background.....  | 16 |
| 1.2 Biomass thermochemical conversion.....                         | 16 |
| 1.3 Biomass feedstocks.....  | 18 |
| 1.4 Project aim and objectives .....                               | 19 |
| 1.5 Summary of thesis outline.....                                 | 19 |
| Chapter 2. Literature review .....                                 | 21 |
| 2.1 Biomass feedstock.....   | 21 |
| 2.1.1 Classification and application .....                         | 21 |
| 2.1.2 Composition.....   | 23 |
| 2.1.3 Engineering properties .....                                 | 25 |
| 2.1.4 Chinese herb residues.....                                   | 27 |
| 2.2 Biomass particle morphology .....                              | 29 |
| 2.2.1 Particle shape .....   | 29 |
| 2.2.2 Biomass particle size distribution .....                     | 30 |
| 2.2.3 Particle size and shape effect .....                         | 33 |
| 2.3 Biomass thermochemical conversion.....                         | 34 |
| 2.3.1 Overview.....  | 34 |
| 2.3.2 Pyrolysis.....   | 36 |
| 2.4 Nitrogen functionalities.....                                  | 38 |
| 2.4.1 Characteristics of nitrogen functionalities .....            | 38 |
| 2.4.2 Evolution of nitrogen functionalities during pyrolysis ..... | 41 |
| 2.5 Modelling of the thermochemical process the biomass .....      | 43 |
| 2.5.1 Overview.....  | 43 |
| 2.5.2 Reaction mechanisms.....                                     | 46 |
| 2.5.3 Discretization methods.....                                  | 48 |
| 2.5.4 Single particle model .....                                  | 50 |
| 2.5.5 Particle size and shape modelling .....                      | 54 |

|  |     |
|--|-----|
| 2.5.6 Shrinkage simulation of single biomass particle.....   | 55  |
| 2.5.7 Population balance model.....  | 57  |
| Chapter 3.    Thermogravimetric characteristics and kinetics analysis.....                                     | 59  |
| 3.1 Introduction.....  | 59  |
| 3.2 Experiment preparation and materials.....  | 60  |
| 3.3 Research method.....   | 61  |
| 3.3.1 Thermogravimetric analysis.....  | 61  |
| 3.3.2 Kinetic parameter study.....   | 61  |
| 3.4 Results and discussion.....  | 64  |
| 3.4.1 Thermogravimetric analysis.....  | 64  |
| 3.4.2 Activation energy.....   | 67  |
| 3.4.3 Reaction model and pre-exponential factor.....   | 71  |
| 3.5 Validation and conclusion.....   | 77  |
| Chapter 4.    Evolution mechanism of N-containing species of product char during pyrolysis<br>of biomass    80 |     |
| 4.1 Introduction.....  | 80  |
| 4.2 Research method.....   | 80  |
| 4.2.1 Materials.....   | 80  |
| 4.2.2 Experimental setup.....  | 80  |
| 4.2.3 X-ray Photoelectron Spectroscopy (XPS) analysis method.....  | 81  |
| 4.3 Results and discussion.....  | 82  |
| 4.4 Conclusion and recommendation.....   | 88  |
| Chapter 5.    Modelling and experimental study of single large herb residue particle during<br>pyrolysis    89 |     |
| 5.1 Introduction.....  | 89  |
| 5.2 Materials and experimental methods.....  | 89  |
| 5.2.1 Material properties.....   | 89  |
| 5.2.2 Experimental approach.....   | 90  |
| 5.3 Numerical model.....   | 92  |
| 5.3.1 Model description.....   | 92  |
| 5.3.2 Mass and energy conservation.....  | 93  |
| 5.3.3 Finite volume approach.....  | 95  |
| 5.4 Results and discussion.....  | 96  |
| 5.4.1 Mass loss.....   | 96  |
| 5.4.2 Temperature distribution.....  | 98  |
| 5.5 Conclusions.....   | 102 |

|  |     |
|--|-----|
| Chapter 6. Modelling the pyrolysis process of single biomass particle with a size distribution | 103 |
| 6.1 Introduction.....  | 103 |
| 6.2 Particle size distribution.....  | 103 |
| 6.2.1 Monte Carlo sampling method.....   | 103 |
| 6.2.2 Particle size distribution of real case.....   | 105 |
| 6.3 Single particle model .....  | 107 |
| 6.3.1 Model description – spherical particle .....   | 107 |
| 6.3.2 Mass and energy conservation during pyrolysis process .....                              | 108 |
| 6.3.3 Intraparticle heat transfer model .....  | 110 |
| 6.3.4 DAEM model.....  | 111 |
| 6.3.5 Results and discussion .....   | 112 |
| 6.3.6 Validation and Conclusion.....   | 120 |
| Chapter 7. Conclusion and Recommendation.....  | 122 |
| 7.1 Conclusions.....   | 122 |
| 7.2 Future work plan .....   | 124 |
| References.....  | 124 |

## List of Figures

|   |    |
|---|----|
| Figure 1-1: Thermochemical conversion processes [8]. .....  | 17 |
| Figure 1-2: Required volume of each renewable resources with same energy content [8].....   | 18 |
| Figure 2-1: Lignocellulose structure [45]. .....  | 24 |
| Figure 2-2: Engineering properties [36, 47].....  | 25 |
| Figure 2-3: The production flow diagram of Chinese herb medicine and CHR [70]. .....  | 28 |
| Figure 2-4: Different shapes of original lignocellulosic biomass from image analysis [78]. ..   | 29 |
| Figure 2-5: Micrographs of grinding biomass particles from different biomass feedstock [77].<br>.....   | 29 |
| Figure 2-6: Particle model geometries used in numerical simulations of heat and mass transfer [80]......  | 30 |
| Figure 2-7: Microscale visualization of woody biomass [82]. (a) Coniferous tree; (b) Section of a pine trunk; (c) Microcellular structure of wood tissue; (d) Micrograph of cell wall with various layers; (e) The nanoscale arrangement of biopolymers within the cell wall; (f) Micrograph of amorphous lignin polymer and a cellulose fibril; (g-i) X-ray computed topography reconstruction of a milled pine particle 0.5mm. .... | 31 |



|   |    |
|---|----|
| Figure 2-8: Cumulative particle size distribution Q3 (%), for different kinds of biomass feedstock (poplar, pulverized wood and wheat straw) and sieving methods: Sieving, 2D dynamic imaging, laser diffraction and FBRM (focused beam reflectance technique) [79]. .. | 32 |
| Figure 2-9: Heat-up time of single particle vs weighted distributed particles [83]. .....   | 33 |
| Figure 2-10: Imaging shape of biomass particles [84]. .....   | 34 |
| Figure 2-11: (a) Process rates of moisture content, devolatilization and char burn out. Mass loss history, max and min temperature inside particle [66]. (b) Single particle conversion steps. .  | 34 |
| Figure 2-12: Schematic description of the biomass temperature distribution [81]. .....  | 35 |
| Figure 2-13: Pyrolysis reaction path of woody biomass [98]. .....   | 37 |
| Figure 2-14: Distribution of N in pyrolysis product as a function of temperature [114]. .....   | 39 |
| Figure 2-15: XPS N 1s spectra of N-containing groups in pyrolysis char product (a), .....   | 40 |
| Figure 2-16: N 1s XPS nitrogen spectra of coal samples produced by pyrolysis at different temperature [123]. .....  | 41 |
| Figure 2-17: N 1s XPS spectra of spirulina platensis samples produced by pyrolysis at different temperature [114]. .....  | 42 |
| Figure 2-18: Modelling scales of biomass conversion. ....   | 44 |
| Figure 2-19: Comparison of different simulation models in terms of accuracy and computing time [130]. .....   | 45 |
| Figure 2-20: Wave-like character. Isotherms [K]. (Solid lines, step number=50; Dashed lines, constant contour level of temperature variable $\eta$ ) [168]. .....   | 54 |
| Figure 2-21: Particle shape evolution [162]. .....  | 55 |
| Figure 2-22: Particle evolution mechanisms [172]. .....   | 57 |
| Figure 3-1: TG curves of herb samples with different $K_2CO_3$ loadings at (a)10 K/min (b)20 K/min (c) 30 K/min (d) 40 K/min. ....  | 64 |
| Figure 3-2: DTG curves of herb samples with different $K_2CO_3$ loadings at (a)10 K/min (b)20 K/min (c) 30 K/min (d) 40 K/min. ....   | 66 |
| Figure 3-3: DTG profile and DDTG profiles of the devolatilization stage of CHR samples with different $K_2CO_3$ loadings at 20 K/min. (Section I & II belong to the main devolatilization phase) .....  | 67 |
| Figure 3-4: Kinetic plots of apparent activation energy as a function of conversion via Starink method. (a)Herb (b)Herb-5%K (c) Herb-7%K (d) Herb-9%K .....   | 69 |
| Figure 3-5: Variation of the thermal activation energy and the value of $R^2$ . .....   | 69 |
| Figure 3-6: Experimental and theoretical master-plots of the CHR samples with different $K_2CO_3$ . .....   | 72 |
| Figure 3-7: Linear fitting model of $y = \ln Pu - \ln \beta RE \alpha$ against $x = \ln [1 - 1 - \alpha/3]$ . ....  | 73 |

|   |     |
|---|-----|
| Figure 3-8: Calculated TG curves based on the D <sub>n</sub> -Jader model compared with experimental data at various heating rates. ....  | 78  |
| Figure 4-1: Schematic diagram of the experimental system. ....  | 81  |
| Figure 4-2: N 1s XPS spectra of CHR at different temperature. ....  | 82  |
| Figure 4-3: N 1s XPS spectra of BS at different temperature. ....   | 83  |
| Figure 4-4: N 1s XPS spectra of BS-15pc at different temperature. ....  | 84  |
| Figure 4-5: Relative N content of N-species for CHR at different temperatures. ....   | 86  |
| Figure 4-6: Relative N content of N-species for BS at different temperatures. ....  | 87  |
| Figure 4-7: Relative N content of N-species for BS-15pc at different temperatures. ....   | 87  |
| Figure 5-1: Schematic diagram of herb particle pyrolysis system. (1) Nitrogen; (2) Flowmeter; (3) Thermocouple; (4) Herb residue particle; (5) Reactor; (6) Condenser; (7) Temperature acquisition device. .... | 90  |
| Figure 5-2: The schematic diagram of single particle pyrolysis experimental setup and measurement points. ....  | 91  |
| Figure 5-3: Theoretical heating curve of experimental sampling point. ....  | 91  |
| Figure 5-4: Schematic of division of cylinder particle. ....  | 95  |
| Figure 5-5: Experimental data of mass loss rate. ....   | 98  |
| Figure 5-6: Cross sectional Contour plot of temperature distribution inside the particle at different pyrolysis temperature and measuring time. ....  | 99  |
| Figure 5-7: Temperature evolution of the model as a function of time (surface and centre temperature). ....   | 100 |
| Figure 5-8: Predicted and measured centre temperature and the surface temperature of particle. ....   | 100 |
| Figure 5-9: Radial temperature distribution against particle radius at different time. ....   | 101 |
| Figure 5-10: Axial temperature distribution against particle length at different time. ....   | 102 |
| Figure 6-1: Monte Carlo sampling code. ....   | 105 |
| Figure 6-2: Size distribution of ground biomass particles from Douglas fir wood [213]. ....   | 105 |
| Figure 6-3: Schematic of intra-particle heat transfer. ....   | 110 |
| Figure 6-4: Mathematica code of average volume temperature. ....  | 110 |
| Figure 6-5: Particle size sampling from a normal distribution ( $\mu_p=1000\mu\text{m}$ , $\sigma_p=200$ ). ....  | 112 |
| Figure 6-6: Biot number against particle diameter. ....   | 113 |
| Figure 6-7: Mass loss rate predicted from two different models (d=1.03mm, 773K): (a) Non-isothermal model with DAEM; (b) Non-isothermal model without DAEM. ....  | 114 |
| Figure 6-8: Influence of temperature on mass loss rate predicted from non-isothermal model with DAEM (1.03mm). ....   | 114 |

|  |     |
|--|-----|
| Figure 6-9: the extent of size reduction at different time periods for whole particle population (non-isothermal model with DAEM).....   | 115 |
| Figure 6-10: Contour plot of radial temperature distribution over time at different Biot number. ....  | 116 |
| Figure 6-11: Particle diameter and porosity variation for different particles: $d=0.59\text{mm}$ ( $Bi<1$ ), $d=0.74\text{mm}$ ( $Bi=1$ ), $d=1.31\text{mm}$ ( $Bi>1$ ) at 773K. (a)Non-isothermal with DAEM. (b) Non-isothermal model without DEAM..... | 116 |
| Figure 6-12: Temporal evolution of particle size distribution at 773K. (a)Non-isothermal with DAEM. (b) Non-isothermal model without DEAM. ....  | 117 |
| Figure 6-13: Temperature at centre of particle at pyrolysis temperature of 773K. (a)Non-isothermal with DAEM. (b) Non-isothermal model without DEAM. ....  | 117 |
| Figure 6-14: Effect of pyrolysis temperature on temperature of Centre of Particles after 1 Second. (a)Non-isothermal with DAEM. (b) Non-isothermal model.....  | 118 |
| Figure 6-15: Percentage of PSD to complete heating up process predicted from different models under temperature. (a)Non-isothermal with DAEM. (b) Non-isothermal model.....  | 119 |
| Figure 6-16: Heat up time under different surrounding temperature. (a)Non-isothermal with DAEM. (b) Non-isothermal model. ....   | 119 |
| Figure 6-17: Comparison of heating up time prediction between single and distributed particle size using different kinetics models. ....   | 119 |
| Figure 6-18: Comparison of heating up time prediction between single and distributed particle size under different temperature. ....   | 120 |
| Figure 6-19: Particle surface temperature. Experiment data obtained from [222].( $d=20\text{mm}$ , 773K). ....   | 121 |
| Figure 6-20: Residue mass fraction ( $d=20\text{mm}$ , 773K). Experimental data from Huang et al. [222]. Ultimate analysis data obtained from Sadhukhan et al.[134]. ....  | 121 |
| Figure 6-21: Size reduction comparison. Shrinkage model from: Huang et al. [222] and Yang et al. [129].....  | 122 |

## List of Tables

|   |    |
|---|----|
| Table 2-1: Biomass classification and related conversion types [35, 36]. ....             | 21 |
| Table 2-2: Different shapes of woody biomass.....   | 22 |
| Table 2-3: Typical lignocellulose content of some lignocellulosic biomass feedstock. .... | 23 |
| Table 2-4: Changed properties of biomass in different process [56, 57]. ....              | 27 |
| Table 2-5: Multiscale biomass composition [36]. ....                                      | 32 |

|   |     |
|---|-----|
| Table 2-6: Pyrolysis modes and product yield [9, 38, 94-97].  | 36  |
| Table 2-7: N content of different biomass fuel [109-113].   | 39  |
| Table 2-8: Pyrolysis kinetic models [32, 101, 136-138].   | 47  |
| Table 2-9: Discretization methods.  | 50  |
| Table 2-10: Considered biomass particle morphology in selected single particle models. ....                               | 52  |
| Table 2-11: Summary of single particle model volume shrinkage factor.   | 56  |
| Table 3-1: Proximate and ultimate analyses of herb.   | 60  |
| Table 3-2: Symbol meanings.   | 61  |
| Table 3-3: Ten different widely used mechanism functions of solid-state reaction models [187].<br>.....                   | 63  |
| Table 3-4: Normalized mass loss of CHR with different K <sub>2</sub> CO <sub>3</sub> loadings determined by TGA.<br>..... | 65  |
| Table 3-5: Calculation results of the thermal activation energy of herb samples by Starink<br>method.....                 | 70  |
| Table 3-6: The calculation results of herb samples (D <sub>n</sub> coefficient and pre-exponential factor).<br>.....      | 72  |
| Table 3-7: Calculation data of fitting model for original herb sample.....  | 73  |
| Table 3-8: Calculation data of fitting model for herb-5% K sample. ....   | 74  |
| Table 3-9: Calculation data of fitting model for herb-7% K sample. ....   | 75  |
| Table 3-10: Calculation data of fitting model for herb-9% K sample. ....  | 76  |
| Table 4-1: The areas of each N-species of CHR at different temperature. ....  | 85  |
| Table 4-2: The areas of each N-species of BS at different temperature .....   | 85  |
| Table 4-3: The areas of each N-species of BS-15pc at different temperature. ....  | 86  |
| Table 5-1: Proximate and ultimate analysis (Dried at 105 °C) [182].   | 89  |
| Table 5-2: Selection of particles using in experiment.....  | 89  |
| Table 5-3: The change of the geometry of the herb residue particles.....  | 92  |
| Table 5-4: Properties and kinetic data.....   | 94  |
| Table 5-5: Experimental results of the geometrical parameters.....  | 97  |
| Table 6-1: Sieved particle sizes, corresponded retained fraction, and cumulative fraction. ...                            | 106 |
| Table 6-2: Proximate analysis and the ultimate analysis of the biomass material. ....                                     | 108 |
| Table 6-3: Properties and kinetic data.....   | 109 |

## NOMENCLATURE

### Roman symbols

|              |  |
|--------------|--|
| A            | Pre-exponential factor                             |
| E            | Activation energy                                  |
| $E_{\alpha}$ | Apparent activation energy                         |
| $E_0$        | Average activation energy                          |
| R            | Universal gas constant                             |
| x            | Thickness of the reaction zone                     |
| $\Delta t$   | Time step  |
| $\Delta m$   | Mass variation                                     |
| n            | Kinetic coefficient                                |
| d            | Diameter of particle                               |
| g            | Gravity acceleration                               |
| $F_N$        | Relative content of different N-containing species |
| $A_N$        | Area of each peak                                  |
| p            | Static pressure                                    |
| D            | Diameter   |
| H            | Height   |
| m            | Mass   |
| $\varphi_0$  | Initial porosity                                   |
| $\varphi$    | Porosity   |
| r            | Radius direction of the particle                   |
| $V_p$        | Particle volume                                    |
| $k_{eff}$    | Effective conductivity                             |

|            |   |
|------------|---|
| $k$        | Thermal conductivity                                    |
| $X_M$      | Mass fraction of moisture                               |
| $X_V$      | Mass fraction of volatile                               |
| $X_C$      | Mass fraction of char                                   |
| $\Delta H$ | Reaction heat   |
| $C_p$      | Heat capacity   |
| $L_p$      | Characteristic length                                   |
| $Bi$       | Biot number   |
| $N_x$      | Division number   |
| $Y$        | Char formation rate                                     |
| $k$        | Rate constant   |
| $h$        | External heat transfer coefficient                      |
| $L_p$      | Characteristic length of particle                       |
| $T_c$      | Temperature of particle centre                          |
| $T_s$      | Temperature of particle surface                         |
| $T_p$      | Particle temperature                                    |
| $t$        | Reaction time   |
| $D$        | Strain tensor   |
| $I$        | Identity tensor   |
| $q$        | Conductive heat flux                                    |
| $H$        | Heat generated from reactions                           |
| $R_g$      | Mass transfer source term due to the pyrolysis reaction |
| $U$        | Velocity vector   |

### Greek symbols

|             |   |
|-------------|---|
| $\mu$       | Dynamic viscosity                                     |
| $\rho$      | Density   |
| $\eta$      | Ratio of the current biomass mass to the initial mass |
| $\mu$       | Mean value of normal distribution                     |
| $\sigma$    | Standard deviation of normal distribution             |
| $\sigma$    | Stefan-Boltzmann constant                             |
| $v$         | Volatile production rate                              |
| $\alpha$    | Conversion rate                                       |
| $f(\alpha)$ | Differential mechanism function                       |

|                   |                               |
|-------------------|-------------------------------|
| $G(\alpha)$       | Integrated mechanism function |
| $\omega$          | Pore emissivity               |
| $l_{\text{pore}}$ | Pore size                     |
| $\beta$           | Heating up rate               |

### Abbreviations

|      |                                     |
|------|-------------------------------------|
| BS   | Bamboo shoot shell                  |
| CHR  | Chinese herb residue                |
| PBM  | Population Balance Model            |
| AR   | Aspect Ratio                        |
| PBE  | Population Balance Equation         |
| MC   | Monte Carlo                         |
| TG   | Thermogravimetry                    |
| TGA  | Thermogravimetric Analyzer          |
| DTG  | Derivative thermogravimetry         |
| XPS  | X-ray Photoelectron Spectroscopy    |
| SFOR | Single first order reaction         |
| DAEM | Distributed activation energy model |

## **Chapter 1. Introduction**

### **1.1 Background**

As the growth of the population, the requirement of energy has increased rapidly. The lack of the fossil fuel becomes a worldwide problem. One of the world Sustainable Development Goals (SDGs) is to make sure that the world can access to the reliable and clean energy. Now, the major fuel source in the world is the fossil fuels [1]. According to the survey of the U.S. Energy Information Administration, the global energy consumption is expected to rise to around 736 quadrillion BTU by 2040 [2]. Currently, the major global fuel source is the fossil fuels [1]. Fossil fuels are not only the key for producing heat and electricity, but the crude oil can be used as a feedstock of other valuable products. As the increasing energy demand, the lack of the fossil fuels and the increasing carbon emission become crucial worldwide problem [3, 4]. A series of alternative energy sources are investigated by researchers, including solar energy, wave power, wind power, tidal energy, geothermal heat, biomass energy and so on [5].

Biomass energy, which can be obtained from organic material, is regarded as one of the most promising form of renewable energy and it can reduce the impact of energy utilization on nature environment [6]. The use of biomass as an energy source to fulfil the majority of global fuel requirements has a long history, until the advent of the fossil fuels era has eventually led to their phasing out in many countries [7]. After the industrial revolution, the fossil fuel gradually replaced the biomass energy in industrial application. Currently, the sustainability of the biomass makes it gain particular interest as an alternative energy source. The advantage of biomass over other renewable energy sources is that it is the only potential source of solid, liquid and gaseous fuels, while others produce heat and power directly [8].

### **1.2 Biomass thermochemical conversion**

The biomass thermochemical conversion is the most popular technology for producing the biofuels, especially the fast pyrolysis process [9]. Through different conversion processes, the



fuel energy will be produced from biomass materials. Three main products will be produced by biomass conversion: solid (bio-char), liquid fuel (bio-oil) and syngas [6]. The liquid fuel is more popular than the other states, since it is easy to be stored and transported, and contain high-energy content. It is found that the production of biofuel depended on the operating technologies and the process parameters. Recent studies found that the biomass conversion efficiency mainly influenced experiment operation parameters, biomass feedstock properties, reaction conditions, economic factor and other factors [10, 11]. The reaction conditions include the reaction temperature, residence time, heating rate and reaction pressure. The operation parameters consist of reactor parameters, inlet gas type and gas flow rate. The biomass properties include biomass type, particle size and engineering properties. There are various approaches to convert biomass feedstock into bioenergy form (Figure 1-1). The thermochemical conversion process of biomass is concerned as the most promising technology for producing the renewable biofuels, especially the fast pyrolysis process. Pyrolysis occurs when the heating temperature at about 500°C in the absence of air and three states of products exist in this condition together [8]. Combustion is the most commonly form used in industrial-scale, while the gasification process remains in pilot-scale [12]. For the combustion process, the hot gas produced at around 800-1000°C temperature. Gasification occurs at around 800-900°C and syngas produced in this stage. The production yields of the biochar, bio-oil and gases from pyrolysis largely depend on the operation conditions of the experiment, the reactor characteristics and the biomass feedstock [8].

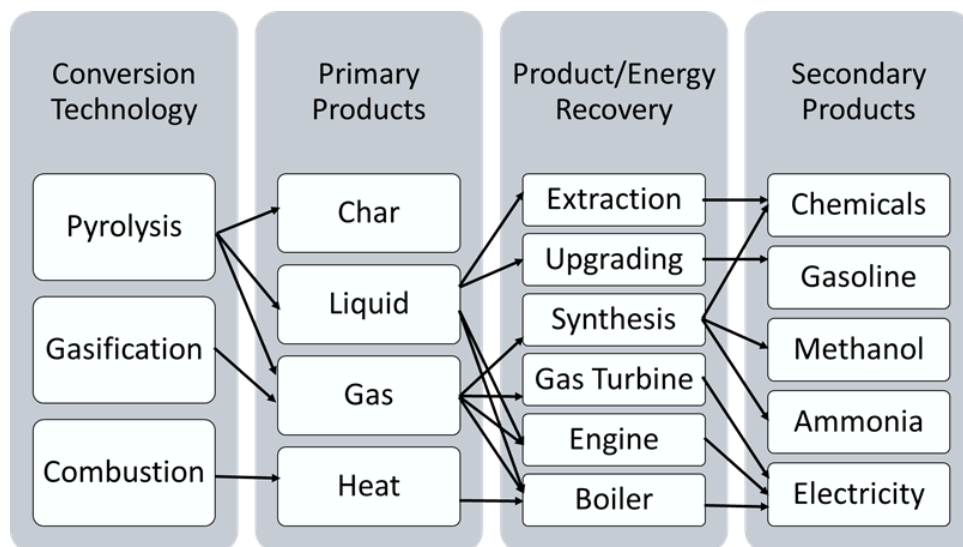


Figure 1-1: Thermochemical conversion processes [8].

The whole biomass-biofuel process including the biomass feedstock selection, storage and transportation, pre-treatment, reactor and product selection and application. In order to obtain higher energy density, appropriate pre-treatment should be applied to the raw biomass feedstock.

Figure 1-2 shows a comparison of the energy content between different renewable energy sources. It is obvious that the wood pellets show high-energy content compared with the other solid materials. Thus, appropriate pre-treatment methods should be applied to the raw biomass feedstock to obtain higher energy density. Pre-treatment, which occupies nearly half of the total cost of processing, is an indispensable step for the biomass-to-energy process [13]. The main goals of this process are saving operation costs and reducing research difficulties [14]. It can break down the original structure of the biomass and make the properties of the material fit to the processing equipment. Three different biomass pre-treatment methods (biological, physical and physiochemical) are concluded in the literature review. Understanding the mechanisms of biomass pre-treatment methods helps selecting the optimal pre-treatment process for different raw materials efficiently [15].

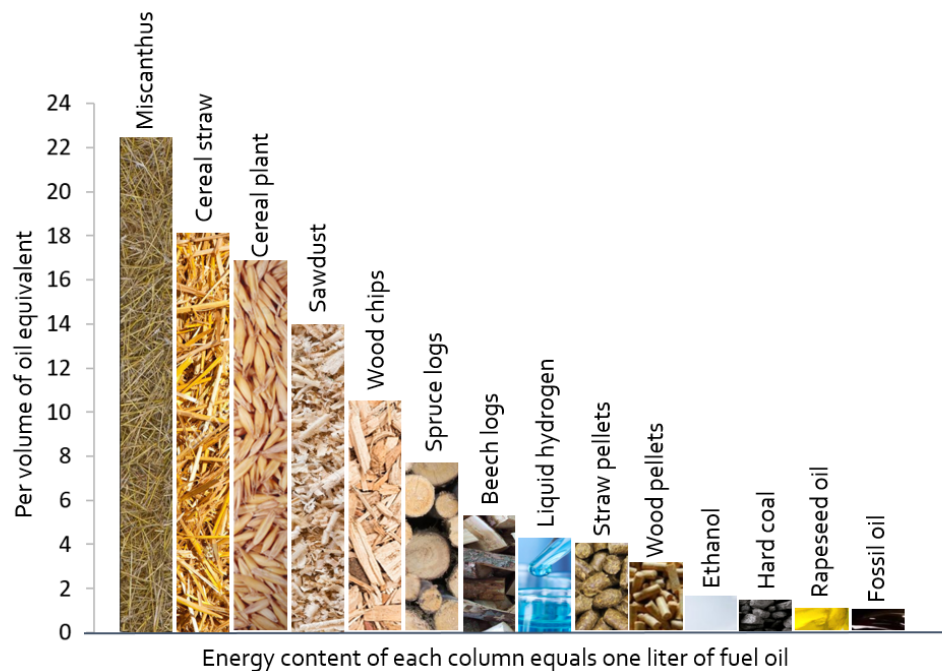


Figure 1-2: Required volume of each renewable resources with same energy content [8].

### 1.3 Biomass feedstocks

Biomass feedstocks have diverse characteristics, including the diversity of particle shape, multi-scale size and various engineering properties. Particle shape and size distribution directly affect the heating-up rate and conversion efficiency [16-18]. These features not only increase the cost of experiment operation and energy consumption, but also give obstruction to the subsequent conversion process study [19]. A number of biomass conversion research use spherical or cylindrical shape with uniform size in numerical simulation to study the biomass conversion efficiency [16, 20-22]. The intra-particle behaviour of biomass particles vary with particle shape, size distribution and feedstock type, however, the effect of porosity and asymmetric nature of

biomass particles on the intra-particle heat transfer properties are not generally considered into the current researches [23]. Recent studies found that the biomass conversion efficiency mainly influenced experiment operation conditions, biomass feedstock properties, reaction conditions, economic factor and other factors [24]. After the normalized pre-treatment process, the biomass particles show a size distribution instead of uniform size and exhibit anisotropic characteristics [25]. Park et al. [26] studied the effects of the surrounding environment on the conversion efficiency using thermogravimetric analysis (TGA) method. They found that the production of biofuel depended on the operating technologies and the process parameters. The particle size will affect the intra-particle heat transfer behaviour directly, while the effect of the asymmetric nature and porosity of the biomass particles is not obvious [23]. The internal heat transfer performance is not easy to be captured experimentally since the fast conversion and the high reaction temperature. Computational modelling method is popular in monitoring the biomass intra-particle heat and mass transfer, since it can capture the rapid reactions [27]. The biomass single particle kinetic models and process models have been developed in many research [28-34].

## 1.4 Project aim and objectives

The aim of this work is to improve and extend the investigation of the pyrolysis characteristics of herb residues through the kinetics analysis method and the particle modelling method. Several key objectives are:

- Investigate the thermogravimetric characteristics and kinetics parameters of CHR pyrolysis. The catalytic behaviour of the CHR pyrolysis is also studied.
- Research the effect of particle morphology on the heat and mass transfer behaviour within particles during pyrolysis process.
- Investigate the effect of operation conditions of pyrolysis process and building up a model framework to predict the heat and mass transfer behaviour during pyrolysis.

## 1.5 Summary of thesis outline

The outline of this thesis with a brief description of each chapter is provided:

**Chapter 2.** This chapter presents a literature review of biomass sources, biomass particle morphology, nitrogen functionalities of biomass, biomass pyrolysis and modelling of biomass pyrolysis.

**Chapter 3.** This chapter introduces the experimental and numerical study of thermogravimetric characteristics of herb residue pyrolysis. The kinetic parameters (activation energy, kinetic

coefficient, and pre-exponential factor) are investigated using Kinetic-free method and master plot method. The herb residues are loaded with different amounts of  $K_2CO_3$  to study the effect of catalyst on the pyrolysis behaviour of herb residues. The obtained parameters are validated by experimental data.

**Chapter 4.** This chapter investigates the evolution mechanism of Nitrogen containing species in the product char during pyrolysis process. The X-ray Photoelectron Spectroscopy (XPS) characterization method is used to study the regulation mechanism of N-containing species of char product.

**Chapter 5.** This chapter provides an experimental and modelling method of single pellet pyrolysis process. A three-dimensional cylinder pellet is modelled to investigate the pyrolysis behaviour. The finite volume approach is used in the simulation.

**Chapter 6.** This chapter provides a model framework, which is able to simulate the pyrolysis process of biomass with a size distribution. The model could be used in predicting the intra-particle temperature distribution at each time step. The influence of particle size on the heat and mass transfer behaviour during pyrolysis are investigate.

**Chapter 7.** This final chapter displays the main conclusions for the results of this Phd work, Then, the suggestion and recommendations for future work are given at last.

## Chapter 2. Literature review

### 2.1 Biomass feedstock

#### 2.1.1 Classification and application

The National Energy Education Development (NEED) project divided the biomass energy into four sorts: wood and agricultural wastes, solid wastes, landfill gas and biogas, and alcohol fuels [35]. The basic biomass conversion types were concluded by Cai et al. [36]: thermochemical conversion (combustion, pyrolysis, gasification and liquefaction) and biochemical conversion (anaerobic digestion and fermentation). The biomass refers to all the organic matter produced through photosynthesis or plant stems, including various organic materials: woods, agricultural or industrial wastes [37]. The main products of the thermochemical conversion are in three states: liquid (bioethanol, bio-oil, digestate and biodiesel), solid (char) and gas (biogas, fuel gas and syngas). Table 2-1 summarises the basic classification of biomass materials and main products.

*Table 2-1: Biomass classification and related conversion types [35, 36].*

| Categories                  | Sources                                 | Conversion   | Production        | Application          |
|-----------------------------|---|--------------|-------------------|----------------------|
| Wood and agricultural waste | Wood residues and agricultural residues | Combustion   | Gas               | Heat/Power           |
|                             |   | Pyrolysis    | Bio-oil           | Heavy oil substitute |
|                             |   |              | Char              | Refinery products    |
|                             |   |              | Fuel gas          | Fuel gas             |
|                             |   | Gasification | Syngas            | Heat/Power           |
|                             |   |              |                   | Synthesis products   |
|                             |   | Liquefaction | Liquefied biomass | Heavy oil substitute |
|                             |   |              |                   | Refinery products    |
|                             |   |              | Fuel gas          | Fuel gas             |
|                             | Crops                                   | Fermentation | Bioethanol        | Transportation       |

|                        |                            |                               |                |                        |
|------------------------|----------------------------|-------------------------------|----------------|------------------------|
|                        |                            |                               |                | fuel                   |
|                        |                            |                               |                | Refinery products      |
|                        |                            |                               | Lignin residue | Heat/Power             |
|                        | Animal farming             | Anaerobic digestion           | Biogas         | Heat/Power             |
|                        |                            |                               |                | Natural gas substitute |
|                        |                            |                               |                | Transportation gas     |
|                        |                            |                               | Digestate      | Organic fertilizer     |
| Solid waste            | Household garbage          | Thermochemical conversion     | Fuel gas       | Heat/Power             |
| Landfill gas or biogas | Microorganism              | Anaerobic digestion           | Biogas         | Heat/Power             |
|                        |                            |                               |                | Natural gas substitute |
|                        |                            |                               | Digestate      | Transportation gas     |
| Alcohol fuels          | Organic material in plants | Fermentation and distillation | Bioethanol     | Transportation fuel    |
|                        | Oil                        | Chemical reaction             | Biodiesel      | Refinery products      |
|                        |                            |                               |                | Engines                |

This parts focus on the lignocellulosic biomasses, especially the woody biomass. Normally, the biomass fuel mainly come from the industry wood residues and forest residues. The types of biomass fuel for conversion process are chips, hog fuel, sawdust, cutter shavings, grinding powder, bark and agricultural product. Among these fuels, the sawdust, cutter shavings and grinding powder obtained from industry wood residues need to go through the mechanical handling process (chipping, crushing, pelleting and briquetting) before conversion. The original forest residues, including the completely small tree, the stem wood and the stumps, can be utilized for conversion directly after mechanical treatment. Table 2-2 lists the features of main woody biomass particle and their resources.

Table 2-2: Different shapes of woody biomass.

|                | Source  | Features  |
|----------------|---|---|
| <b>Chips</b>   | Forest and agricultural residues; Industry wood residues (chemical untreated) | Treatment process: Raw material use or mechanical handling (Sizing) |
| <b>Sawdust</b> | Industry wood residues (chemical untreated)                                   | Treatment process: Mechanical handling (Sizing)                     |

|                        |  |  |
|------------------------|--|--|
| <b>Cutter shavings</b> | Industry wood residues (chemical untreated)              | Treatment process: Mechanical handling (Sizing)  |
| <b>Grinding powder</b> | Industry wood residues (chemical untreated)              | Treatment process: Mechanical handling (Sizing)  |
| <b>Pellets</b>         | After mechanical treatment (from Industry wood residues) | Small size with high density particle, low transport cost; Treatment process: Mechanical handling (Pelleting)  |
| <b>Briquettes</b>      | After mechanical treatment                               | Bigger than pellets, high density and low transport cost; Treatment process: Mechanical handling (Briquetting) |

### 2.1.2 Composition

The lignocellulosic biomass consist of the three main terms of cellulose, hemicellulose and lignin, as well as small amounts of inorganic minerals and organic extracts [38]. Moisture content can also be found in the biomass materials, including the bound water (cell wall), the free water and the water vapour. The content of cellulose, hemicellulose and lignin depends on the biomass sources. Table 2-3 lists the typical ratio of lignocellulose content of different biomass sources.

*Table 2-3: Typical lignocellulose content of some lignocellulosic biomass feedstock.*

| <b>Feedstock</b>  | <b>Hemicellulose (%)</b> | <b>Cellulose (%)</b> | <b>Lignin (%)</b> |
|-------------------|--------------------------|----------------------|-------------------|
| Rice straw [38]   | 27.2                     | 34.0                 | 14.2              |
| Wood [39]         | 25.0-35.0                | 40.0-55.0            | 18.0-35.0         |
| Switch grass [40] | 25.0-30.0                | 35.0-40.0            | 15.0-20.0         |
| Barley straw [40] | 24.0-33.0                | 36.0-43.0            | 6.3-9.8           |
| Wheat straw [41]  | 26.0-32.0                | 29.0-35.0            | 16.0-21.0         |
| Corn stove [42]   | 26.0                     | 38.0                 | 19.0              |

The cellulose, which is a linear polymer, is the main part of the cell walls of lignocellulosic biomass [43]. The cellulose chains are packed together by microfibril (hydrogen bonds) which determines the crystalline or amorphous structure of the cellulose [14, 44]. As the second major part of the woody biomass, the hemicellulose is a heterogeneous polymer composed of several different types of monosaccharides (including glucose, mannose, xylose, galactose, etc) [38, 45]. Hemicellulose is an inhomogeneous structure and is covered around the celluloses [44]. For different biomass feedstock, the compositions of hemicellulose are different [46]. The lignin, which consists of cross-linked phenolic monomeric polymers, is a large, complex molecular

structure [43]. Figure 2-1 gives the main components of lignocellulosic material.

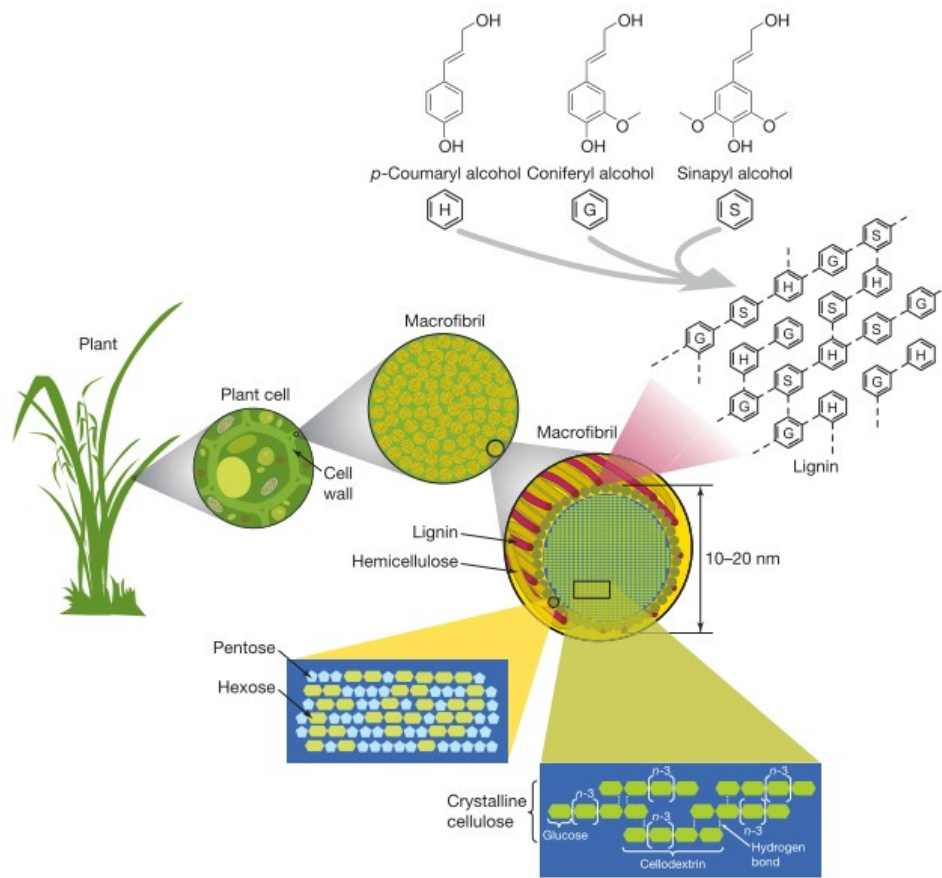


Figure 2-1: Lignocellulose structure [45].



## 2.1.3 Engineering properties

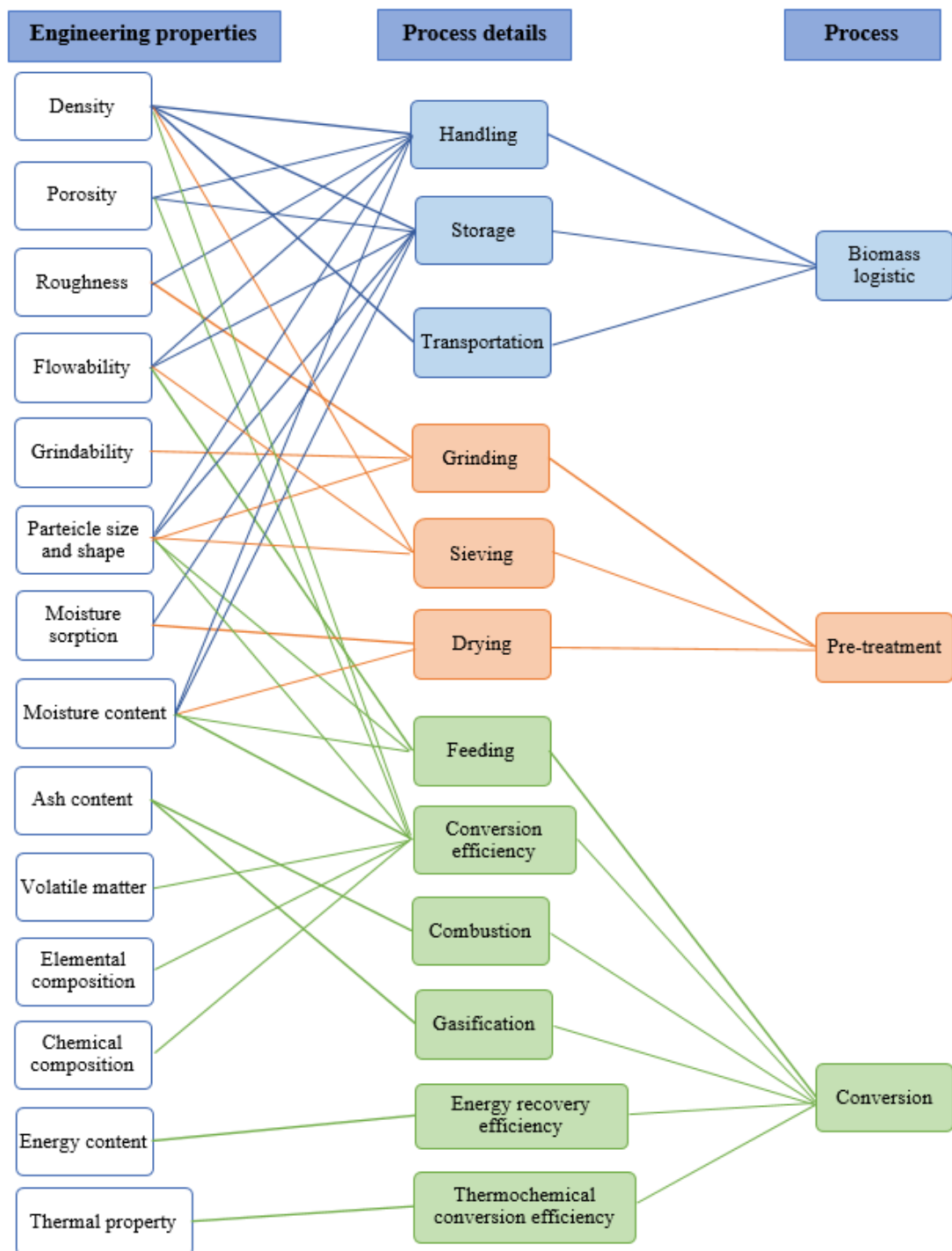


Figure 2-2: Engineering properties [36, 47].

The multiscale nature of the biomass feedstocks is a big challenge in numerical study of the biomass conversion [48]. The engineering characteristics of the biomass influence the quality of the biomass feedstock, the pre-treatment method and the efficiency of the conversion. These properties are particle density, followability, grind-ability, particle size, moisture content, moisture sorption, ash content, volatile matter, porosity, roughness, elemental and chemical

composition, energy content, thermal composition [36]. Cai et al. [36] concluded the engineering application of these properties in their review. They divided the whole process of converting biomass to biofuel into three parts: the logistics, pre-treatment and conversion processes. Tumuluru et al. [47] regarded the whole process as a function of material properties of the biomass. The engineering properties and their related logistic process are shown in Figure 2-2.

The particle density influences the biomass logistics part. The particle density changes during the whole biomass-to-fuel process. The biomass particle density is divided into two groups: bulk density and particle density [49]. Bulk density is the mass of per unit volume of powders or particles [50]. Bulk density influences the cost of feedstock transportation and storage. After pre-treatment, the density of biomass is increased to obtain high conversion efficiency. The particle size and shape are the parameters influence the conversion efficiency, the pre-treatment method and the handling and storage of biomass in different forms [51]. Nonuniform particle size and shape of the biomass will lead to high delivery and storage cost. Large particles always consume the long reaction time. The property of flowability influences the handling, feeding and storage process [52]. Moisture content relates to the drying, handling, storage, and feeding facilities and conversion processes. Woody biomass must be dried to become the biomass feedstock and used for energy production [49]. Two forms of moisture exist in the biomass particles: free moisture and bound moisture [53]. The free water is the liquid water or water vapor exist in biomass cells and the bound water is the chemical water within cell walls [54]. After pre-treatment process, the biomass loses most of the free water content which exists in the biomass cells and pores. The rest bound water content will be evaporated during the thermochemical conversion process. Ash content is an estimation of the potential risk of slagging and fouling during conversion, especially in combustion and gasification process [49]. The properties of volatile matter, elemental composition and chemical composition relate to the conversion efficiency. The elementary and chemistry composition of the biomass will influence the conversion efficiency. Stanislav et al. reviewed the chemical composition of different biomass resources [55]. Different plant species grown in different regions showed various elemental composition. Thus, the appropriate pre-treatment process will change the elemental composition of biomass, which will further affect the thermochemical conversion efficiency.

Table 2-4: Changed properties of biomass in different process [56, 57].

|                                    | Transportation | Storage | Pre-treatment | Conversion |
|------------------------------------|----------------|---------|---------------|------------|
| Density                            | √              | √       | √             | √          |
| Size & Shape                       | √              | √       | √             | √          |
| Porosity                           |                |         | √             | √          |
| Moisture content                   | √              | √       | √             | √          |
| Ash content                        |                | √       | √             | √          |
| Energy content                     |                | √       | √             | √          |
| Volatile content                   |                |         | √             | √          |
| Elemental and chemical composition |                |         | √             | √          |

Table 2-4 lists the changed properties in different process. For long distance transport, the biomass original feedstock needs to be processed (grinding, pelleting or drying) to concentrate storage. The biomass density, size and shape will be changed during these steps. The original biomass materials can be delivered directly for short distance transport. After long-term storage, the water content in the woody biomass volatilized and the density of these particles decrease. Three kinds of degradation will occur on biomass feedstock during storage: chemical, mechanical and biological. The original size and shape shrink and the porosity of the biomass increase. The pre-treatment process changes the physical properties of the biomass, including the density, size and shape, porosity and the moisture content.

#### 2.1.4 Chinese herb residues

China is one of the world's largest producers and consumers of Chinese herb materials, and annual Chinese medicine material is discharged around 5.0 million tons [58]. The Chinese herb residues are extract from the original herb materials (Figure 2-3). However, the herb residue is easy to decay and bring serious irreversible pollution to the surrounding environment. How to reuse and recycle this special solid waste is a very urgent significant job, yet a devil of a tricky problem. The Chinese herb residues (CHR) are a kind of biomass wates, which could be used as an alternative energy source for biomass thermal conversion technology [59, 60]. Compared with the traditional biomass wastes, such as wood residue and straw, the decocted Chinese herb residues have different chemical components [61].

The Chinese herb residues (CHR) are selected to investigate the kinetic characteristics. There are more than 15 million tons of Chinese herb residues after extraction of herb active components annually. However, the herb residues are easy to decay and potentially harmful to environment. How to reuse and recycle this special solid waste is an urgent job. CHR are also a kind of biomass waste, which could be employed as a renewable energy source via biomass thermal conversion technology. It is one of the most promising technologies in the large-scale clean utilization of herb residues due to its short process and high efficiency [59, 60].

Compared with other biomass such as stalks, straws, and wood residues, chemical compositions of the decocted CHR were significantly different, which suggested special pyrolytic behaviors [61]. This investigative topic remains a puzzled issue. Recently, several reports had proved that the catalytic pyrolysis of CHR was a solution with great application prospects, such as, the preparation of hydrogen-rich gas and the effective removal of CO<sub>2</sub> using Ni/CaO catalysts [62, 63], upgrading the quality of bio-oil by ZSM-5 catalysts [64, 65], and in-situ CO<sub>2</sub> capture promoted by CaO catalysts [66, 67]. However, the catalytic properties of potassium salts were rarely reported for the CHR materials, which has attracted much attention in recent years due to the exceptional catalytic effect of potassium on the on the pyrolysis and gasification for the traditional biomass [68, 69].

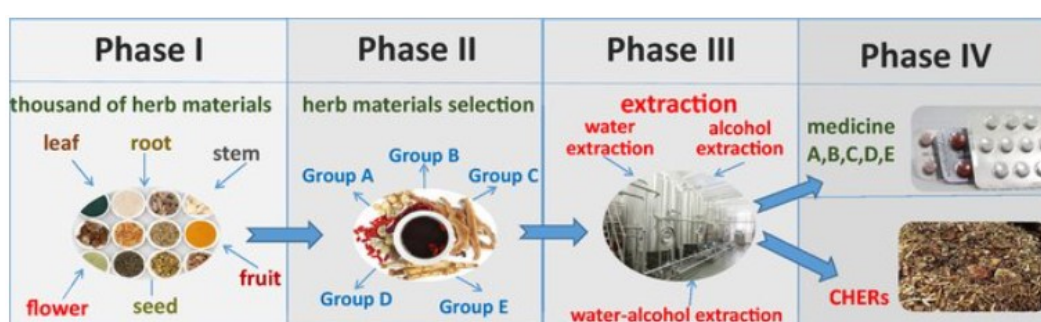


Figure 2-3: The production flow diagram of Chinese herb medicine and CHR [70].

The growth process of biomass (especially Chinese herb materials) will enrich a variety of inorganic salt minerals. These inorganic salts have a significant impact on the pyrolysis characteristics of biomass. Among such inorganic salts, potassium salt has attracted much attention in recent years due to its exceptional catalytic effect. Jia et al. [71] studied the catalytic effect and mechanism of K<sub>2</sub>CO<sub>3</sub>, KOH, CH<sub>3</sub>COOK, and KCl on the pyrolysis of wood chips, and confirmed that the catalytic activity trend follows the sequence of K<sub>2</sub>CO<sub>3</sub> ≈ KOH > CH<sub>3</sub>COOK > KCl. However, the addition of catalysts such as KNO<sub>3</sub>, K<sub>2</sub>SO<sub>4</sub>, K<sub>2</sub>HPO<sub>4</sub>, and KCl leads to secondary pollution problems by N, S, P and Cl in the pyrolysis process. Therefore, K<sub>2</sub>CO<sub>3</sub> becomes the hotspot of recent research because of non-heteroatoms and mildly corrosive [72-75]. Zhou et al. [69] examined the catalytic pyrolysis characteristics of sawdust and validated that K<sub>2</sub>CO<sub>3</sub> can provide an alternative reaction pathway of sawdust, reduce the activation energy of the pyrolysis reaction, and increase the yield of synthesis gas. The optimal yield of synthesis gas is achieved at 900°C and 10% of K<sub>2</sub>CO<sub>3</sub> addition. Fan et al. [76] investigated the K<sub>2</sub>CO<sub>3</sub> catalytic pyrolysis of three different agricultural and forestry wastes (pine wood, peanut hulls, rice straw), and concluded that the catalytic effect of K<sub>2</sub>CO<sub>3</sub> on the pyrolysis process of different raw materials highly relied on the physicochemical properties of biomass fuel, following the order of catalytic effect: pine wood > peanut hull > straw.

## 2.2 Biomass particle morphology

### 2.2.1 Particle shape

Biomass is naturally anisotropic, which means that it has different properties along different directions [77]. In many numerical studies, the biomass particles are seen as a function of a single characteristic length of the particle (such as sphere). However, the morphologies of real biomass particles are more complex, which show irregular shapes. Gil et al. [78] characterized the standard sieving method and measured the necessary parameters of the biomass. Four shape factors were used to classify the biomass: aspect ratio (AR), rectangularity, solidity and curl. Figure 2-4 shows several shapes of poplar and corn stover obtained from image analysis method.

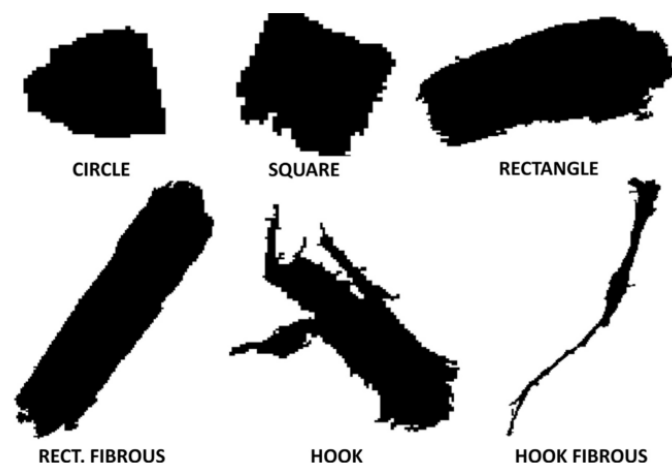


Figure 2-4: Different shapes of original lignocellulosic biomass from image analysis [78].

Different kinds of biomass feedstock show various size and shape characteristics [77, 79]. Figure 2-5 shows the milled biomass particles of different kinds of feedstock under same conditions. Most biomass particles display a roughly cylindrical shape, which present varying aspect ratios [77]. The large difference in the surface area to volume ratios of different shapes will affect the particle heating-up rates.

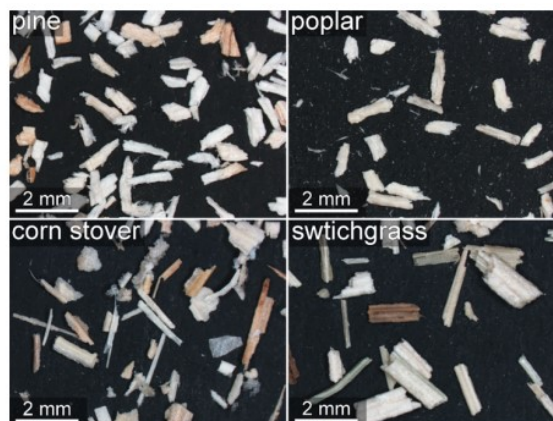


Figure 2-5: Micrographs of grinding biomass particles from different biomass feedstock [77].

Normally, researchers commonly study the cylindrical and spherical shape of biomass particles (discussion in Section 3.3). Ciesielski et al. [80] compared three different particle model geometries in the simulation, as shown in Figure 2-6. The first one (a) was a microstructure model which included the fibres and pores of the biomass. The second one (b) was a same profile model without the fibres and pores. The third one (c) was a sphere model. They found that similar behaviour was shown between the microstructure and solid models; however, the spherical model heats significantly slower than the others due to its much smaller surface-area-to-volume ratio.

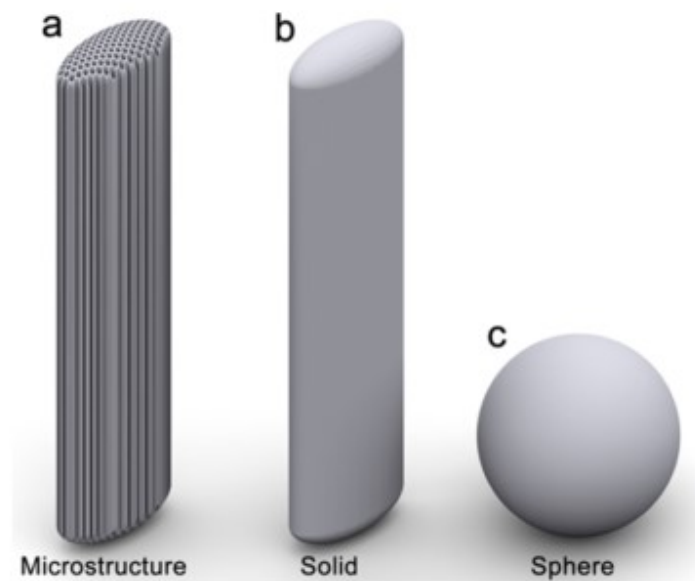


Figure 2-6: Particle model geometries used in numerical simulations of heat and mass transfer [80].

### 2.2.2 Biomass particle size distribution

The size distribution of biomass particles is given by standard sieving method. The high heating rates of the material will maximize the liquid oil yield of the biomass thermochemical conversion. Typically, the particle size should be reduced to less than 3mm before entering the reactor to ensure the sufficient heating rates [9]. It is a big challenge to develop simulation models that are sufficiently accurate and computationally efficient because it is necessary to treat highly complicated multi-scale, multi-phase and multi-physics problems [81]. The precise structure and properties of biomass particles should be highly emphasised in the following research [48].

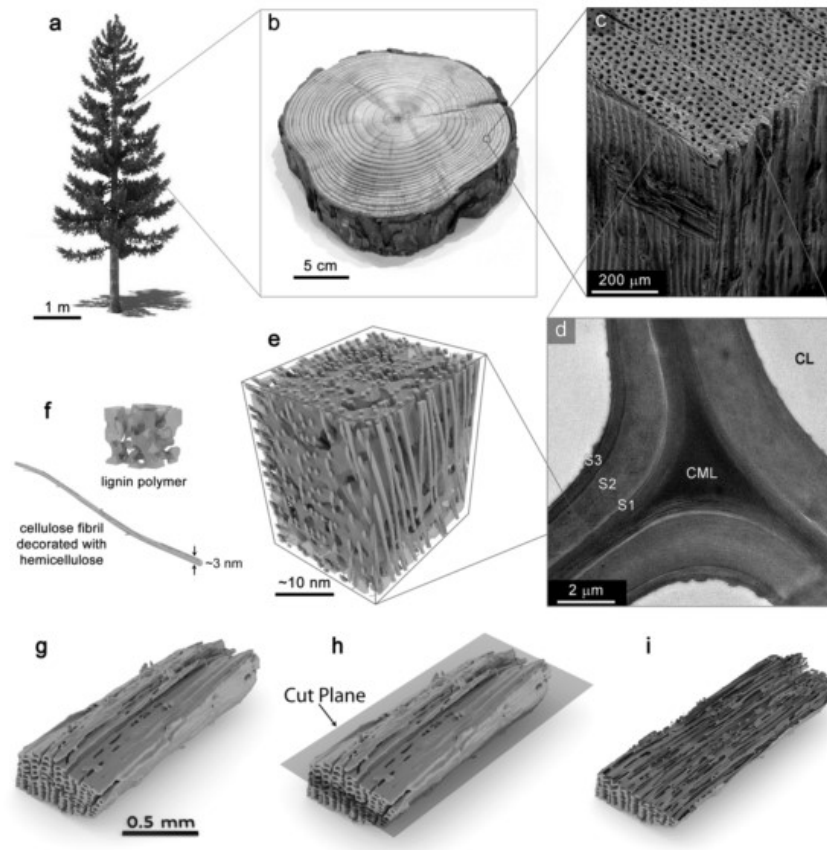


Figure 2-7: Microscale visualization of woody biomass [82]. (a) Coniferous tree; (b) Section of a pine trunk; (c) Microcellular structure of wood tissue; (d) Micrograph of cell wall with various layers; (e) The nanoscale arrangement of biopolymers within the cell wall; (f) Micrograph of amorphous lignin polymer and a cellulose fibril; (g-i) X-ray computed topography reconstruction of a milled pine particle 0.5mm.

Figure 2-7 shows the multi-scale structure of the lignocellulosic biomass, from the whole tree to the microstructure the arrangement of cellulose, hemicellulose and lignin of cell wall. Figure 2-7 (g-i) give the X-ray computed pine biomass particles milled to 0.5mm. It shows high aspect ratio and non-spherical porous structure. Table 2-5 lists the microstructures of the biomass particles with different size groups. Usually, the size of biomass particles that fed into the reactor concentrate on  $10^{-3}$  to  $10^{-1}$ m size groups. These particles are obtained from original woods or crops ( $10^0$  to  $10^{-1}$ m) [48].



Table 2-5: Multiscale biomass composition [36].

| Physical structure         | Size scale (m) | Composition   |
|----------------------------|----------------|---|
| Cellulose                  | $10^{-10}$     | C-C, C-H, C-O, O-H bonds, oxygenated and aromatic rings   |
|                            | $10^{-9}$      | Cellulose (linear polymer with $\beta$ -linked glucose);<br>Hemicellulose (5-C sugar monomers amorphous polymer); |
| Lignocellulose             | $10^{-8}$      | Lignin (3D polymer with oxygenated phenylpropane);<br>Small organic and inorganic ions                            |
|                            | $10^{-7}$      | Lignocellulose nanolayers   |
| Wood Cell                  | $10^{-6}$      | Cells (A matrix of lignocellulose nanolayers)   |
| Microstructure             | $10^{-5}$      | Groups of adjacent cells (tissues)  |
|                            | $10^{-4}$      |   |
|                            | $10^{-3}$      | Small fibers and stem sections  |
| $10^{-2}$                  |                |   |
| Wood stem                  | $10^{-1}$      | Whole plants  |
|                            | $10^0$         |   |
| Macroscopic biomass (Tree) | $10^1$         |   |

The forms of particle size distribution for thermochemical conversion processes had been reported in many literatures. The form of particle size distribution largely depends on the sieving techniques: mechanical sieving, dynamic imaging, laser diffraction and so on (details in Section 5.1). Trubetskaya et al. [79] measured the size distribution of three biomass feedstock, using different sieving techniques (Figure 2-8). It is clear that different techniques and biomass feedstock showed different cumulative size distribution. Wiggins et al. [83] proved that the heating up rates are different for different size distribution. They compared the heat-up time of single particle (0.5mm and 2mm) and the weighted distributed particles (Figure 2-9).

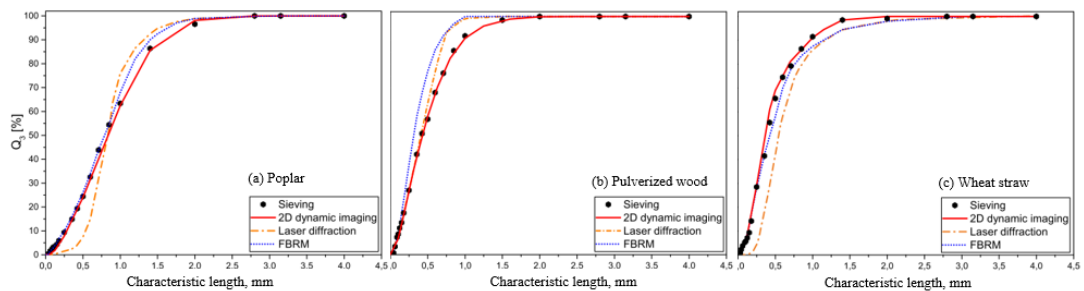


Figure 2-8: Cumulative particle size distribution  $Q_3$  (%), for different kinds of biomass feedstock (poplar, pulverized wood and wheat straw) and sieving methods: Sieving, 2D dynamic imaging, laser diffraction and FBRM (focused beam reflectance technique) [79].



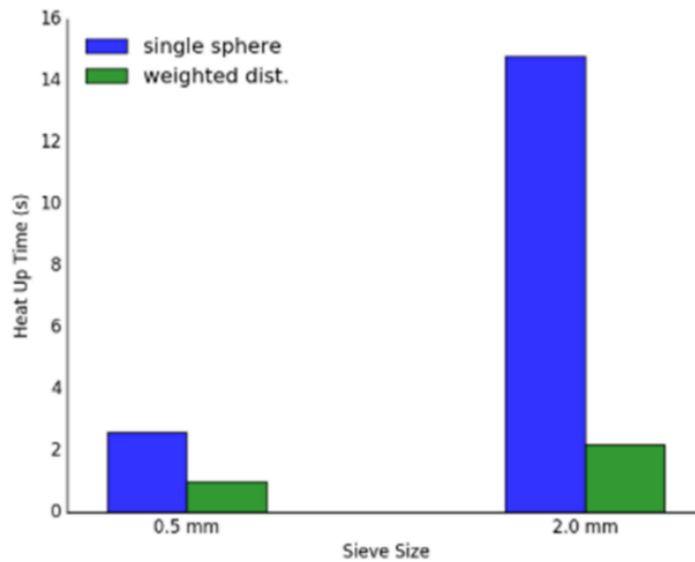


Figure 2-9: Heat-up time of single particle vs weighted distributed particles [83].

### 2.2.3 Particle size and shape effect

The particle shape and size distribution greatly affect the dynamics of biomass particles, including the drying, heat transfer rate and reaction efficiency [84]. Since the fast pyrolysis for producing liquid fuels only occurs in a few seconds, the heating-up rate of particles must be sufficient to finish the heat transfer. The size and shape of biomass particles should be finely designed in thermochemical conversion processes. The dimensionless parameter: Biot number ( $Bi$ ), is considered as an important particle characteristics to describe the ratio of internal thermal resistance of a particle to the external thermal resistance of a particle [85]. The critical Biot number where the internal temperature gradient of particle become significant was set as  $Bi=1$  [86]. When  $Bi<1$ , the temperature gradient within particles can be regarded as isothermal, while for  $Bi>1$ , the particles are considered as “thermally thick” and the devolatilization behaviour of these particles have large difference with the isothermal one [29].

Janse et al. [28] researched three types of single wood particles: Disc/flake-like, Cylindrical, Spherical shape with similar mass and volume. They found that the increase of particle size leads to obvious increase in thermal decomposition time and the heat transfer rate of spherical particles was quicker than the other shapes. Lu et al. [84] proved that the particle shapes will not only affect the conversion efficiency, but the product yield distribution. They studied three kinds of particle shapes: spherical, cylindrical and disc-like (Figure 2-10) and found that near-spherical particles display higher bio-oil yield and react more quickly compared with non-spherical particles. Bennadji et al. also verified that the increasing particle size would raise the devolatilization time [16].

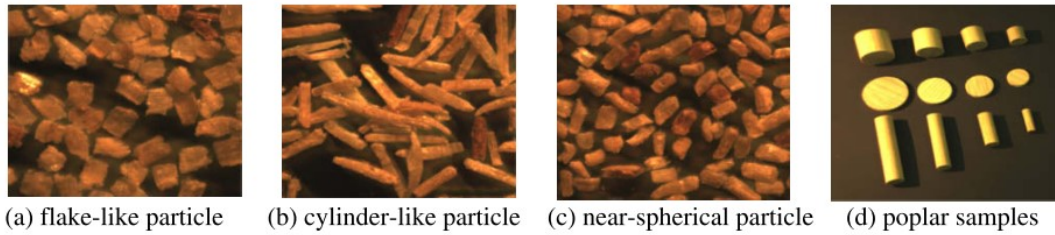


Figure 2-10: Imaging shape of biomass particles [84].

## 2.3 Biomass thermochemical conversion

### 2.3.1 Overview

During the thermochemical conversion process of biomass, different sub-processes can occur such as the drying, ignition, devolatilization, etc. With varying modelling properties (biomass particle properties, modelling conditions), the sub-processes will occur simultaneously or sequentially [53]. Figure 2-11 shows the particle size and structure change during conversion processes. The following details are given to the whole thermochemical conversion process:

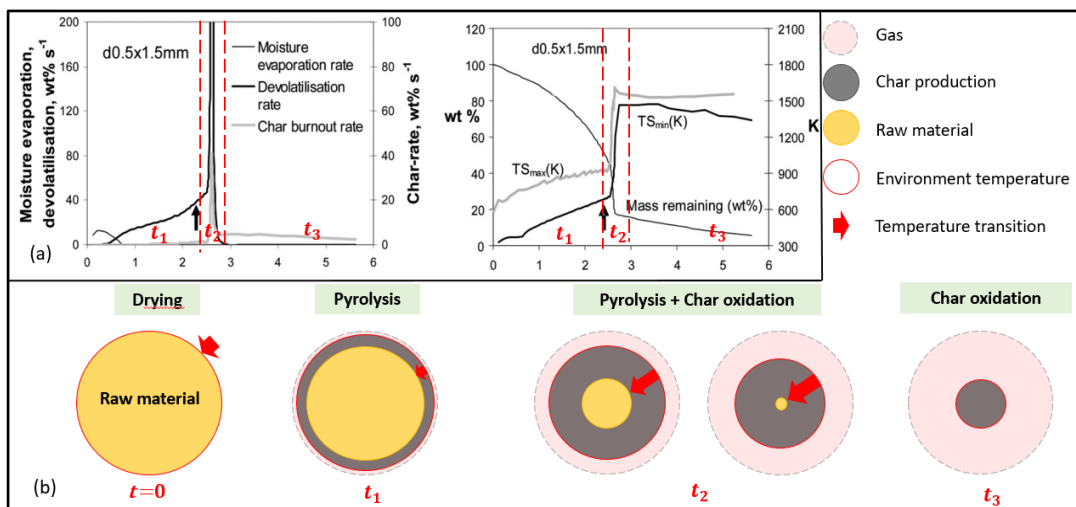


Figure 2-11: (a) Process rates of moisture content, devolatilization and char burn out. Mass loss history, max and min temperature inside particle [66]. (b) Single particle conversion steps.

#### First stage: Drying ( $t=0$ )

The drying process occurs at the beginning of the thermochemical conversion, volatilizing the residual moisture in biomass.

#### Second stage: Pyrolysis ( $t_1$ )

In this stage, the drying and devolatilization occur simultaneously. As the heating temperature

increasing, the char layer forms gradually and the water content in biomass volatiles completely.  $TS_{max}$  and  $TS_{min}$  increase gradually. The products of this stage are primary tar, char, water vapor and syngas.

**Third stage: Pyrolysis and char combustion ( $t_2$ )**

The devolatilization and char combustion process both occur rapidly in this stage. The char product increases continually as the increasing temperature, at the same time, the formed char layer on the biomass surface combusts.  $TS_{max}$  and  $TS_{min}$  increase rapidly, then suffer a sharp decrease. It is noticed that the char generation rate is greater than the char burnout rate.

**Last stage: Char combustion ( $t_3$ )**

In this stage, all the raw materials react completely. The char generated at previous stage reacts gradually. Core temperature equals the environment temperature approximately.

A simplified schematic description of temperature distribution inside the biomass particle during devolatilization process was assumed by Biwas and Umeki (Figure 2-12) [81]. As the reaction proceeding, char layer formed on the biomass surface and the heat transferred through the layer to the core area from the surrounding environment.

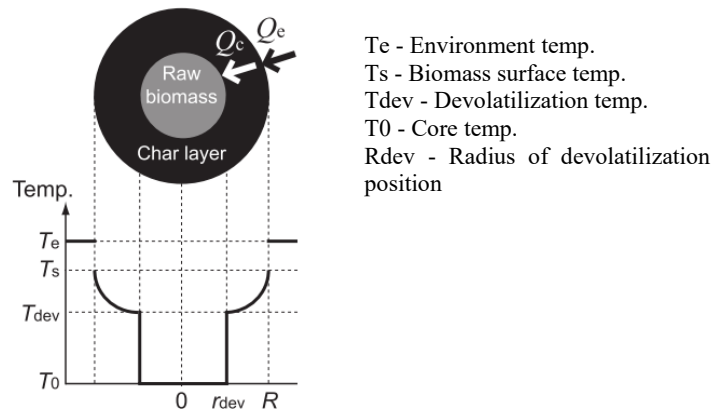


Figure 2-12: Schematic description of the biomass temperature distribution [81].

The modelling and simulation methods of the biomass thermochemical conversion have been developed by many researchers. The focus on the biomass modelling area multiscale, including small particle scale model, the chemical kinetic model, the reactor scale model, and the process scale model. Different modelling scales aim at researching different properties of biomass thermochemical conversion. Gagliano et al. studied the biomass gasification and pyrolysis process to predict the product composition using three novel numerical thermodynamic equilibrium models [87]. Bisulandu and Marias developed a numerical model to simulate the thermochemical conversion process of biomass in cement rotary kiln [88]. A CFD model of travelling bed gasifier was developed by Bernada et al. to simulate the gasification process of

solid waste [89]. Since the complexity of these process, it is necessary to consider many related parameters and conditions, such as the physical properties, the reaction types, the transport properties and so on. The mathematical models of biomass particles conversion in bed reactors usually controlled by governing equations: mass, energy, and momentum transport equations [90-93].

### 2.3.2 Pyrolysis

Pyrolysis is considered the most powerful technique in biomass-to-bioenergy process, since it has ability to produce the highest liquid fuel compared with other thermochemical processes. The fast pyrolysis is typically operated under the condition of 500°C to 800°C and heated rapidly to obtain liquid product [8, 94]. The moderate operation temperature and short residence time make sure the high heating up rate of biomass particles. Table 2-6 concludes the product yields of different pyrolysis modes. Different types of pyrolysis occur at different operating conditions, including the operation temperature, the feedstock size and the residence time. It is obvious that the fast pyrolysis produces the highest liquid fuel with very high heating-up rate. Compared with the other forms of product, the liquid product have the advantages of easy of transport, storage and high energy density [9].

Table 2-6: Pyrolysis modes and product yield [9, 38, 94-97].

| Pyrolysis technology | Conditions   | Heating rate | Liquid                   | Solid           | Gas     |
|----------------------|--|--------------|--------------------------|-----------------|---------|
| Fast                 | ~500°C;<br>Vapour residence time: <2s;<br>Solid residence time: 10s;<br>Feedstock size: <1 mm; | Very high    | 75 wt.% of bio-oil       | 12 wt.% of char | 13 wt.% |
| Immediate            | ~400°C;<br>Vapour residence time: 5s-20s;<br>Solid residence time: ~20min;                     | High         | 40-50 wt.% in two phases | 40 wt.% of char | 20 wt.% |
| Slow (carbonization) | ~400°C;<br>Residence time: hours-days;<br>Feedstock size: 5-50 mm;                             | Very low     | 30 wt.% in two phases    | 35 wt.% of char | 35 wt.% |
| Conventional         | ~600°C;<br>Residence time: 5-30min;  | Low          | 36% wt.% of bio-oil      | 30 wt.% of char | 34 wt.% |
| Flash                | 300°C~700°C;<br>Residence time: <0.5-1s;<br>Feedstock size: <0.2 mm;                           | High         | 75 wt.% of oil           | 12wt.% of char  | 13 wt.% |
| Hydro-pyrolysis      | <500°C;<br>Residence time: <10s;   | High         |                          | —               | —       |

|              |                                     |      |   |                 |             |
|--------------|-------------------------------------|------|---|-----------------|-------------|
| Gasification | ~750°C-900°C;<br>Residence time: 5s | High | — | ~2 wt.%<br>char | ~98wt.<br>% |
|--------------|-------------------------------------|------|---|-----------------|-------------|

To ensure the highest bio-oil yield, the fast pyrolysis process requires the following characteristics [95]: (1) moisture content within the biomass feedstock need to be reduced less than 10%; (2) biomass particles need to be grounded less than 3mm; (3) the whole process occurs at moderate temperature (~500°C); (4) rapid char removal technique and vapour cooling rate. The thermochemical decomposition scheme of biomass particles is very complex. The possible reaction pathways of biomass pyrolysis are shown in Figure 2-13. In primary biomass decomposition reaction, the raw biomass material decomposed rapidly when the temperature reach to pyrolysis condition. The primary products are syngas (CO, CO<sub>2</sub>, H<sub>2</sub> and CH<sub>4</sub>) and char. As the increasing of the operation time, secondary gas phase cracking occurs inside biomass.

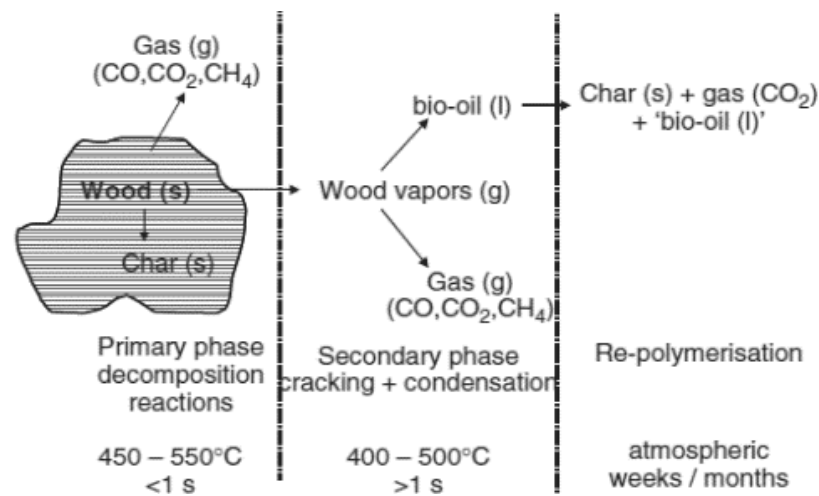


Figure 2-13: Pyrolysis reaction path of woody biomass [98].

When simulating the pyrolysis process, the kinetic scheme needs to be considered to simulate the thermal decomposition of biomass. The kinetic mechanisms are affected by various properties, including the reaction condition, the biomass composition and operation parameters [99]. Thus, the precise results of simulating the thermochemical conversion of biomass are largely depended on the construction of kinetic model. Different pyrolysis kinetic models had been studied by various research. Biomass is a highly heterogeneous substance, and the pyrolysis process of biomass involves complex chemical and physical changes. Thus, the kinetic mechanism of pyrolysis process is complex and cannot be successfully defined using kinetic models [100, 101]. The detailed kinetic models of current study will be introduced in Section 2.5.2.

## 2.4 Nitrogen functionalities

According to Section 2.3, there are three main ways of biomass thermochemical conversion and utilization: pyrolysis, gasification, and combustion. The research on the formation mechanism and characteristics of Nitrogen (N) pollutants focused on the fuel-N pollutants [102]. All of the three types of thermochemical conversion undergo primary pyrolysis of fuel-N conversion and secondary reaction of N-containing pollutant formation. Due to the different operation methods, the reaction pathways can be concluded by [103]:

- Devolatilization (primary pyrolysis): The fuel-N is converted into volatile-N and semi-coke N, where volatile-N includes gas phase N and tar-N.
- Secondary reaction: The free radicals (H, OH, O) introduced by the reaction medium or released by the fuel structure play a key role in this stage. For pyrolysis process, the oxygen does not participate the reaction, and the fuel-N is mainly converted into NH<sub>3</sub>, HCN, HNCO, semi coke N and tar-N. The product NH<sub>3</sub>, HCN, HNCO are called NO<sub>x</sub> (NO and N<sub>2</sub>O) precursors.

Some research results show that biomass char significantly affects soil nitrogen form and content, mainly in two aspects [104-108]: one is to reduce the loss of mineral nitrogen; the other is to promote organic nitrogen mineralization, especially to accelerate nitrification. Physical char can improve soil porosity, improve soil permeability, change soil microbial community structure, increase microbial activity, and promote nitrification, but reduce denitrification, thereby reducing soil N<sub>2</sub>O emissions [105]. If nitrogen can be immobilized in solid carbon products to obtain valuable nitrogen-containing carbon materials (widely used in catalysis, pollutant adsorption, and energy storage). However, there is no report on the conversion of nitrogen into nitrogen-containing carbon materials to control nitrogen emissions. Therefore, it is necessary to study the nitrogen fixation pathway and nitrogen transformation mechanism during pyrolysis to reduce nitrogen emissions.

### 2.4.1 Characteristics of nitrogen functionalities

Compared with coal fuel, biomass fuels are full of O and H elements, and the thermochemical conversion process can promote the entry of fuel N into volatile matter. The content of N in different biomass materials have a great impact on pyrolysis products. Table 2-7 lists the N content of different biomass fuel.

Table 2-7: N content of different biomass fuel [109-113].

| Fuel type        | N content    |
|------------------|--------------|
| Woody biomass    | 0.1-1.0 wt.% |
| Herbal biomass   | 0.3-4.0 wt.% |
| Aquatic plants   | 3.0-7.0 wt.% |
| Industrial waste | 2.5-9.0 wt.% |

Chen et al. [114] studied the evolution and transformation of N content during the microalgae pyrolysis process for different temperature condition. The results showed that the N content in char product decreased continually as the pyrolysis temperature increase from 400°C to 800°C (Figure 2-14). The distribution of N in bio-oil product increased at first, then decreased after 500°C. These results due to the cracking of amino acids, which will convert to the N-containing compounds. The different colour of lines represents different types of samples. From the figure, we can see that in the low temperature zone of pyrolysis, the most nitrogen were obtained in carbon product, then, in the high temperature range, main N products were found in gas product.

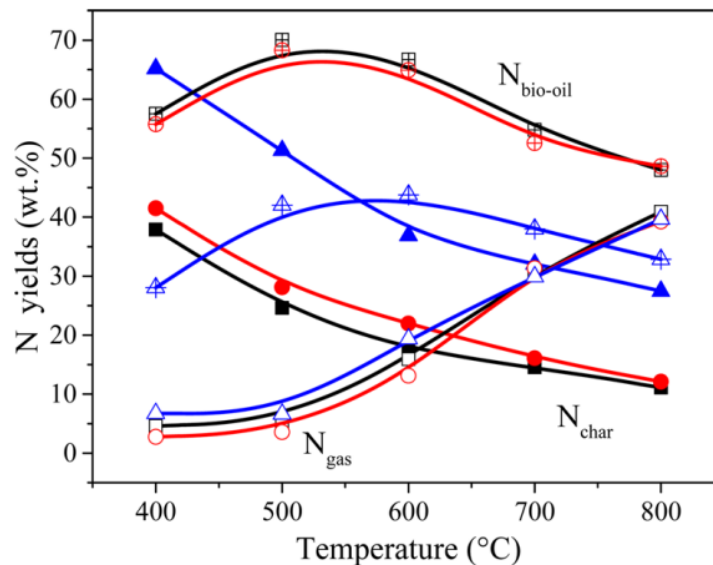


Figure 2-14: Distribution of N in pyrolysis product as a function of temperature [114].

The structure of N-containing groups of fuel affects the formation and evolution of NO<sub>x</sub> precursors in pyrolysis process. Leppalahti and Koljonen [115] concluded the characteristics of N functionalities of different fuels. They found that the existing form of N-containing structure of the biomass fuel is protein. Hansson et al. [113] had argued that the content of N in biomass is in form of proteins or free amino acids, and the protein-N accounted for 66-87% of total N content. They pointed out that the NO<sub>x</sub> precursors of the biomass pyrolysis are came from these

proteins.

There are several techniques can be used for investigating the Nitrogen functionalities in solid materials. The most successful method to study the functionalities of nitrogen in solid materials is X-ray photoelectron spectroscopy (XPS) [116]. The non-destructive XPS technique has been used on large scale investigation of N-containing species. Compared with the XPS, the Time of Flight Secondary Ion Mass Spectrometry (TOF-SIMS) method is destructive. The application of the other non-destructive techniques (such as Nuclear Magnetic Resonance (NMR) and Infra-red (IR) techniques) on studying the evolution of Nitrogen functionalities are not satisfactory until now [116]. A good alternative non-destructive technique is X-ray absorption near edge structure (XANES), which is a ray structure of absorption spectrum [117]. The results from XPS and XANES can be used for verifying each other.

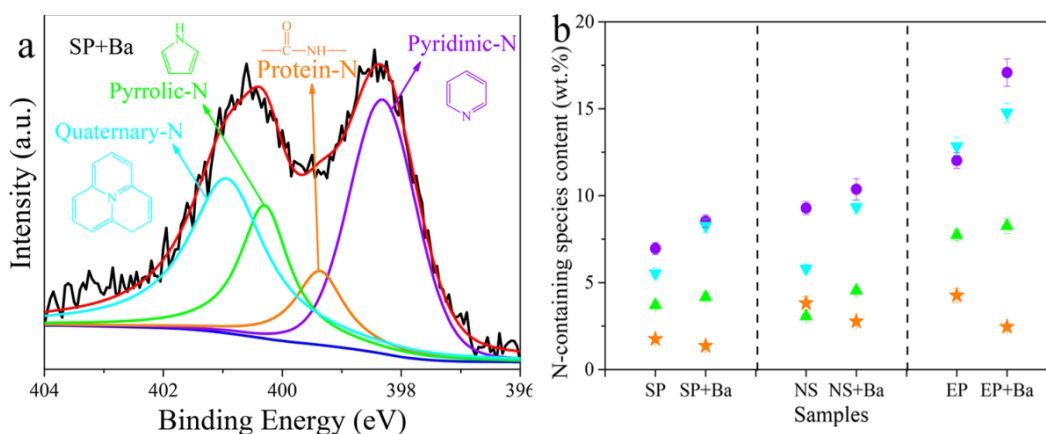


Figure 2-15: XPS N 1s spectra of N-containing groups in pyrolysis char product (a), with the N-containing species content of different materials (b) [118]. The materials used in Figure 2-15 are *Sapirulina platensis* (SP), *Nannochloropsis* (NS), *Enteromorpha prolifera* (EP) and bamboo waste (Ba).

Figure 2-15 is the XPS N 1s spectra of N-containing species in pyrolysis char product of biomass [118]. The N-containing species could be divided into five groups [119]: (1) Protein-N ( $399.7 \pm 0.4\text{eV}$ ), (2) Pyrrolic-N ( $400.2 \pm 0.3\text{eV}$ ), (3) Oxidized-N ( $402\text{-}405\text{eV}$ ), (4) Quaternary-N ( $401.2 \pm 0.3\text{eV}$ ), (5) Pyridinic-N ( $398.5 \pm 0.3\text{eV}$ ). It could be found that only small amount of protein-N exists in the char product and large amount of pyrrolic-N, pyridinic-N and quaternary-N exist in the product after pyrolysis. Different materials showed various properties of N-containing functionalities.



## 2.4.2 Evolution of nitrogen functionalities during pyrolysis

During pyrolysis process, the N-containing groups change as the increasing heating temperature. Many researchers studied the control of N emission of coal pyrolysis [120-122]. Kelemen et al. [123] investigated the evolution characteristics of N functionalities during pyrolysis of coal. They found that the main existing forms of N-containing groups in coal are pyridinic-N, pyrrolic-N, and quaternary-N. Figure 2-16 gives the N transformation mechanism at different pyrolysis temperature of coal samples. As the increasing heating temperature, the content of quaternary-N was continually rising. The thermal stability of quaternary-N is higher than pyrrolic-N and pyridinic-N.

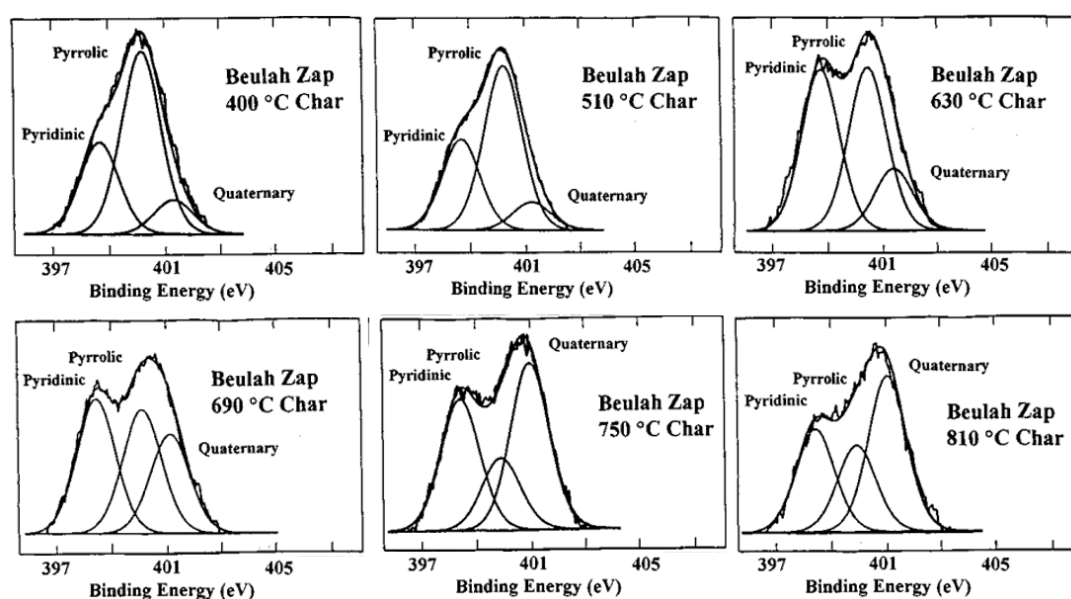


Figure 2-16: N 1s XPS nitrogen spectra of coal samples produced by pyrolysis at different temperature [123].

However, for the biomass fuel, the protein-N is the dominant form, which is different from the coal fuel [124]. Figure 2-17 gives the N 1s spectra of the product char of spirulina platensis pyrolysis at different temperatures. It could be found that there are four N-containing functional groups exist in spirulina platensis, including protein-N, pyridinic-N, pyrrolic-N, and quaternary-N. At 400°C, the main existing form of N in sample was protein-N, then, the content of protein-N decreased gradually with the increase of the pyrolysis temperature. This was because of the low thermal stability of the protein-N.

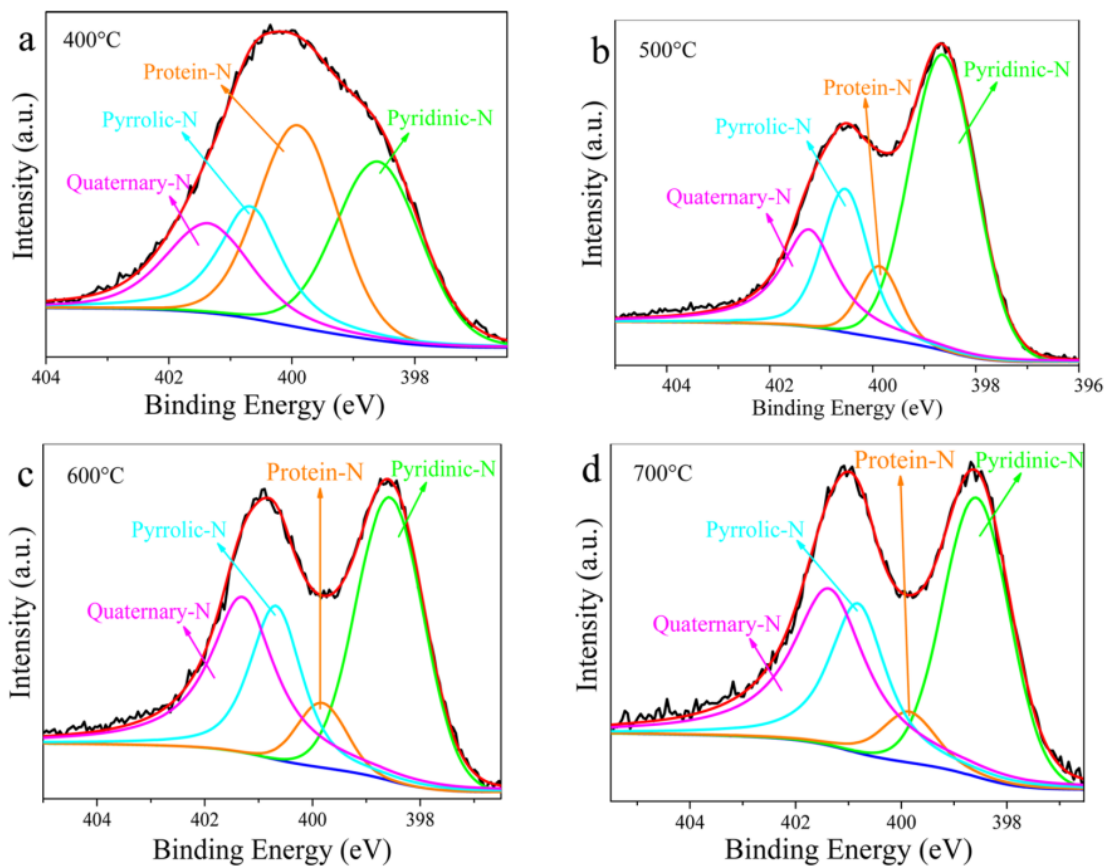


Figure 2-17: N 1s XPS spectra of spirulina platensis samples produced by pyrolysis at different temperature [114].

## 2.5 Modelling of the thermochemical process the biomass

### 2.5.1 Overview

For the biomass thermochemical conversion process, models contribute to the design of thermal conversion reactor, predict the operation properties in different conditions (normal condition, load or fuel change condition, start-up and shut down condition) [125]. The reason why the numerical modelling method is widely used now is that some necessary parameters cannot be measured experimentally. For instance, the reaction time of fast pyrolysis process is very short, thus, the requirement of measuring instruments with quick response times, and the intra-particle temperature distribution cannot be obtained accurate [99]. Two main modelling approaches are mechanistic modelling and empirical modelling [126]. The mechanistic modelling, also known as the mathematical modelling, is based on the mechanisms of a system, predicting and understanding the behaviours of a process or components. However, the empirical models, which based on the directly observed and measured data from experiment, are more simplistic and do not need too many computations. It uses curve fitting the process details to summarise the experimental results [127]. In chemical engineering, the mathematical method is generally applied to construct the biomass conversion models. The focus on the biomass modelling area is multi-scale, including the small particle scale model, the chemical kinetic model, the reactor scale model and the process scale model (Figure 2-18). The single particle model was developed to observe the phenomena occurring inside the particle during conversion. The process-scale simulation aimed at modelling the whole thermochemical process and optimizing the design of reactors. Over the past few decades, the researches of biomass pyrolysis mainly focused on the following subjects [48]: (1) Investigating the chemical compositions of biopolymers in biomass (cellulose, hemicellulose and lignin); (2) Improving the reaction-transport models to simulate the thermochemical conversions of lignocellulosic structures; (3) Designing and optimizing the reactors using modelling methods. Different modelling scales aim at researching different properties of biomass thermochemical conversion. This section reviews the modelling methods of biomass particles and the presented models.

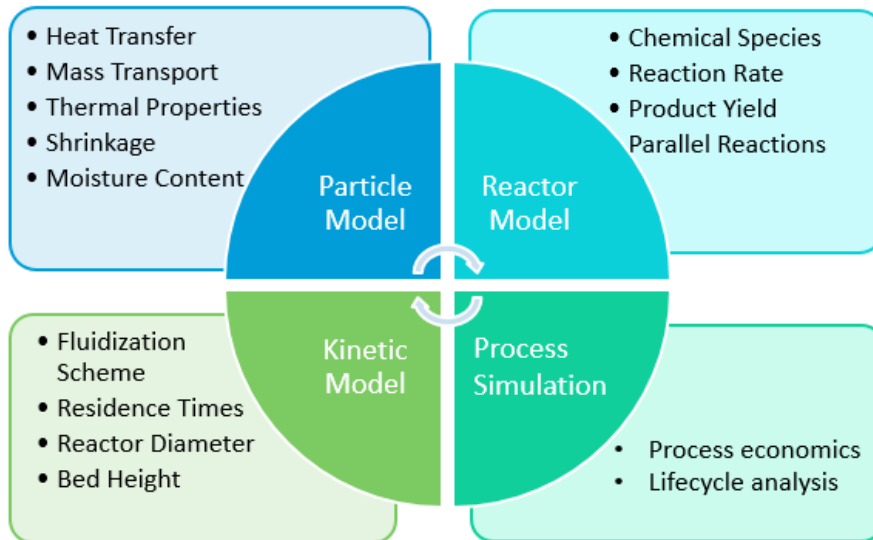


Figure 2-18: Modelling scales of biomass conversion.

Many reasons lead to the widespread application of fast pyrolysis modelling method, including the heating-up rate of particles and the real time temperature are difficult to measure experimentally; instantaneous reaction requires the measuring equipment with high precision; the contact between the sample and the thermocouple is difficult to keep close in experiment [99]. However, the multiscale nature of biomass feedstock and the multiphase nature of pyrolysis are challenges of the biomass thermochemical conversion simulation [48]. During the thermal conversion of biomass, a particle undergoes a variety of processes, such as drying, ignition, devolatilisation and volatiles combustion, char gasification and char oxidation. The single particle models of biomass could be used to investigate the intra-particle heat and mass transfer principle, predict the effect of the particle physical properties on the conversion efficiency and production yield and assess the thermochemical conversion systems [128, 129].

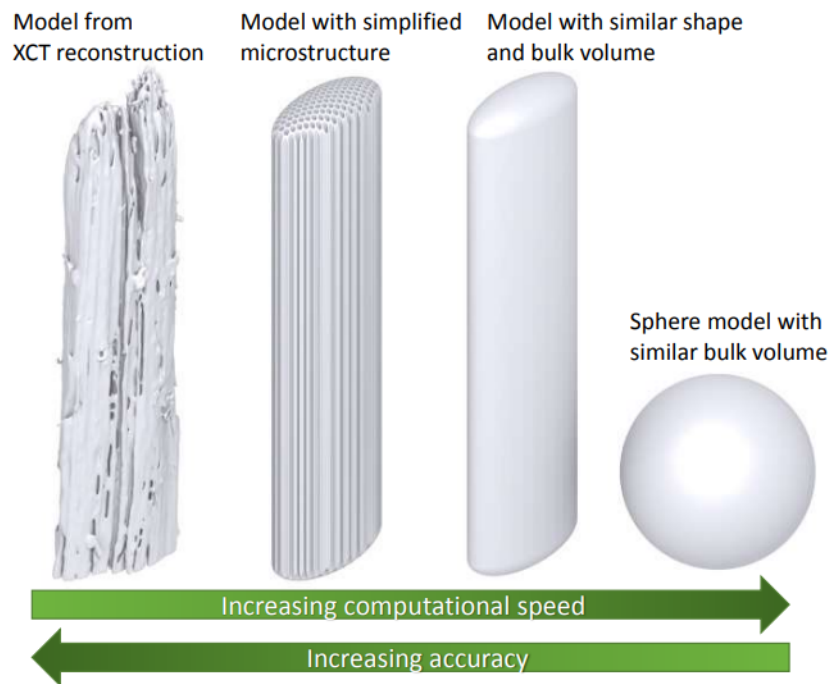


Figure 2-19: Comparison of different simulation models in terms of accuracy and computing time [130].

Most of current biomass particle models are simplified to uniform size and shape, ignoring the size distribution and asymmetric nature. This is because the simplified structure is easy to be constructed. Ciesielski et al. [130] concluded that the more precise model construction, the more accurate of the simulation results, and the lower computation speed in developing the single particle model (Figure 2-19).

For the biomass thermochemical conversion process, models contribute to the design of thermal conversion reactor, predict the operation properties in different conditions (normal condition, load or fuel change condition, start-up and shut down condition) [125]. Compared with the laboratory experiments, the modelling method not only can save cost and time but also can optimize the real experiment systems. To find out the most efficient way of biomass conversion, researchers use modelling method to simulate different conversion process of biomass particle [131]. Bidabadi et al. [132] investigated an analytical model of single biomass particle to study its pyrolysis behaviour. Biomass gasification process was modelled by Gomez-Barea et al. [125] using fluidized bed reactor. In 2017, Liu et al. [133] developed a shrinkage CFD model of biomass particles to simulate the fast pyrolysis process. Sadhukhan et al. [134] developed a kinetic model of large size wood particles to see the heat transfer performance during pyrolysis process. The review of Jiang et al. [131] listed a large amount of single particle combustion model. They presented the decomposition method of solid fuel particle (coal, biomass...) and different modelling strategies of different particles.

## 2.5.2 Reaction mechanisms

The fundamental studies of conversion processes occur at biomass particle level are studied by simulating single particle model. This part focuses on summarizing and comparing the biomass conversion characteristics in particle level from previous studies. Also, the mechanism of heat and mass transfer inside the particle are discussed. The thermochemical conversion consist of multi-step parallel processes, including dehydration, pyrolysis, gasification and carbon oxidation [135]. The complex reaction mechanism could be concluded by different kinetic models. The pyrolysis process is the initial reaction of gasification, liquefaction and carbonization. Models for the pyrolysis of biomass are generally based on the apparent kinetics. Table 2-8 listed the different types of pyrolysis kinetic models developed by researchers [32, 101, 136-138].

The one-step global model was one of the first developed model when simulating thermochemical conversion process of biomass [101]. The developed model considers the pyrolysis as a single step first order reaction, in which the biomass decomposes into gases and solid char with a fixed char yield. This kinetic model is oversimplified the complex reaction mechanism of pyrolysis. The effect of moisture and char oxidation was ignored in this model.

The competing kinetic model considers differing yields of char [139]. It was assumed that the primary and secondary reactions are grouped together, which means competitive reaction. The total three products are formed simultaneously. This model is generally used for woody biomass pyrolysis.

The secondary char cracking model is the two-stage parallel reaction model. The feedstock is initially thermos-decomposed into three products, gases, tar and char, with the undergoing further decomposition into gases and char [139]. The Broido-Shafizadeh model was widely used for cellulosic material. The original material components (original cellulose, hemicellulose, lignin) transformed to active components firstly, then, continue to primary and secondary decomposition.

Table 2-8: Pyrolysis kinetic models [32, 101, 136-138].

| Kinetic model                 | Pathway | Description  |
|-------------------------------|---------|--|
| One step global model         |         | One-step global models were first developed when simulating the thermochemical conversion of biomass. The single step first order reaction of pyrolysis was considered. The biomass decomposes into gases and solid char with a fixed carbon.  |
| Competing model               |         | This is the most popular kinetic model of woody pyrolysis. This model contained the lumped primary and secondary reactions. It was assumed that the activation energy for char formation is equal to that of the weight loss reaction, resulting in a varying char yield.  |
| Secondary char cracking model |         | A rate of competition model had been developed to account for secondary reactions in which tar was cracked into lighter gases or re-polymerized to form char. The primary reactions were the first order reaction, considering Arrhenius-type temperature dependence. The secondary reaction rate is proportional to the tar vapour concentration. |
| Broido-Shafizadeh scheme      |         | The Broido-Shafizadeh scheme was widely used for the pyrolysis of cellulosic material. The original cellulose was transformed to active cellulose first, then, continue to decomposition. The extend model was original cellulose, hemicellulose and lignin turn to active components.   |

Numerous reports had showed that the calculation results obtained from the Kinetic-free method give a better description of the pyrolysis process of biomass [140, 141], especially for the Starink method [69, 142]. On the other hand, the kinetic-free model only offers very limited kinetic information, except the activation energy and pre-exponential factor. For more comprehensive kinetic analysis, the determination of significant mechanism function is very important. Although various reaction schemes have been developed to describe the mechanism functions [143-147], they always appear to be inconvenient when using these complex reaction models, which involve a lot of unknown kinetic parameters that cannot be simply obtained by traditional model-free methods. In this paper, the reaction mechanism and pre-exponential

factor were analyzed by using the generalized master-plots method, and the model results using the optimized parameters were compared with the experimental data at various heating rates. It is anticipated that the current work should be instructive for further kinetic analysis of catalytic pyrolysis of herb residues.

### 2.5.3 Discretization methods

Discretization is an essential pre-processing technique used in many knowledge discovery and computational problems. Its main goal is to transform a set of continuous attributes into discrete ones, by associating categorical values to intervals and thus transforming quantitative data into qualitative data. The governing equations can be solved by different discretization methods, including finite element method, finite volume method, finite difference method and the Lattice Boltzmann method. The first three methods could be seen as the same type in computational fluid dynamics (CFD), since they solve the governing equations by considering the particle flow as continuum.

#### ***Finite element methods:***

The finite element method (FEM) is a basic discretization method when solving the CFD problem. This method treats a continuous domain into discrete elements and compute the governing equations in each small domain. It is important to consider the initial conditions and the boundary conditions of the computing domain. It is handled by approximating the fields within each element as a simple function, such as a linear or quadratic polynomial, with a finite number of degrees of freedom (DOFs). This gives an approximate local description of the physics by a set of simple linear (but sometimes nonlinear) equations. When the contributions from all elements are assembled. Then, a large sparse matrix equation system that can be solved by any of a number of well-known sparse matrix solvers. The FEM is generally applied to the mechanical engineering discipline, like the aeronautical, biomechanical and automotive industries, to optimize and improve their design. Shi et al. [148] applied the FEM into biomass pyrolysis modelling analysis. They simulated the physical and chemical processes of the biomass particle pyrolysis using the finite element analysis software, which is called COMSOL Multiphysics 5.0. This software package was used to solve the ordinary differential equations and partial differential equations involved in the kinetic and particle models.

#### ***Finite volume methods:***

The finite volume method (FVM) is similar to the finite-element method in that the CAD model is first divided into very small but finite-sized elements of geometrically simple shapes. Apart



from this, the finite-volume method is very different from the finite-element method, beginning with the concept of elements, which are instead referred to as cells. The finite-volume method is based on the fact that many physical laws are conservation laws—what goes into one cell on one side needs to leave the same cell on another side. Following this idea, you end up with a formulation that consists of flux conservation equations defined in an averaged sense over the cells. Historically, this method has been very successful in solving fluid flow problems. Perera and Narayana [149] applied this method into biomass particle pyrolysis analysis to predict the effect of surrounding conditions on particle behaviour during conversion.

***Finite difference methods:***

The finite difference method (FDM) is also a discretization method using in CFD problem. This method only works well in solving the regular geometry problem. The FDM is the most direct approach to discretizing partial differential equations. We can consider a point in space where we take the continuum representation of the equations and replace it with a set of discrete equations, called finite-difference equations. The finite-difference method is typically defined on a regular grid and this fact can be used for very efficient solution methods. The method is therefore not usually used for irregular CAD geometries, but more often for rectangular or block-shaped models. The scheme of FVM in solving CFD problem is:

$$\frac{\partial Q}{\partial t} + \frac{\partial F}{\partial x} + \frac{\partial G}{\partial y} + \frac{\partial H}{\partial z} = 0 \quad (2-1)$$

***Lattice Boltzmann methods:***

The Lattice Boltzmann method (LBM) is originally from the Lattice Gas Automata (LGA) theory. It treats the fluid flow as the microscopic particle flow and the particles experience a series of collisions. The basic equation of LBM can be derived:

$$f_i(\vec{x} + \vec{e}_i \cdot t, t + \Delta t) - f_i(\vec{x}, t) = -\frac{1}{\tau} \left( f_i(\vec{x}, t) - f_i^{eq}(\vec{x}, t) \right) + S_i(\vec{x}, t) \quad (2-2)$$

Where  $f_i(\vec{x}, t)$  is the fluid density distribution function,  $S_i(\vec{x}, t)$  is a source term added into the LB equation,  $\tau$  is the relaxation time which related to the kinetic viscosity. The  $\vec{x}$  and  $\vec{e}_i$  are the position and discrete velocity vectors, respectively. The  $f_i^{eq}(\vec{x}, t)$  is the equilibrium distribution function (EDF) and it is expressed as:

$$f_i^{eq}(\vec{x}, t) = w_i \rho \left[ 1 + \frac{\vec{e}_i \cdot \vec{u}}{c_s^2} + \frac{(\vec{e}_i \cdot \vec{u})^2}{2c_s^4} - \frac{\vec{u}^2}{2c_s^2} \right] \quad (2-3)$$

Where  $w_i$  is the weighing coefficient in  $i$ th direction,  $\rho$  is the macroscopic density and  $c_s$  is the

sound speed which can derived from lattice speed.

*Table 2-9: Discretization methods.*

| Discretization methods                      | Merits  | Drawbacks   |
|---|---|---|
| Finite element method (FEM) [148, 150, 151] | Can solve complex geometry model;<br>High accuracy;   | Require large computer memory than FVM;<br>Highly depend on mesh quality; |
| Finite volume method (FVM) [152]            | Save computing time;<br>Easy to programme in CFD problem;   | Need more effort on solving the complex geometry problem;                 |
| Finite difference method (FDM) [153]        | Easy to programme;<br>Fast compute time;<br>Can solve complex geometry and get accurate results;  | Not good in solving the irregular geometry problem;<br>Less accuracy;     |
| Lattice Boltzmann method (LBM) [154, 155]   | Efficiency in solving the transport behaviour between biomass particles;<br>Efficiency in solving the complex boundary problem;<br>Suitable for massive parallel computing; | Complicated programming;  |

#### 2.5.4 Single particle model

After pre-treatment process, most of biomass particles are non-uniform shape (non-spherical, flake-like and resemble cylindrical shape). In the computational simulation area, different particle shape influences the accuracy of the results. The particle size influences the internal heat transfer gradients and the biomass conversion behaviour. The burning rates of large particles are always limited by the diffusion rates, thus, the surface area to volume ratio of biomass particles is important for predicting the conversion time [53]. The effects of biomass properties, like porosity, size and shape, density, and thermal conductivity were considered. Since complex sub-conversions involved in the thermal conversion process, such as the evaporation and devolatilization process, particle shrinkage and swelling, and secondary pyrolysis reactions, appropriate simplifications and assumptions should be considered in the simulation. For example, one-dimensional single particle models were modelled with following assumptions [20, 28]: (1) One-dimension conversion process (ignoring porous and asymmetric nature); (2) Uniform temperature between different phases; (3) Negligible pressure gradient inside the particle (porosity considered); (4) Laminar flow. This section summaries the modelling methods of particle model and the current models considering different assumptions.

In chemical engineering, models are used to effectively quantify the mass and heat transfer within the particle and between particles. There are several types of models, which determine the mass transfer and heat transfer between the particles for different variables such as particle aggregation, conduction, radiation et cetera. The single particle model; SPM revolves on the rates of heat and mass transfer within particles in this case ash, moisture and char. The rates are used to observe the effect of a variable such as particle diameter or temperature over time at a constant density.

However, the SPM is noted as the simplest of models due to relating the heat and mass transfer with a rate constant which will produce values from any point of the particle. This means that the SPM assumes that the particles are spherical and do not vary in size or distribution. The SPM can be used to understand the interaction of particles and the general trends of variables at controlled measures. Thus, the SPM is usually a platform to base further conditions. An example of further conditions is the particle growth term which is included within a highly developed Population Balance Model (PBM) (Soares and McKenna, 2013). For this study, the SPM is developed first in order to understand the effect of variables on woody particles at constant density. After pre-treatment process, most of biomass particles are non-uniform shape (non-spherical, flake-like and resemble cylindrical shape). In the computational simulation area, different particle shape influences the accuracy of the results. The particle size influence the internal heat transfer gradients and the biomass conversion behaviour. The burning rates of large particles are always limited by the diffusion rates, thus, the surface area to volume ratio of biomass particles is important for predicting the conversion time [53].

Many researchers use modelling method to study the thermal conversions behaviour of single biomass particle. The effects of biomass properties, like porosity, size and shape, density, and thermal conductivity were considered. Since complex sub-conversions involved in the thermal conversion process, such as the evaporation and devolatilization process, particle shrinkage and swelling, and secondary pyrolysis reactions, appropriate simplifications and assumptions should be considered in the simulation. Single particle models were always modelled with the following assumptions [20, 28]:

- One-dimension conversion process;
- Uniform temperature between different phases;
- Negligible pressure gradient inside the particle (porosity considered);
- Laminar flow;

One-dimensional models are generally used in the simulation to study the intra-particle heat and mass transfer performance. Lu et al. [4] investigated the effects of particle shape and size on combustion behaviour using one-dimensional single particle model. There were few 2-

dimensional and 3-dimensional models in current research since the complex assumptions. Yang et al. [129] developed a two-dimensional cylindrical model to study the biomass combustion behaviour. They used a range size of biomass particles and demonstrated the release of the combustion feature and tar production as the increase of temperature. The model proposed by Porteiro et al. [156, 157] introduced a specific discretization scheme which treated the 3D model as 1D model. Interior-particle processes (drying, devolatilization and char reactions), exterior-particle processes (diffusional and convective transport), and particle shrinkage were considered in this model. Ciesielski et al. [82] constructed a three-dimensional near-cylindrical particle model with porous structure to study the heat and mass transfer behaviour. Table 2-10 lists a summary of single particle models of considering different morphology of biomass particle.

*Table 2-10: Considered biomass particle morphology in selected single particle models.*

| Model | Particle type                    | Particle size                             | Porosity       | Shrinkage      | Anisotropy | Process         | Scope  |
|-------|----------------------------------|---|----------------|----------------|------------|-----------------|--|
| [156] | Wood cylinder particle           | 300mm long and 25mm radius for validation | Considered     | Considered     | No         | Combustion      | Particle homogeneity and isotropy assumption; Predicting the conversion properties of biomass;         |
| [158] | Wood particle: palm kernel shell | 1mm, 2mm, 4mm, 10mm                       | Not considered | Considered     | No         | Combustion      | Demonstrating the particle size effect on the combustion behaviour;                                    |
| [159] | Spherical beech wood particle    | 0.5mm-3mm                                 | Considered     | Not considered | No         | Combustion      | Predicting the combustion behaviour of a series of particle size;                                      |
| [160] | Wood slab particle               | Half thickness 5 $\mu$ m-2cm              | Considered     | Considered     | No         | Pyrolysis       | Examining the effect of the shrinkage (0.1-0.4) and moisture (0-30%) on pyrolysis products separately; |
| [20]  | Symmetric sphere particle        | 2mm-20mm                                  | Considered     | Not considered | No         | Gasification    | Predicting the conversion time the weight loss rate and the temperature distribution;                  |
| [28]  | Wood particle (sphere /slab/     | 100 $\mu$ m-1000 $\mu$ m                  | Considered     | Not considered | No         | Flash pyrolysis | Predicting the product yield   |

|       |                                    |  |                |                |  |                |  |
|-------|------------------------------------|--|----------------|----------------|--|----------------|--|
|       | cylinder)                          |  |                |                |  |                | for different particle shapes;   |
| [129] | Cylinder particle                  | 10 $\mu$ m-20mm  | Considered     | Considered     | No   | Combustion     | Demonstrating the simple models can assuming the biomass combustion behaviour; Results are accurate for small particles; |
| [161] | Spherical model                    | 0.125mm-5mm  | Not considered | Not considered | No   | Fast pyrolysis | Predicting the mass loss rate of single particle by modelling and experiment;  |
| [162] | Sphere/Slab/Cylinder               | Sphere: 2.54cm;<br>Cylinder:2 $\times$ 3cm;<br>Slab:1mm; | Considered     | Considered     | Yes,<br>anisotropy<br>boundary<br>conditions | Pyrolysis      | Presenting the pyrolysis behaviours of different shapes of anisotropy biomass particles;                                 |
| [163] | Large wood particles               | -  | Considered     | Considered     | No   | Pyrolysis      | Studying the pyrolysis mechanisms of large wood particles;   |
| [164] | Cylinder wood particle             | 6mm diameter and 16.5mm length                           | Considered     | Considered     | No   | Combustion     | Evaluating the single particle   |
| [165] | 1D Layered model                   | 50mm   | Considered     | Considered     | No   | Combustion     | Analysing the required modelling specifications for single particle pyrolysis;   |
| [80]  | Microstructural cylinder model     | 40 $\mu$ m-500 $\mu$ m                                   | Considered     | Not considered | Yes  | -              | Demonstrating the conversion behaviour of microstructural structure;   |
| [166] | Thermally thick wood slab particle | 5 $\mu$ m-5cm  | Considered     | Considered     | No   | Pyrolysis      |  |

### 2.5.5 Particle size and shape modelling

One of the simplifications of the biomass particle morphology is spherical assumption of particle model. L  d   [99] reviewed the drawbacks of simplified spherical model, that is, the simple model ignored the biomass thermal properties varied with direction and the heat transfer behaviour changed with pores exist in the biomass particles. Another simplification is to use the uniform size to present the particle size distribution, which obtained from the milling or grounding process. In realistic, particle size distribution have distinct effect on the biomass thermochemical conversion (details in Section 2.4). Particle size determines the distance that external heat transfer to the center of the particle, which therefore has an effect on the kinetic rate, so approximating the particle to one size cannot represent a true thermochemical conversion process. Researchers had investigated the limitations of this kind of simplification [86, 166, 167].

The ansymmetric nature of biomass particles was considered by many researches. For example, the ‘‘wave-like’’ character of the particle during pyrolysis was studied by Di Blasi [168]. It was assumend that biomass property functions varied in different direction. Two-dimensional contour plots were shown as Figure 2-20.

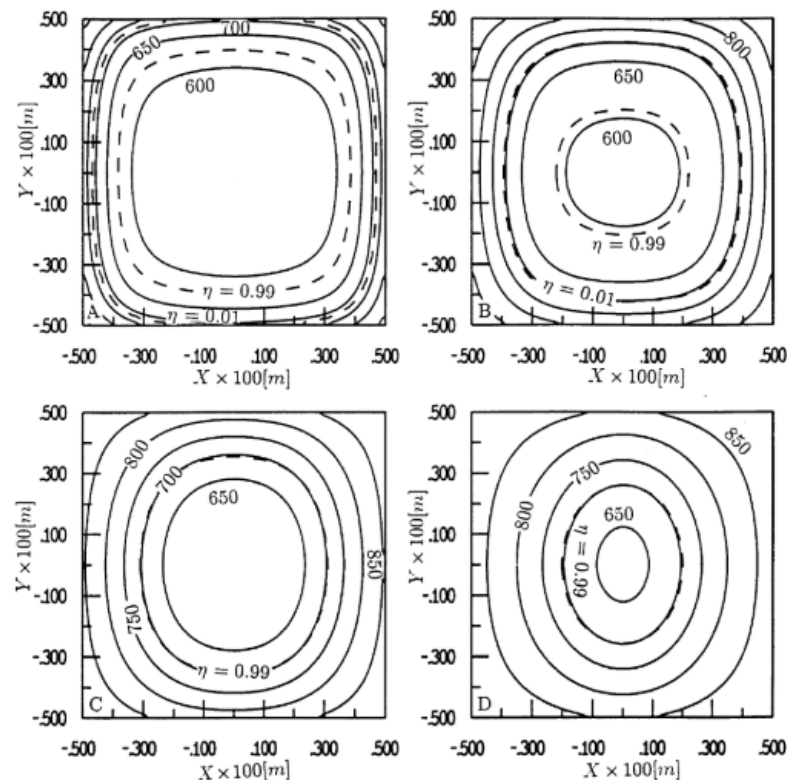


Figure 2-20: Wave-like character. Isotherms [K]. (Solid lines, step number=50; Dashed lines, constant contour level of temperature variable  $\eta$ ) [168].

An updated model studying the anisotropic behaviour of particle in different direction of

cylindrical particle was studied by Gentile et al. [162], considering the anisotropic geometry effect and the particle shrinkage. They developed a 3-dimensional model of cylinder biomass particle and made a comparison of particle shape evolution between the simulation and the experimental data (Figure 2-21).

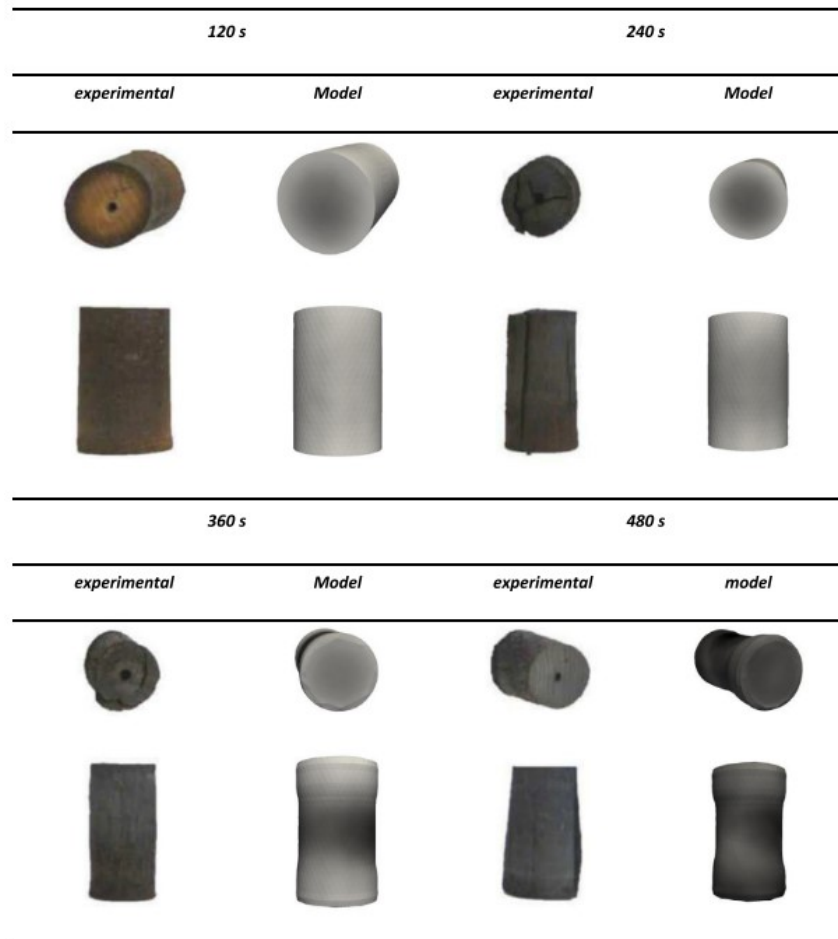


Figure 2-21: Particle shape evolution [162].

### 2.5.6 Shrinkage simulation of single biomass particle

The shrinkage of the biomass during conversion is a big challenge in numerical simulation. With the particle shrinking, many properties of the biomass particle change as well, such as the porosity and the density. Wang et al. [169] investigated the influence of thermal pre-treatment temperatures on wood biomass biochemical compositions, physical properties and microstructure by using wild cherry wood samples. They found that dimensions of the wood were reduced in all directions and shrinkage increased with increased treatment temperature and weight loss. With increased treatment temperature, losses of weight and volume increased, and bulk density decreased. Chemical restructuring during the pyrolysis reactions results in shrinkage of the solid matrix. [160] defined shrinkage as the ratio between the reduced dimension and the original dimension. Table 2-11 summarizes the shrinkage factor of single

particle model.

Table 2-11: Summary of single particle model volume shrinkage factor.

| Type             | Expression   | Features   | Literature |
|------------------|--|--|------------|
| Conversion time  | $\frac{1}{\Delta L_k} \frac{d\Delta L_k}{dt} = \frac{1}{V_p} \frac{dV_p}{dt} n_k$ <p><math>\Delta L</math> is the cell dimension, <math>n</math> is the direction factor, and <math>k</math> represents either one of the two coordinates;</p>   | Isotropic model, particle volume shrinks as the conversion processes proceed (time);                                       | [129]      |
| Conversion temp. | $s_{r,char} = (-1 + 0.00395T_{ext} - 2.62 \times 10^{-6}T_{ext}^2) \times m_{char}/m_0$ $s_{z,char} = (-4.7 + 0.0108T_{ext} - 5.86 \times 10^{-6}T_{ext}^2) \times m_{char}/m_0$ <p><math>T_{ext} &gt; 723</math> K<br/> <math>s_{z,char} = 0 \quad T_{ext} &lt; 723</math> K</p> <p><math>s_i</math> are shrinkage factors on different coordinates;<br/> <math>m</math> represents the mass;</p>   | A radial shrinkage factor is defined;  | [78]       |
| Empirical value  | $\frac{v}{v^0} = 1 + x_M(\beta_M - 1.0) + x_B(\beta_B - 1.0) + x_C(\beta_C - 1.0)$ <p><math>v</math> is the particle volume;<br/> <math>x_m, x_B, x_C</math> are conversion of moisture, biomass, and char;<br/> <math>\beta_M</math> is the shrinking factor for moisture drying (<math>\beta_M=0.9</math>);<br/> <math>\beta_B</math> is shrinking factor of decolatilization (<math>\beta_B=0.9</math>);<br/> <math>\beta_C</math> is char buring shrinkage factor (<math>\beta_C=0</math> at beginning stage);</p> | The particle shrinks slightly during drying and shrinks more rapidly during char burning;                                  | [28]       |
|                  | Shrinkage computed along the process (1% each time, 20% total);  | Shrinkage results from char consumption;   | [156]      |
|                  | 10% total;   | No shrinkage occurs at drying and pyrolysis stage, size shrinkage occurs at char combustion stage;                         | [170]      |
|                  | $V = V_0 \cdot f_r^{y+1} \cdot f_l$ <p><math>f_r</math> and <math>f_l</math> are the shrinkage factors in radial and longitudinal direction;</p>   | Final shrinking factors obtained from experiment for cylinder are $f_r=8\%$ , $f_l=10\%$ ; For sphere $f_r = f_l = 10\%$ ; | [134]      |
| Moisture         | $V_{Y_{ws}} = \frac{V_{dry}(1 - Y_{ws})}{1 - 1.28Y_{ws}}$ <p><math>V</math> is the particle volume, <math>Y</math> is the water content in the biomass;</p>  | The particle shrinkage results from the moisture evaporation;  | [165]      |



### 2.5.7 Population balance model

The Population Balance Model (PBM) of biomass particles is an updated model of single particle model. It overcomes the limitations of traditional one-dimensional single particle model. Population balance approach is generally used to describe the transformation of a group of particles with size distribution during the particle processing, such as the granulation, crystallisation and fluidization [171]. During the thermochemical conversion process, the biomass particles experienced a series of change in particle size and shape, including shrinkage, swelling and breakage (reasons showed in Section 2.5.2). There are four fundamental evolution occur in the particle group: breakage, nucleation, growth and aggregation (as shown in Figure 2-22). The breakage is a set of processes where particle size is reduced whilst producing smaller particles. The nucleation is the process where the new particles are formed from the matter which is not recognised as particulate matter. The growth is the process that non-particulate matter becomes incorporated within a particle. The aggregation is the process by which larger particles are formed from the joining of smaller particles.

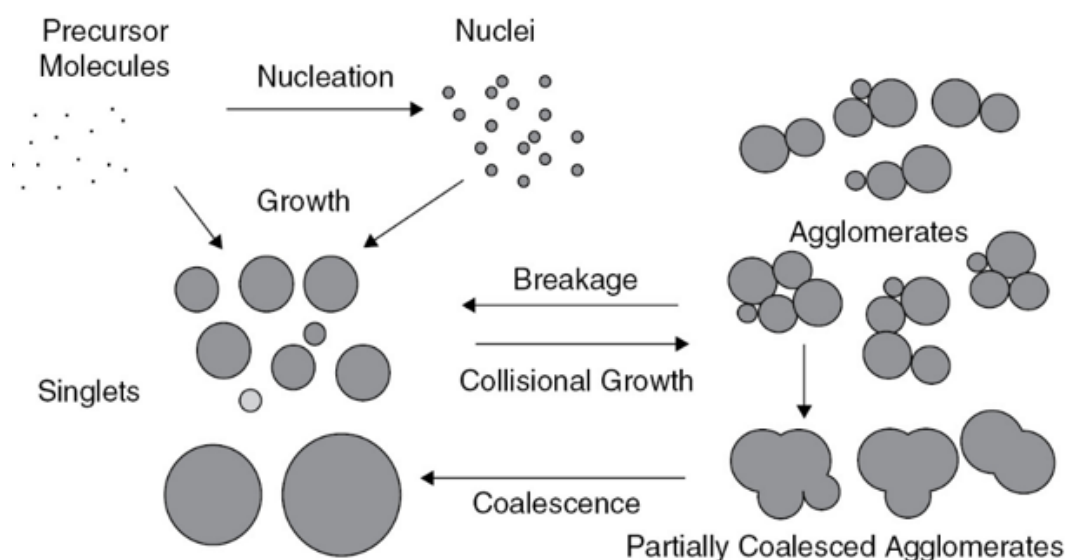


Figure 2-22: Particle evolution mechanisms [172].

The first derivations of population balance model were presented by Hulburt & Katz [173] and Randolph [174] in 1964. Since then, the PBM had been introduced into the process modelling area, including the granulation and crystallisation [175, 176]. However, the use of PBM was rarely introduced into the thermochemical conversion process of biomass. Gil et al. [177] introduced the population balance approach for the biomass particles after milling process, considering the particle breakage to predict the final particle size distribution. Yu et al. [178] studied the population balance equations by developing an optimal Monte Carlo sampling

method. They found that the accuracy of solutions was related to the initial sample number, replicated number and section number. The PBM of biomass particles for gasification process in fluidized-bed was developed by Natale et al. [179]. Two types of mechanisms of size shrinkage were considered: abrasion and fragmentation. In this model, they used the lognormal probability density function to describe the particle size distribution:

$$p_0^* = \frac{1}{d\sqrt{2\pi} \ln \sigma} \exp \left[ -\frac{1}{2} \left( \frac{\ln(d/\mu)}{\ln \sigma} \right)^2 \right] \quad (2-4)$$

Where  $\mu$  represents the mean value and  $\sigma$  is the standard deviation.

In the modelling of the thermochemical conversion process of biomass particles, the properties of different particles will change with the position and simulating time. At first, the PBM is developed by considering the single particle properties, including the particle self-characteristics which called “internal co-ordinates ( $x_i$ )” and the particle space characteristics which called “external co-ordinates ( $x_e$ )”. Then, the characteristics of particle group should be considered, such as the particle size distribution. Finally, the population balance equation (PBE) of a group of biomass particles can be derived by continuous functions. The PBE can describe the continuity of the particles and evolution of the size distribution. The PBM can be solved by Monte Carlo method. The basic principle of Monte Carlo approach is to generate a set of numbers randomly and input the results into the calculation system [178]. One of the advantages of Monte Carlo methods is their stochastic nature is harmonious with the nature of particle processing, and this produces robust results which reflect the process well. However, to improve the accuracy of Monte Carlo method solutions, many particles must be tracked, which also increases computational expense. Yu et al. investigated the accuracy of the PBM solved using Monte Carlo sampling method [180]. They found that the accuracy of the Monte Carlo sampling method could be measured by Squared Hellinger Distance ( $H^2$ ). The coefficient was related to the initial sample number, the bins’ number, and the number of replicates.

## **Chapter 3. Thermogravimetric characteristics and kinetics analysis**

### **3.1 Introduction**

Thermogravimetric characteristics analysis technique is widely used in studying the reaction mechanism of thermochemical conversion process in laboratory. Thermogravimetric analysis can not only obtain the kinetic parameters and reaction mechanisms through the change the weight loss curve, but also study the physical and chemical characteristics of the biomass [181]. The determination of activation energy was concluded by Starink [69, 142] using kinetic-free method. The kinetic-free method can offer basic kinetic parameters activation energy and pre-exponential factor. It is important to determine the significant mechanism function for comprehensive study of kinetic characteristics.

Since the reaction mechanisms are complex, it is inconvenient to describe the reaction function using current reaction schemes. This results from the unknown kinetic parameters cannot be obtained from traditional model-free methods [143-147]. To evaluate the kinetic parameters, the model-free method with Starink assumption could be applied to determine the activation energy without assuming a kinetic model of the process. The reaction can be described by one kinetic equation and the reaction rate is a constant value. The reaction mechanism and pre-exponential factor could be analysed by the generalized master-plots method. The model results could be optimized by comparing with the experimental data at various heating rates. It is expected that the current kinetic analysis work could be used as the guidance for the further analysis of the catalytic pyrolysis of herb residues.

In this section, the kinetic parameters and reaction mechanism of herb pyrolysis were calculated by using the generalized master-plots method, and the model results using the optimized parameters were validated by the experimental data at various heating rates. The catalytic behaviour of herb pyrolysis was also investigated by loading different amount of potassium salts on Chinese herb residues.

## 3.2 Experiment preparation and materials

The CHR powder (60 mesh) was selected in the experiment and purchased from Guangdong Jiuqi Ecological Environment Technology Co., Ltd. The raw material is a kind of woody CHR waste during the production of proprietary Chinese medicine manufactured by Guangdong Jiuhe Pharmaceutical Co., Ltd. Table 3-1 shows the proximate and ultimate analyses results of herb residue [182]

. The proximate and ultimate analyses of the herb powder are similar to the pine powder. The chemical reagents were analytical grade and purchased from Aladdin (Shanghai) Chemical Reagent CO., Ltd., the experimental gases were purchased from Guangzhou Yuejia Gas Co., Ltd., including high-purity nitrogen (purity  $\geq 99.999\%$ ), high-purity argon (99.999%) and other standard gases. Raw CHR contains low nitrogen (0.79 wt%) and high amount of volatiles (80.87 wt%) shown in Table 3-1, which indicates that the CHR material could be a desirable feedstock for thermochemical conversion [183]. Moreover, the ash content of raw CHR sample (3.37 wt%) is lower than the conventional biomass materials [143], such as wheat straw (6.01 wt%) and rape straw (5.63 wt%), which may be due to the fact that most of the soluble inorganic minerals will be removed from CHR during the decocting process, especially the potassium.

Table 3-1: Proximate and ultimate analyses of herb.

| Samples      | Proximate analyses (wt%) |       |        | Ultimate analyses (wt%) |           |           |             |
|--------------|--------------------------|-------|--------|-------------------------|-----------|-----------|-------------|
|              | $A_d$                    | $V_d$ | $FC_d$ | $C_{daf}$               | $H_{daf}$ | $N_{daf}$ | $O^*_{daf}$ |
| herb residue | 3.37                     | 80.87 | 15.76  | 46.91                   | 6.06      | 0.79      | 42.88       |

\*(by difference.)

In this work, the catalyst of potassium carbonate ( $K_2CO_3$ , 99.0 wt%) was loaded on the CHR powder by impregnation method as follows: firstly,  $K_2CO_3$  and deionized water were mixed to make a catalyst solution; and then slowly dripped into the dry herb residue and well stirred; finally, the sample was dried in an air-circulating oven at 378K for over 12.0 h, after aging at 273K for about 12.0 h in a refrigerator. The dried sample was crushed in an agate mortar, and the fractions of particle size  $< 60$  mesh was selected. According to the mass fraction of potassium, the samples loading  $K_2CO_3$  are marked as Herb-5%K, Herb-7%K and Herb-9%K, respectively. The raw CHR material was treated with a similar method, just replaced the catalyst solution with the same quality of deionized water and marked the dried CHR sample as Herb.

## 3.3 Research method

### 3.3.1 Thermogravimetric analysis

The TA SDT650 rapid temperature-increasing thermogravimetric analyzer manufactured by TA Instruments in U.S.A was used to carry out the thermogravimetric analysis of herb samples. About 5.00 mg of dry-based sample was placed in an Al<sub>2</sub>O<sub>3</sub> crucible. The gas flow rate of the high-purity nitrogen was 100 ml/min. The heating-up temperature is from 300 to 1125 K with different programmed heating rates ( $\beta_1=10$  K/min,  $\beta_2=20$  K/min,  $\beta_3=30$  K/min,  $\beta_4=40$  K/min).

The mass loss ratio is defined in Eq. (3-1)  $\Delta Mass_i = \frac{Mass\ loss\ at\ stage\ i}{Total\ mass\ loss} \times 100\%$

(3-1), which is the ratio of the mass loss at different stage to the total mass loss.

$$\Delta Mass_i = \frac{Mass\ loss\ at\ stage\ i}{Total\ mass\ loss} \times 100\% \quad (3-1)$$

Where  $i = 1, 2, 3$ , stands for pyrolysis stages: dehydration, devolatilization and carbonization respectively.

### 3.3.2 Kinetic parameter study

The Arrhenius dynamics formula applied in the solid-state biomass thermal decomposition kinetics could be described as Eq. (3-2) and Eq. (3-3):

$$\frac{d\alpha}{dt} = A \exp\left(-\frac{E_\alpha}{RT}\right) f(\alpha) \quad (3-2)$$

$$\alpha = \frac{m_0 - m_t}{m_0 - m_\infty} \quad (3-3)$$

Where the meanings of symbols are shown in Table 3-2.  $f(\alpha)$  is the differential mechanism function, depending on the reaction model (Table 3-3).

Table 3-2: Symbol meanings.

| Symbol     |  |
|------------|--|
| t          | Reaction time (s)                                      |
| $\alpha$   | Conversion rate (%)                                    |
| $m_0$      | Initial sample mass                                    |
| $m_t$      | Mass at the time t                                     |
| $m_\infty$ | Final sample mass                                      |
| A          | Pre-exponential factor of Arrhenius (s <sup>-1</sup> ) |
| $E_\alpha$ | Apparent activation energy (kJ/mol)                    |

|             |                                 |
|-------------|---------------------------------|
| $T$         | Kelvin temperature (K)          |
| $f(\alpha)$ | Differential mechanism function |
| $\beta$     | Heating rate                    |

For the non-isothermal kinetics ( $\beta = dT/dt, K \cdot s^{-1}$ ), introducing a constant heating rate  $\beta$  into the Eq. (3-4):

$$\frac{d\alpha}{dT} = \frac{A}{\beta} \exp\left(-\frac{E_\alpha}{RT}\right) f(\alpha) \quad (3-4)$$

The integrated mechanism function ( $G(\alpha)$ ) can be obtained from the integration of Eq. (3-5) and Eq. (3-6):

$$G(\alpha) = \frac{A}{\beta} \int_0^T \exp\left(-\frac{E_\alpha}{RT}\right) dT \quad (3-5)$$

$$G(\alpha) = \frac{AE_\alpha}{\beta R} P(u) \quad (3-6)$$

In Eq. (3-6), the  $P(u)$  is considered as temperature integral, in which  $u = E_0/(RT)$ ,  $E_0$  is the average activation energy. Although there is no common-sense analytical solution for the temperature integral function  $P(u)$ , a number of methods have been developed [184]. Starink [142] summarized the pros and cons of different integral approximation methods, including Kissinger, Ozawa and Boswell equations. Then he proposed an accurate non-isothermal method to determine the activation energy through multi heating rates and model-free kinetics. The Starink's approximation [142, 185] of the temperature integral equation in the range of  $20 \leq u \leq 60$ , is given as:

$$P(u) = \frac{\exp(-1.0008u-0.312)}{u^{1.92}} \quad (3-7)$$

The apparent activation energy could be given by:

$$\ln \frac{\beta}{T^{1.92}} = -1.0008 \frac{E_\alpha}{R} \frac{1}{T} + \ln \frac{A R^{0.92}}{G(\alpha) E_\alpha^{0.92}} - 0.312 \quad (3-8)$$

It is clear that there is a linear relationship exists between  $1/T$  and  $\ln(\beta/T^{1.92})$ . Thus, the activation energy  $E_\alpha$  at the conversion rate  $\alpha$  can be obtained from the slope of the curve by plotting the linear fitting curve of  $1/T$  against  $\ln(\beta/T^{1.92})$  for the whole conversion process. The master plots are used for determining the reaction model. The experimental data are compared with the theoretical curves to determine the reaction model.

Based on the model-free kinetic results, the generalized master-plot method was used for the determination of the reaction model and its mechanism function by comparing experimental data with the theoretical master curves. Master-plot method is based on the integral mechanism function ( $G(\alpha)$ ) shown in Table 3-3. From the integral kinetic equation, Eq.(3-6) and Eq. (3-7),

at reference point  $\alpha = 0.5$ , the following equation is obtained [186]:

$$\frac{G(\alpha)}{G(0.5)} = \frac{P(u)}{P(u_{0.5})} \quad (3-9)$$

The suitable pyrolysis reaction mechanism is the master-plot curve which best represents the experimental data, once  $G(\alpha)$  has been determined, the pre-exponential factors ( $A_\alpha$ ) can be estimated from the Eq. (3-8).

Table 3-3: Ten different widely used mechanism functions of solid-state reaction models [187].

| Mechanism Models                 | Symbol | $f(\alpha)$                                    | $G(\alpha)$                       |
|----------------------------------|--------|--|-----------------------------------|
| Contracting area                 | R2     | $(1-\alpha)^{1/2}$                             | $2[1-(1-\alpha)^{1/2}]$           |
| Contracting volume               | R3     | $(1-\alpha)^{2/3}$                             | $3[1-(1-\alpha)^{1/3}]$           |
| Nucleation (Johnson-Mehl-Avrami) | Am     | $m(1-\alpha) [-\ln(1-\alpha)]^{1-1/m}$         | $[-\ln(1-\alpha)]^{-1/m}$         |
| 1-D diffusion                    | D1     | $1/(2\alpha)$                                  | $\alpha^2$                        |
| 2-D diffusion                    | D2     | $[-\ln(1-\alpha)]^{-1}$                        | $\alpha+(1-\alpha) \ln(1-\alpha)$ |
| 3-D diffusion-Jander             | D3     | $[(3/2)(1-\alpha)^{1/3}]/[1-(1-\alpha)^{1/3}]$ | $[1-(1-\alpha)^{1/3}]^2$          |
| Ginstling-Brounshtein            | D4     | $(3/2)/[(1-\alpha)^{1/3}-1]$                   | $(1-2\alpha/3)-(1-\alpha)^{2/3}$  |
| First-order reaction             | L1     | $1-\alpha$                                     | $-\ln(1-\alpha)$                  |
| Second-order reaction            | L2     | $(1-\alpha)^2$                                 | $(1-\alpha)^{-1}-1$               |
| Third-order reaction             | L3     | $(1-\alpha)^3$                                 | $[(1-\alpha)^{-2}-1]/2$           |

## 3.4 Results and discussion

### 3.4.1 Thermogravimetric analysis

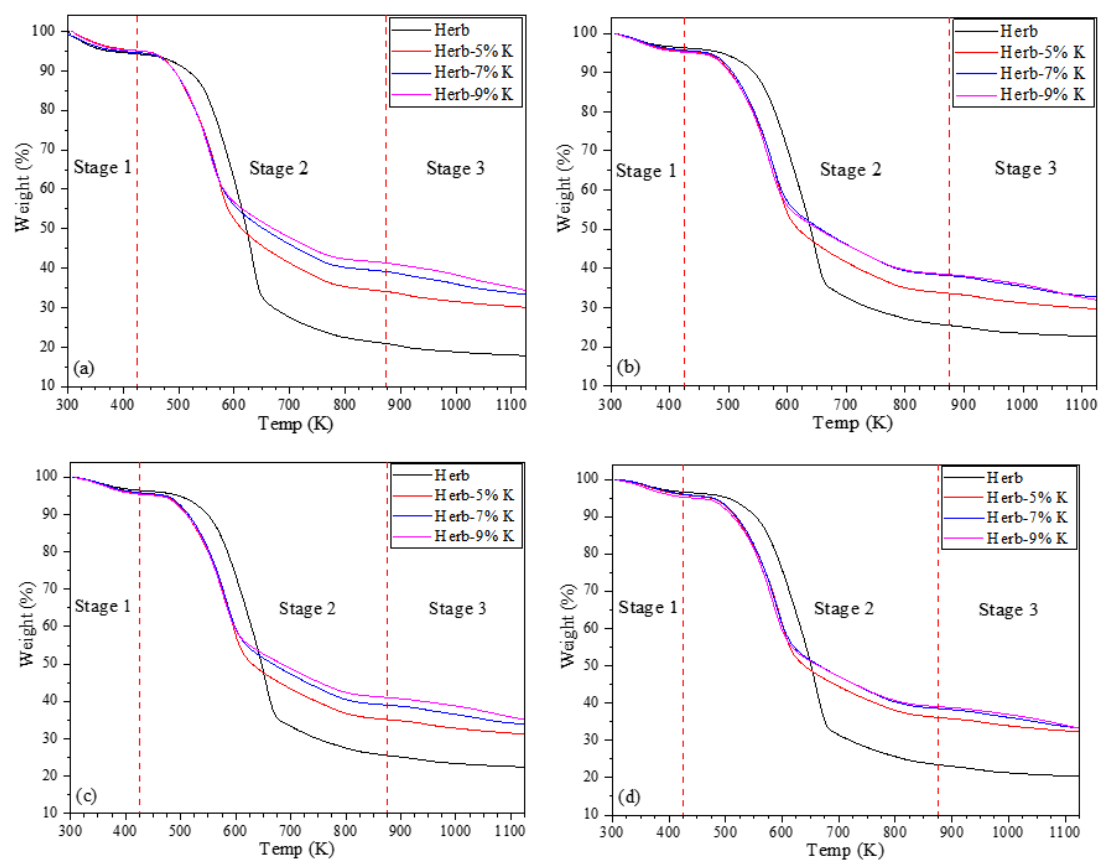


Figure 3-1: TG curves of herb samples with different  $K_2CO_3$  loadings at (a) 10 K/min (b) 20 K/min (c) 30 K/min (d) 40 K/min.

Figure 3-1 shows the TG curves of CHR powders loading different proportions of  $K_2CO_3$  catalyst at different heating rates of 10-40 K/min. At any of the four heating rates, the catalytic pyrolysis process of herb can be divided into three stages [143]: Stage1-dehydration, Stage2-devolatilization and Stage3-carbonization. Table 3-4 lists the normalized mass loss of CHR for different samples:  $\Delta Mass_1$  (4.23 wt%- 7.94 wt%),  $\Delta Mass_2$  (82.02 wt%- 91.83 wt%) and  $\Delta Mass_3$  (3.68 wt%- 10.53 wt%) for three stages of the catalytic pyrolysis at different heating rates. The first stage is from 300K to 425K, which is mainly due to the removal of bound water and desorption of adsorbed gases and light volatiles, and it is usually called as dehydration. The second stage is from 425K to 875K, which is the major region for pyrolysis process as over 82.02% mass loss occurs, where most of the volatiles were decomposed and released. The last stage is carbonization at temperature above 875K, mainly dominated by the degradation of carbonaceous residues with little mass loss about 3.68%-10.53% [143].



Table 3-4: Normalized mass loss of CHR with different  $K_2CO_3$  loadings determined by TGA.

| Sample   | $\Delta Mass_1, \%$ |           |           |           |                           | $\Delta Mass_2, \%$ |           |           |           |                            | $\Delta Mass_3, \%$ |           |           |           |                           |
|----------|---------------------|-----------|-----------|-----------|---------------------------|---------------------|-----------|-----------|-----------|----------------------------|---------------------|-----------|-----------|-----------|---------------------------|
|          | $\beta_1$           | $\beta_2$ | $\beta_3$ | $\beta_4$ | Mean                      | $\beta_1$           | $\beta_2$ | $\beta_3$ | $\beta_4$ | Mean                       | $\beta_1$           | $\beta_2$ | $\beta_3$ | $\beta_4$ | Mean                      |
| Herb     | 6.91                | 4.77      | 4.55      | 4.23      | <b>5.12</b><br>$\pm 1.22$ | 89.41               | 91.57     | 91.47     | 91.83     | <b>91.70</b><br>$\pm 1.12$ | 3.68                | 3.66      | 3.98      | 3.91      | <b>3.81</b><br>$\pm 0.16$ |
| Herb-5%K | 6.96                | 6.50      | 6.21      | 6.05      | <b>6.43</b><br>$\pm 0.40$ | 87.33               | 87.91     | 88.21     | 88.37     | <b>87.97</b><br>$\pm 0.46$ | 5.45                | 5.60      | 5.61      | 5.58      | <b>5.56</b><br>$\pm 0.07$ |
| Herb-7%K | 7.94                | 6.47      | 6.30      | 5.98      | <b>6.67</b><br>$\pm 0.87$ | 83.28               | 85.36     | 85.93     | 86.21     | <b>85.19</b><br>$\pm 1.32$ | 8.77                | 8.16      | 7.77      | 7.80      | <b>8.13</b><br>$\pm 0.46$ |
| Herb-9%K | 7.45                | 7.08      | 7.02      | 7.07      | <b>7.16</b><br>$\pm 0.20$ | 82.02               | 83.39     | 83.81     | 84.20     | <b>83.36</b><br>$\pm 0.95$ | 10.53               | 9.53      | 9.17      | 8.74      | <b>9.49</b><br>$\pm 0.76$ |

\* The heating rates is  $\beta_1=10$  K/min,  $\beta_2=20$  K/min,  $\beta_3=30$  K/min,  $\beta_4=40$  K/min.

As a kind of special biomass waste, CHR mainly contains hemicelluloses, cellulose and lignin as well. Their DTG curves (Figure 3-2) show the typical pyrolysis characteristics of lignocellulosic biomass in the devolatilization stage, which could be distinguished into two individual phases [145]: main devolatilization phase (425–700K for original herb sample, and 425–650K for catalytic samples) and continuous slight polycondensation phase (700–875 K for original herb sample, and 650–875K for catalytic samples), respectively. The normalized mass loss of CHR for this stage is determined by TGA data from 425–900K. The first phase is a rapid weight-loss process, in which a large amount of volatile matter is released quickly. Generally, hemicelluloses and cellulose had high reactivity and could be completely decomposed in this phase [188], and the weight loss peaks of these two substances overlapped in DTG. For the second phase (>700 K), however, the TG curves decline slowly, and the DTG curves only show slight shoulder peaks with long tails. This is primarily due to the pyrolysis process of lignin with a relatively stable structure [189], and the slight polycondensation of the unstable bio-chars at a very slow pyrolysis rate [190]. Comparing the TG&DTG curves of CHR with different  $K_2CO_3$  loadings, it is clear that  $K_2CO_3$  catalysts made the TG&DTG curves move to the low temperature region comparing with the raw CHR sample, similar with the catalytic pyrolysis of cotton stalk [191] and sawdust [69].

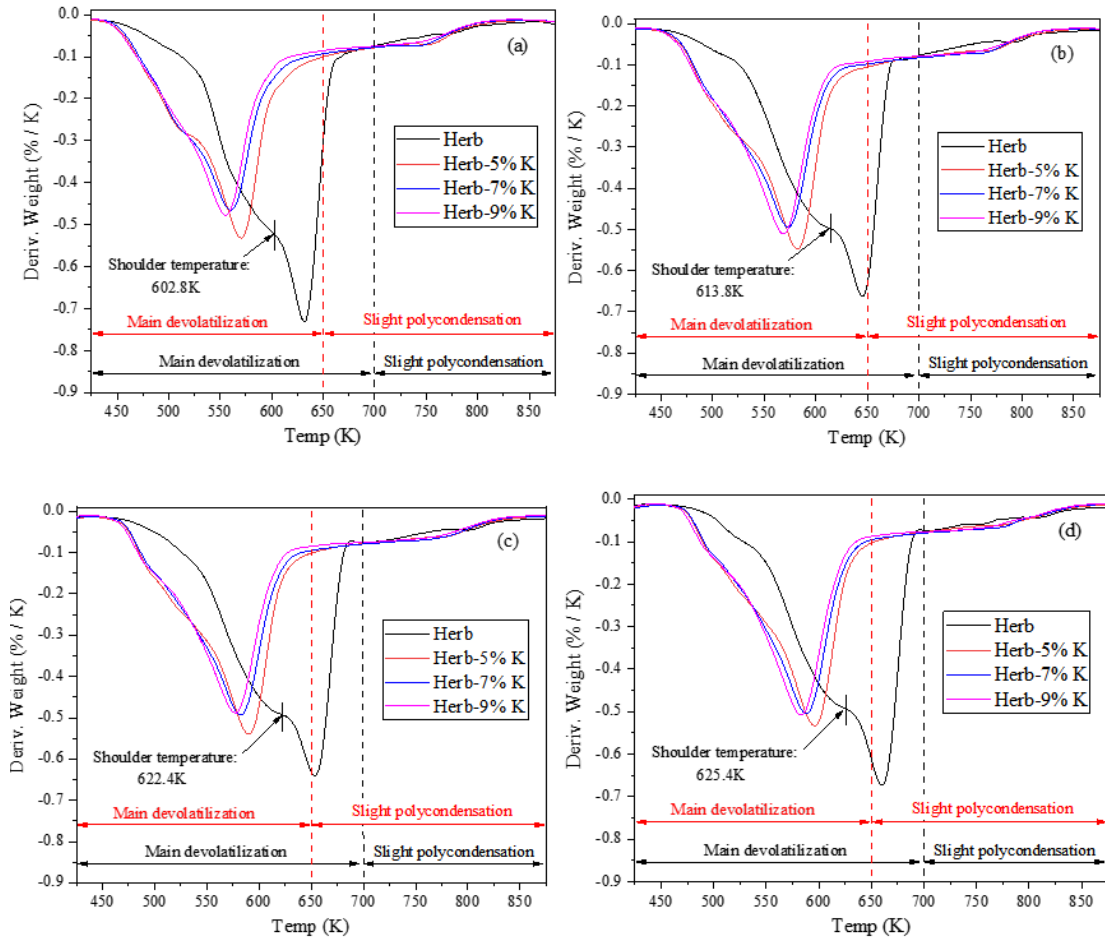


Figure 3-2: DTG curves of herb samples with different  $K_2CO_3$  loadings at (a) 10 K/min (b) 20 K/min (c) 30 K/min (d) 40 K/min.

Further analysis of the devolatilization stage is depicted by the second derivative of TG data (DDTG, Figure 3-3). Corresponding to the temperature points where  $d^2m_t/m_0/dT^2$  is near to zero in DDTG profiles, the devolatilization stage could be further divided into three subsections: *Section I* (425-615K for raw CHR, 425-525K for CHR with  $K_2CO_3$ ), *Section II* (615-700K for raw CHR, 525-650K for CHR with  $K_2CO_3$ ) and *Section III* (700-875K for raw CHR, 650-875K for CHR with  $K_2CO_3$ ), corresponding to the thermal decomposition of the three pseudo components: hemicellulose, cellulose and lignin [6]. According to the temperature points in DDTG profiles corresponding to the local minima, one kind of shoulder peaks in DTG curves could be found in *Section I* owing to the decomposition of hemicelluloses [6], and it is defined as  $T_s$  for the temperature corresponding to the shoulder peak. Another kind of sharp peaks in DTG curves appear in *Section II*, which attribute to the degradation of cellulose and partial depolymerization of lignin [61], and the temperature corresponding to the maximum DTG peak is defined as  $T_{max}$ . At high temperatures, the nearly horizontal straight lines appear

in Section III, which attribute to the long tails with low weight loss rate in the DTG curves, relating to the slight polycondensation of aromatic rings in the complex structures of lignin [189].

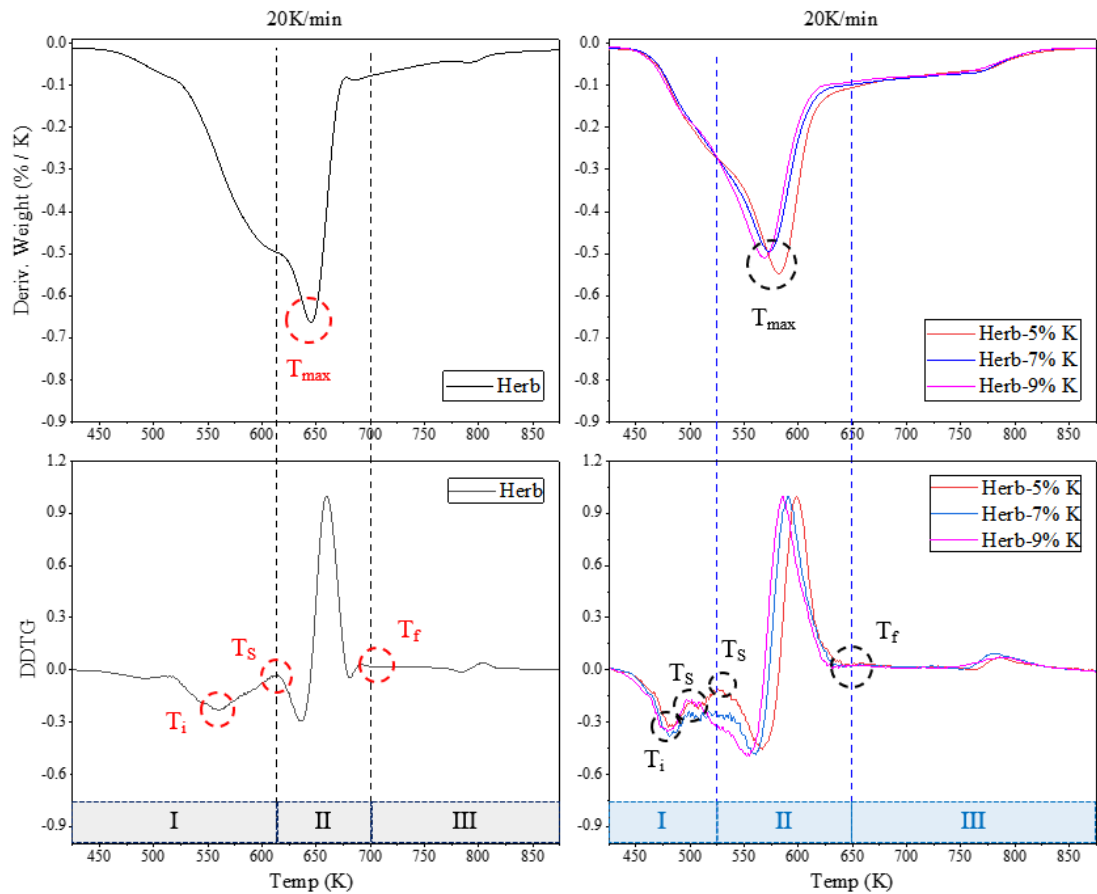


Figure 3-3: DTG profile and DDTG profiles of the devolatilization stage of CHR samples with different  $K_2CO_3$  loadings at 20 K/min. (Section I&II belong to the main devolatilization phase)

### 3.4.2 Activation energy

To accurately predict the catalytic pyrolysis characteristics in the main devolatilization phase, a model-free method of Starink is applied to analyze the kinetic parameters of CHRs loaded with different proportions of  $K_2CO_3$ . The specific calculation method of activation energy has been described in Section 3.3. The conversion rate ( $\alpha$ ) ranging from 0.1 to 0.8 with a step-size of 0.02 is adopted in this work. As shown in Figure 3-4, the curves for all samples have the similar trend: the  $\ln(\beta/T^{1.92})$  is linearly related with the  $1/T$ , and the slope of which is calculated to obtain the activation energy  $E_\alpha$ . For  $\alpha=0.1-0.8$ , the values of regression variance ( $R^2$ ) should be all exceed 0.99 (Table 3-5), indicating that the activation energies are relatively accurate.  $K_2CO_3$  catalyst significantly reduce the activation energy, and the pyrolysis characteristics of

CHR samples are changed with the increase of the K concentration. However, satisfactory agreement is found on activation energies distribution between K-7% and K-9% samples, for their curves are almost overlapping with less than 2.74% deviation, which suggests that the suitable additive proportion of potassium should be about 7.0 % for the CHR material.

Figure 3-4 is the kinetic plots of apparent activation energy. Figure 3-5 is the variation of activation. The values of  $R^2$  and  $E_a$  become a little more volatile in higher conversions ( $\alpha > 0.70$ ) for CHR samples with  $K_2CO_3$ . The small discrepancy should be caused by the combined effects of secondary reactions, diffusion and catalysis of potassium salts [192]. As is well known [193], the percentage variation between minimum and maximum activation energy should be less than 30%, when the one-step decomposition reaction could be used performing kinetic computations on thermal analysis data. Therefore, the conversion range of 0.10-0.74 is applied in next sections, where the apparent activation energies vary from 180 to 195 kJ/mol and 130 to 180 kJ/mol with a percentage of ~8.0% and ~20-30% for the raw CHR and the CHR with  $K_2CO_3$ . The average activation energy ( $E_0$ ) of Herb, Herb-5%K, Herb-7%K and Herb-9%K are: 185.90 kJ/mol, 160.61 kJ/mol, 145.21 kJ/mol and 143.86 kJ/mol, respectively.

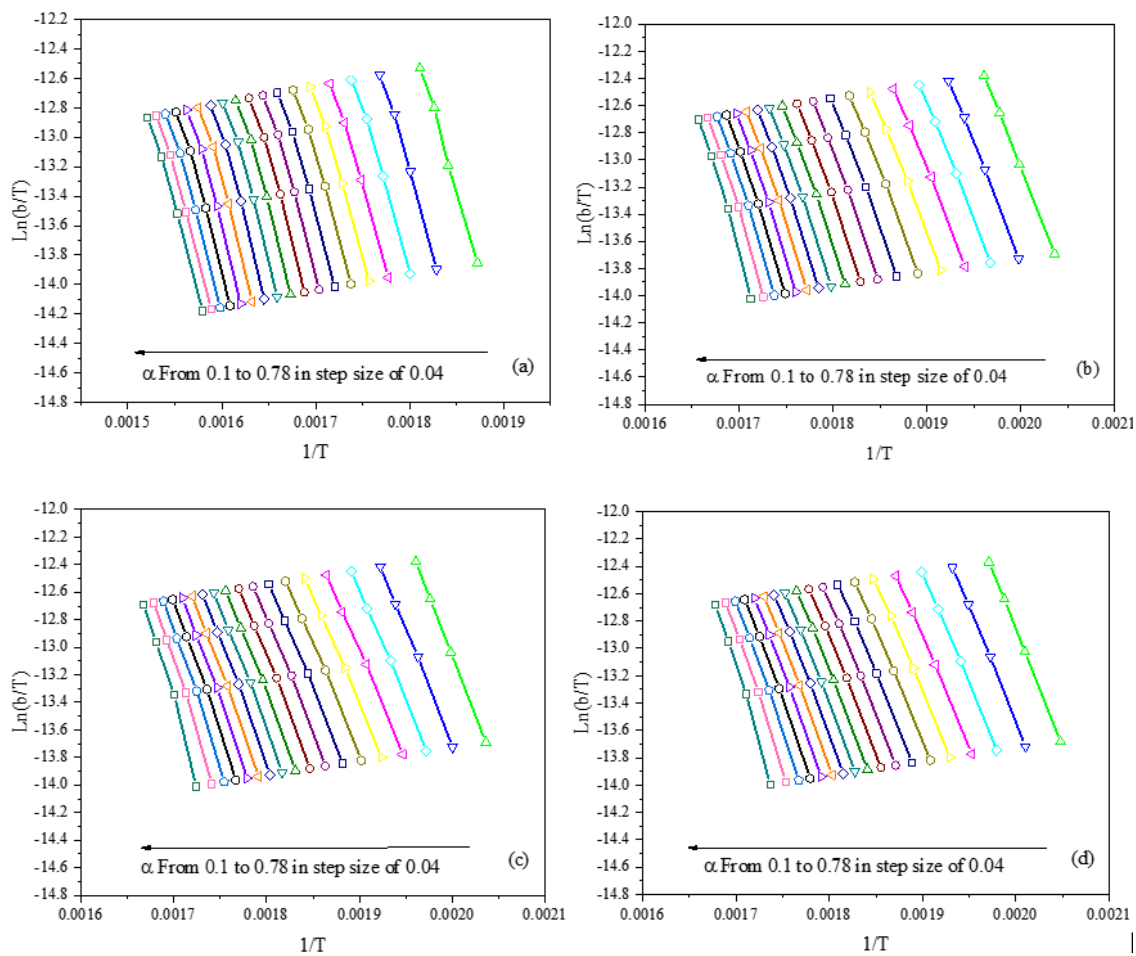


Figure 3-4: Kinetic plots of apparent activation energy as a function of conversion via Starink method. (a) Herb (b) Herb-5%K (c) Herb-7%K (d) Herb-9%K

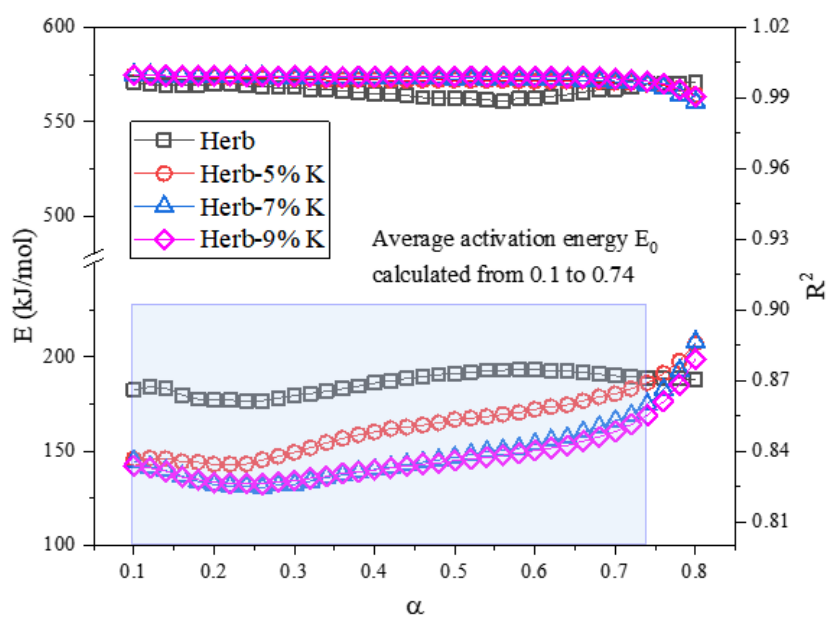


Figure 3-5: Variation of the thermal activation energy and the value of  $R^2$ .

Table 3-5: Calculation results of the thermal activation energy of herb samples by Starink method.

| $\alpha/$<br>% | Herb                       |        | Herb-5% K                  |        | Herb-7% K                  |        | Herb-9% K             |        |
|----------------|----------------------------|--------|----------------------------|--------|----------------------------|--------|-----------------------|--------|
|                | $E/kJ \cdot mol^{-1}$<br>1 | $R^2$  | $E/kJ \cdot mol^{-1}$<br>1 | $R^2$  | $E/kJ \cdot mol^{-1}$<br>1 | $R^2$  | $E/kJ \cdot mol^{-1}$ | $R^2$  |
| 0.1            | 182.27                     | 0.9924 | 145.75                     | 0.9998 | 144.69                     | 1.0000 | 142.24                | 0.9999 |
| 0.12           | 184.21                     | 0.9996 | 146.13                     | 0.9996 | 141.58                     | 0.9996 | 141.04                | 0.9996 |
| 0.14           | 183.19                     | 0.9982 | 145.92                     | 0.9994 | 139.58                     | 0.9993 | 139.27                | 0.9995 |
| 0.16           | 179.78                     | 0.9941 | 144.38                     | 0.9992 | 136.60                     | 0.9993 | 136.21                | 0.9994 |
| 0.18           | 177.61                     | 0.9968 | 144.00                     | 0.9990 | 133.80                     | 0.9991 | 134.83                | 0.9993 |
| 0.2            | 176.88                     | 0.9957 | 143.01                     | 0.9988 | 132.34                     | 0.9990 | 133.33                | 0.9994 |
| 0.22           | 176.98                     | 0.9952 | 143.08                     | 0.9988 | 131.35                     | 0.9992 | 132.93                | 0.9994 |
| 0.24           | 176.60                     | 0.9952 | 143.12                     | 0.9987 | 131.23                     | 0.9991 | 132.77                | 0.9992 |
| 0.26           | 176.75                     | 0.9957 | 145.29                     | 0.9985 | 130.69                     | 0.9990 | 132.46                | 0.9992 |
| 0.28           | 178.24                     | 0.9958 | 147.20                     | 0.9985 | 131.98                     | 0.9989 | 133.76                | 0.9992 |
| 0.3            | 179.38                     | 0.9962 | 149.27                     | 0.9981 | 132.35                     | 0.9987 | 134.26                | 0.9993 |
| 0.32           | 180.57                     | 0.9952 | 151.80                     | 0.9981 | 133.99                     | 0.9985 | 135.51                | 0.9991 |
| 0.34           | 181.70                     | 0.9947 | 154.46                     | 0.9976 | 136.10                     | 0.9986 | 136.44                | 0.9991 |
| 0.36           | 183.16                     | 0.9945 | 156.67                     | 0.9977 | 137.21                     | 0.9987 | 138.20                | 0.9990 |
| 0.38           | 184.55                     | 0.9945 | 158.73                     | 0.9979 | 138.90                     | 0.9984 | 139.07                | 0.9991 |
| 0.4            | 186.04                     | 0.9938 | 160.13                     | 0.9976 | 140.26                     | 0.9985 | 140.01                | 0.9990 |
| 0.42           | 187.25                     | 0.9937 | 161.91                     | 0.9975 | 141.25                     | 0.9983 | 141.00                | 0.9991 |
| 0.44           | 188.64                     | 0.9928 | 162.73                     | 0.9975 | 142.93                     | 0.9986 | 142.01                | 0.9992 |
| 0.46           | 189.60                     | 0.9925 | 163.82                     | 0.9975 | 143.99                     | 0.9985 | 143.09                | 0.9991 |
| 0.48           | 190.62                     | 0.9917 | 164.99                     | 0.9977 | 145.34                     | 0.9983 | 143.72                | 0.9992 |
| 0.5            | 191.24                     | 0.9917 | 166.69                     | 0.9975 | 146.63                     | 0.9982 | 145.02                | 0.9992 |
| 0.52           | 191.77                     | 0.9910 | 167.50                     | 0.9974 | 148.15                     | 0.9983 | 145.68                | 0.9992 |
| 0.54           | 192.81                     | 0.9902 | 168.29                     | 0.9974 | 149.75                     | 0.9980 | 146.70                | 0.9990 |
| 0.56           | 192.93                     | 0.9900 | 169.49                     | 0.9974 | 150.54                     | 0.9983 | 147.75                | 0.9990 |
| 0.58           | 193.27                     | 0.9899 | 170.38                     | 0.9972 | 151.52                     | 0.9982 | 148.90                | 0.9991 |
| 0.6            | 193.15                     | 0.9897 | 172.16                     | 0.9971 | 153.73                     | 0.9982 | 150.40                | 0.9990 |
| 0.62           | 192.66                     | 0.9892 | 173.49                     | 0.9971 | 155.69                     | 0.9981 | 151.59                | 0.9989 |
| 0.64           | 192.46                     | 0.9884 | 174.58                     | 0.9971 | 156.98                     | 0.9977 | 152.95                | 0.9988 |
| 0.66           | 191.80                     | 0.9900 | 176.63                     | 0.9973 | 160.10                     | 0.9976 | 155.27                | 0.9989 |
| 0.68           | 190.80                     | 0.9900 | 178.77                     | 0.9969 | 162.74                     | 0.9975 | 157.56                | 0.9987 |
| 0.7            | 189.92                     | 0.9907 | 180.43                     | 0.9966 | 166.14                     | 0.9970 | 160.41                | 0.9983 |
| 0.72           | 189.26                     | 0.9915 | 183.15                     | 0.9965 | 169.07                     | 0.9965 | 164.13                | 0.9977 |
| 0.74           | 188.76                     | 0.9926 | 186.23                     | 0.9959 | 174.81                     | 0.9958 | 169.01                | 0.9970 |
| 0.76           | 188.97                     | 0.9935 | 191.18                     | 0.9953 | 182.58                     | 0.9945 | 176.31                | 0.9961 |
| 0.78           | 188.65                     | 0.9937 | 197.73                     | 0.9941 | 192.62                     | 0.9911 | 185.22                | 0.9937 |

|     |        |        |        |        |        |        |        |        |
|-----|--------|--------|--------|--------|--------|--------|--------|--------|
| 0.8 | 188.11 | 0.9948 | 206.97 | 0.9915 | 207.82 | 0.9884 | 198.89 | 0.9906 |
|-----|--------|--------|--------|--------|--------|--------|--------|--------|

### 3.4.3 Reaction model and pre-exponential factor

The  $E_0$  obtained by Starink method is used to determine the reaction model and pre-exponential factor, since the method is found to be more efficient [185]. By plotting the theoretical (lines) and experimental (spots) master plots as a function of conversion rate in Figure 3-6, it is observed that experimental master plots give poor fits to theoretical master plots based on the common reaction mechanisms ( $G(\alpha)$ , Table 3-3), even though experimental master plots at all heating rates are little close to the three-dimensional diffusion-Jander (D3) model when  $\alpha < 0.5$ . As is noted by [193], D3-Jander equation (Eq. (3-13)) used the parabolic law (Eq. (3-10)) to define the thickness of the reaction zone ( $x$ , Eq. (3-12)) based on the assumption of spherical solid particles.

$$x^2 = kt \quad (3-10)$$

$$x = R (1 - (1 - \alpha)^{1/3}) \quad (3-11)$$

$$2 \left(1 - (1 - \alpha)^{1/3}\right) = k't \quad (3-12)$$

Where  $k$  and  $k'$  are constant.

However, the parabolic law is the simplest rate equation for an infinite flat plane (one-dimensional (D1) model), where the conversion fraction ( $\alpha$ ) is directly proportional to product layer thickness ( $x$ ). At present work, therefore, a modified D3-Jander model ( $D_n$ ) is defined as Eq. (14), to describe the complex nonlinear relationship between  $\alpha$  and  $x$ .

$$G(\alpha) = \left[1 - (1 - \alpha)^{1/3}\right]^n \quad (3-13)$$

Where  $n$  is the coefficient of the model. Substituting the Eq. (7) to Eq. (6), then, taking logarithm on both side of the equation, the following equation is given as:

$$\ln[P(u)] - \ln\left[\frac{\beta R}{E\alpha}\right] = -\ln A + n \ln [1 - (1 - \alpha)^{1/3}] \quad (3-14)$$

The coefficient  $n$  of the D3 model and the pre-exponential factor  $A$  for different heating rates can be solved from Eq. (3-14) by plotting the linear fitting model of  $\ln[P(u)] - \ln\left[\frac{\beta R}{E\alpha}\right]$  against  $\ln [1 - (1 - \alpha)^{1/3}]$ , whose slope and intercept allow evaluation of the kinetic parameters  $n$  and  $A$ , respectively.

In Figure 3-6, The coefficients  $n$  of  $D_n$  model are depicted using the average values at different

heating rates. The detailed results of the pre-exponential factor  $A$  and coefficient  $n$  are shown in Table 3-6.

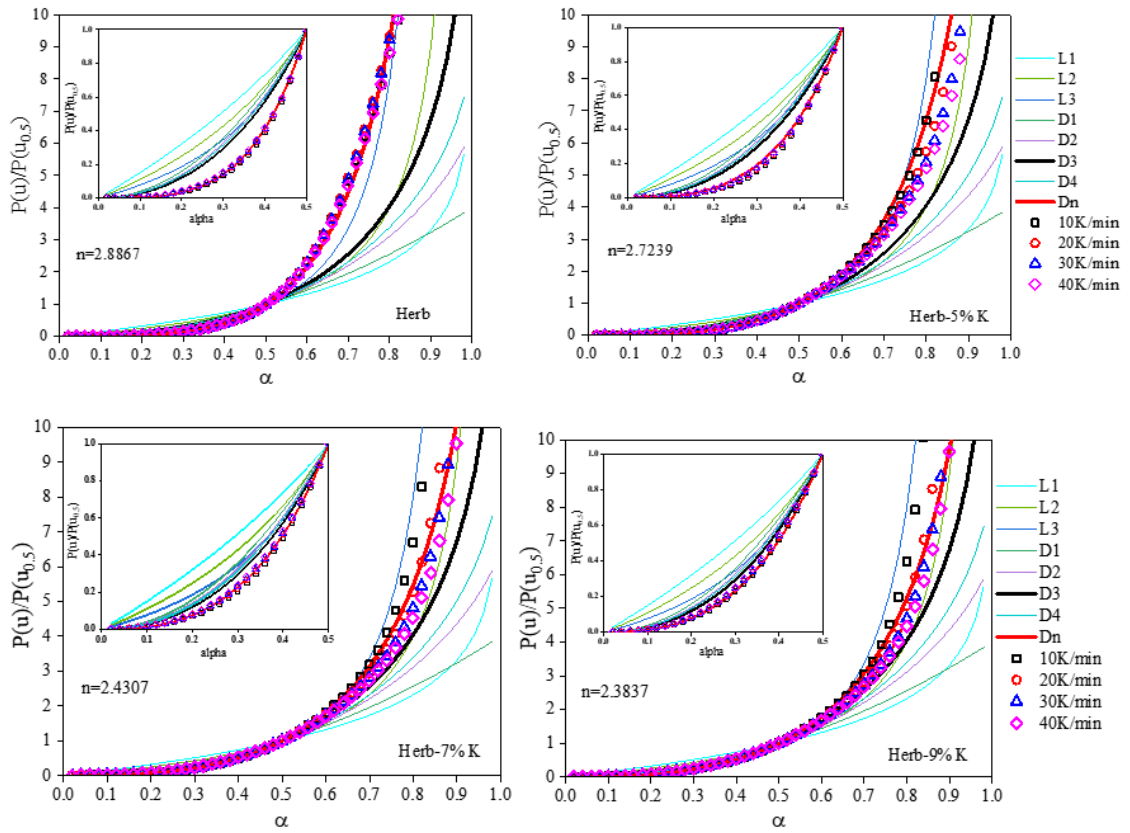


Figure 3-6: Experimental and theoretical master-plots of the CHR samples with different  $K_2CO_3$ .

Table 3-6: The calculation results of herb samples ( $D_n$  coefficient and pre-exponential factor).

| $\beta$ | Herb   |                       | Herb-5% K |                       | Herb-7% K |                       | Herb-9% K |                       |
|---------|--------|-----------------------|-----------|-----------------------|-----------|-----------------------|-----------|-----------------------|
|         | $n$    | $A/(s^{-1})$          | $n$       | $A/(s^{-1})$          | $n$       | $A/(s^{-1})$          | $n$       | $A/(s^{-1})$          |
| 10K/min | 2.9244 | $1.66 \times 10^{12}$ | 2.8092    | $1.66 \times 10^{11}$ | 2.5518    | $1.03 \times 10^{10}$ | 2.4714    | $1.06 \times 10^{10}$ |
| 20K/min | 2.8766 | $1.94 \times 10^{12}$ | 2.7136    | $2.09 \times 10^{11}$ | 2.4128    | $1.45 \times 10^{10}$ | 2.3893    | $1.28 \times 10^{10}$ |
| 30K/min | 2.8742 | $1.96 \times 10^{12}$ | 2.6936    | $2.13 \times 10^{11}$ | 2.3883    | $1.46 \times 10^{10}$ | 2.3596    | $1.35 \times 10^{10}$ |
| 40K/min | 2.8717 | $1.79 \times 10^{12}$ | 2.6792    | $2.12 \times 10^{11}$ | 2.3700    | $1.50 \times 10^{10}$ | 2.3146    | $1.45 \times 10^{10}$ |
| AVE     | 2.8867 | $1.84 \times 10^{12}$ | 2.7239    | $2.00 \times 10^{11}$ | 2.4307    | $1.36 \times 10^{10}$ | 2.3837    | $1.28 \times 10^{10}$ |



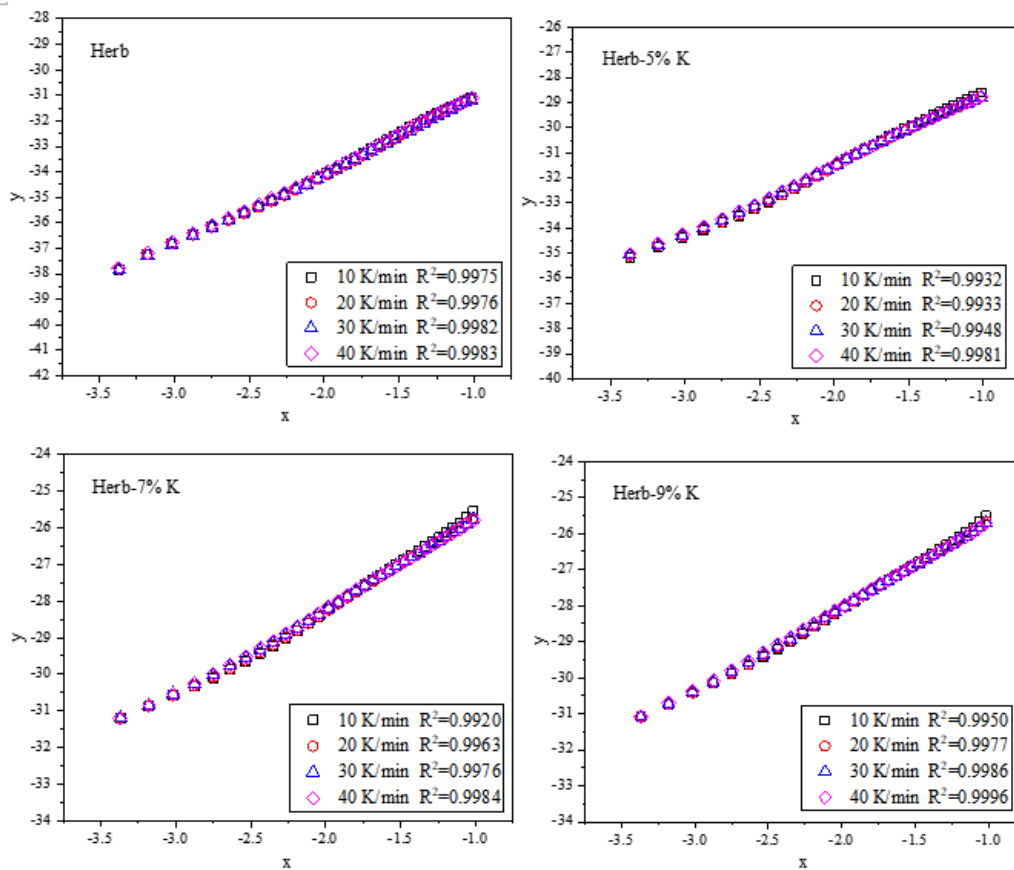


Figure 3-7: Linear fitting model of  $y = \ln[P(u)] - \ln \left[ \frac{\beta R}{E\alpha} \right]$  against  $x = \ln [1 - (1 - \alpha)^{1/3}]$ .

The experimental and  $D_n$  theoretical master plots of the raw CHR at different heating rates are almost overlap, while that of the CHR samples with  $K_2CO_3$  have apparent differences after  $\alpha > 0.6$  under different heating rates. The mechanism corresponds to  $D_n$ -Jander equation, indicating that reaction rate is mainly governed by diffusion for the main devolatilization stage of the raw CHR at all four heating rates. Therefore, the average values of  $n$  and  $A$  at the four heating rates can be used as the kinetic parameters for the raw CHR sample. However, for CHR samples with  $K_2CO_3$ , the experimental points become to discrete data at different heating rates as the temperature increase ( $\alpha > 0.5$ ), and values of  $n$  and  $A$  tend to change measurably with the heating rates as shown in Figure 3-7 (calculation data listed in Table 3-7, Table 3-8, Table 3-9 and Table 3-10). It possibly attributes to the significant catalytic effect of  $K_2CO_3$  on the thermal decomposition of CHR samples at the higher temperatures. Consequently, for CHR with  $K_2CO_3$ , different values of  $n$  and  $A$  are selected at various heating rates, which is useful to improve the accuracy of kinetic parameters, as well as for the modeling of biomass catalytic pyrolysis.

Table 3-7: Calculation data of fitting model for original herb sample.

| 10 K/min | 20 K/min | 30 K/min | 40 K/min |
|----------|----------|----------|----------|
|----------|----------|----------|----------|

|        |         |        |         |        |         |        |         |
|--------|---------|--------|---------|--------|---------|--------|---------|
| x      | y       | x      | y       | x      | y       | x      | y       |
| -3.369 | -37.832 | -3.369 | -37.792 | -3.369 | -37.850 | -3.369 | -37.775 |
| -3.179 | -37.238 | -3.178 | -37.255 | -3.177 | -37.286 | -3.177 | -37.196 |
| -3.017 | -36.801 | -3.016 | -36.833 | -3.016 | -36.845 | -3.016 | -36.755 |
| -2.876 | -36.468 | -2.876 | -36.493 | -2.876 | -36.492 | -2.875 | -36.397 |
| -2.750 | -36.168 | -2.750 | -36.185 | -2.749 | -36.176 | -2.750 | -36.082 |
| -2.638 | -35.893 | -2.636 | -35.905 | -2.638 | -35.896 | -2.638 | -35.801 |
| -2.535 | -35.627 | -2.532 | -35.638 | -2.533 | -35.626 | -2.535 | -35.537 |
| -2.438 | -35.377 | -2.438 | -35.394 | -2.439 | -35.382 | -2.437 | -35.283 |
| -2.349 | -35.139 | -2.351 | -35.165 | -2.349 | -35.146 | -2.349 | -35.047 |
| -2.267 | -34.900 | -2.267 | -34.932 | -2.267 | -34.918 | -2.267 | -34.820 |
| -2.189 | -34.675 | -2.190 | -34.715 | -2.189 | -34.698 | -2.190 | -34.606 |
| -2.116 | -34.459 | -2.116 | -34.507 | -2.117 | -34.493 | -2.116 | -34.398 |
| -2.047 | -34.249 | -2.046 | -34.301 | -2.046 | -34.291 | -2.046 | -34.197 |
| -1.979 | -34.041 | -1.979 | -34.104 | -1.979 | -34.095 | -1.979 | -34.000 |
| -1.916 | -33.845 | -1.916 | -33.914 | -1.917 | -33.907 | -1.916 | -33.813 |
| -1.855 | -33.649 | -1.855 | -33.728 | -1.856 | -33.725 | -1.855 | -33.628 |
| -1.797 | -33.461 | -1.797 | -33.546 | -1.796 | -33.542 | -1.797 | -33.450 |
| -1.739 | -33.275 | -1.740 | -33.368 | -1.739 | -33.366 | -1.740 | -33.273 |
| -1.685 | -33.097 | -1.684 | -33.191 | -1.686 | -33.200 | -1.684 | -33.100 |
| -1.631 | -32.921 | -1.631 | -33.022 | -1.631 | -33.029 | -1.631 | -32.932 |
| -1.580 | -32.753 | -1.579 | -32.854 | -1.580 | -32.865 | -1.580 | -32.767 |
| -1.529 | -32.586 | -1.528 | -32.691 | -1.528 | -32.702 | -1.528 | -32.604 |
| -1.479 | -32.419 | -1.479 | -32.530 | -1.479 | -32.541 | -1.479 | -32.444 |
| -1.430 | -32.261 | -1.431 | -32.373 | -1.431 | -32.389 | -1.430 | -32.286 |
| -1.382 | -32.109 | -1.382 | -32.214 | -1.382 | -32.232 | -1.383 | -32.137 |
| -1.335 | -31.961 | -1.335 | -32.063 | -1.336 | -32.084 | -1.335 | -31.986 |
| -1.290 | -31.824 | -1.290 | -31.923 | -1.290 | -31.939 | -1.289 | -31.847 |
| -1.243 | -31.686 | -1.243 | -31.779 | -1.243 | -31.797 | -1.243 | -31.707 |
| -1.198 | -31.561 | -1.198 | -31.646 | -1.198 | -31.664 | -1.199 | -31.578 |
| -1.154 | -31.443 | -1.152 | -31.516 | -1.154 | -31.537 | -1.153 | -31.452 |
| -1.107 | -31.325 | -1.109 | -31.400 | -1.108 | -31.410 | -1.107 | -31.330 |
| -1.064 | -31.215 | -1.062 | -31.277 | -1.063 | -31.292 | -1.062 | -31.215 |

Table 3-8: Calculation data of fitting model for herb-5% K sample.

| 10 K/min |         | 20 K/min |         | 30 K/min |         | 40 K/min |         |
|----------|---------|----------|---------|----------|---------|----------|---------|
| x        | y       | x        | y       | x        | y       | x        | y       |
| -3.367   | -35.160 | -3.370   | -35.093 | -3.369   | -35.070 | -3.367   | -35.021 |

|        |         |        |         |        |         |        |         |
|--------|---------|--------|---------|--------|---------|--------|---------|
| -3.178 | -34.747 | -3.180 | -34.701 | -3.179 | -34.661 | -3.179 | -34.614 |
| -3.017 | -34.385 | -3.016 | -34.346 | -3.017 | -34.302 | -3.018 | -34.249 |
| -2.877 | -34.079 | -2.875 | -34.038 | -2.875 | -33.985 | -2.875 | -33.930 |
| -2.749 | -33.786 | -2.750 | -33.747 | -2.749 | -33.691 | -2.750 | -33.632 |
| -2.636 | -33.512 | -2.637 | -33.474 | -2.636 | -33.410 | -2.636 | -33.349 |
| -2.533 | -33.238 | -2.534 | -33.201 | -2.532 | -33.136 | -2.533 | -33.076 |
| -2.439 | -32.974 | -2.439 | -32.939 | -2.437 | -32.874 | -2.437 | -32.813 |
| -2.349 | -32.696 | -2.349 | -32.673 | -2.350 | -32.617 | -2.349 | -32.555 |
| -2.267 | -32.434 | -2.266 | -32.421 | -2.267 | -32.369 | -2.267 | -32.313 |
| -2.189 | -32.179 | -2.189 | -32.180 | -2.190 | -32.133 | -2.189 | -32.077 |
| -2.116 | -31.930 | -2.116 | -31.944 | -2.116 | -31.899 | -2.116 | -31.853 |
| -2.045 | -31.684 | -2.046 | -31.716 | -2.046 | -31.677 | -2.045 | -31.631 |
| -1.979 | -31.460 | -1.980 | -31.500 | -1.980 | -31.465 | -1.981 | -31.426 |
| -1.916 | -31.246 | -1.915 | -31.292 | -1.916 | -31.265 | -1.918 | -31.230 |
| -1.855 | -31.046 | -1.855 | -31.097 | -1.855 | -31.077 | -1.855 | -31.039 |
| -1.796 | -30.851 | -1.796 | -30.912 | -1.796 | -30.892 | -1.796 | -30.861 |
| -1.739 | -30.677 | -1.739 | -30.742 | -1.739 | -30.724 | -1.739 | -30.693 |
| -1.684 | -30.509 | -1.684 | -30.578 | -1.684 | -30.562 | -1.684 | -30.533 |
| -1.631 | -30.349 | -1.631 | -30.420 | -1.630 | -30.407 | -1.631 | -30.383 |
| -1.578 | -30.188 | -1.578 | -30.266 | -1.579 | -30.260 | -1.580 | -30.234 |
| -1.528 | -30.044 | -1.528 | -30.125 | -1.529 | -30.121 | -1.529 | -30.096 |
| -1.479 | -29.905 | -1.478 | -29.989 | -1.479 | -29.987 | -1.478 | -29.963 |
| -1.430 | -29.769 | -1.430 | -29.857 | -1.430 | -29.858 | -1.430 | -29.836 |
| -1.383 | -29.638 | -1.382 | -29.731 | -1.382 | -29.734 | -1.382 | -29.711 |
| -1.335 | -29.504 | -1.336 | -29.604 | -1.335 | -29.609 | -1.336 | -29.590 |
| -1.289 | -29.377 | -1.289 | -29.482 | -1.290 | -29.490 | -1.289 | -29.473 |
| -1.243 | -29.254 | -1.243 | -29.362 | -1.243 | -29.373 | -1.243 | -29.358 |
| -1.198 | -29.127 | -1.197 | -29.241 | -1.197 | -29.255 | -1.199 | -29.245 |
| -1.152 | -28.998 | -1.152 | -29.121 | -1.153 | -29.140 | -1.153 | -29.129 |
| -1.107 | -28.874 | -1.107 | -29.004 | -1.107 | -29.025 | -1.108 | -29.017 |
| -1.062 | -28.741 | -1.063 | -28.883 | -1.062 | -28.905 | -1.063 | -28.903 |

Table 3-9: Calculation data of fitting model for herb-7% K sample.

| 10 K/min |         | 20 K/min |         | 30 K/min |         | 40 K/min |         |
|----------|---------|----------|---------|----------|---------|----------|---------|
| x        | y       | x        | y       | x        | y       | x        | y       |
| -3.368   | -31.202 | -3.368   | -31.201 | -3.369   | -31.194 | -3.368   | -31.200 |
| -3.179   | -30.872 | -3.179   | -30.879 | -3.179   | -30.847 | -3.178   | -30.842 |

|        |         |        |         |        |         |        |         |
|--------|---------|--------|---------|--------|---------|--------|---------|
| -3.018 | -30.577 | -3.018 | -30.584 | -3.018 | -30.539 | -3.018 | -30.530 |
| -2.874 | -30.327 | -2.875 | -30.321 | -2.874 | -30.268 | -2.876 | -30.249 |
| -2.750 | -30.100 | -2.750 | -30.083 | -2.749 | -30.017 | -2.749 | -29.994 |
| -2.637 | -29.868 | -2.637 | -29.847 | -2.636 | -29.773 | -2.636 | -29.747 |
| -2.534 | -29.650 | -2.532 | -29.619 | -2.533 | -29.547 | -2.533 | -29.518 |
| -2.437 | -29.429 | -2.438 | -29.400 | -2.440 | -29.330 | -2.438 | -29.294 |
| -2.351 | -29.228 | -2.350 | -29.199 | -2.350 | -29.125 | -2.349 | -29.087 |
| -2.267 | -29.010 | -2.267 | -28.991 | -2.267 | -28.921 | -2.267 | -28.883 |
| -2.191 | -28.818 | -2.190 | -28.803 | -2.190 | -28.733 | -2.189 | -28.695 |
| -2.115 | -28.612 | -2.116 | -28.609 | -2.115 | -28.540 | -2.115 | -28.508 |
| -2.046 | -28.415 | -2.046 | -28.420 | -2.047 | -28.361 | -2.048 | -28.331 |
| -1.980 | -28.235 | -1.979 | -28.245 | -1.979 | -28.188 | -1.981 | -28.163 |
| -1.916 | -28.054 | -1.916 | -28.075 | -1.917 | -28.024 | -1.916 | -27.997 |
| -1.855 | -27.886 | -1.855 | -27.911 | -1.857 | -27.867 | -1.855 | -27.842 |
| -1.797 | -27.727 | -1.798 | -27.761 | -1.796 | -27.714 | -1.796 | -27.695 |
| -1.740 | -27.569 | -1.739 | -27.606 | -1.740 | -27.566 | -1.740 | -27.552 |
| -1.685 | -27.421 | -1.684 | -27.464 | -1.685 | -27.426 | -1.684 | -27.414 |
| -1.632 | -27.277 | -1.632 | -27.329 | -1.632 | -27.292 | -1.631 | -27.283 |
| -1.579 | -27.139 | -1.580 | -27.197 | -1.579 | -27.161 | -1.579 | -27.157 |
| -1.528 | -27.004 | -1.529 | -27.067 | -1.530 | -27.039 | -1.529 | -27.034 |
| -1.478 | -26.870 | -1.480 | -26.944 | -1.481 | -26.916 | -1.480 | -26.915 |
| -1.431 | -26.751 | -1.430 | -26.824 | -1.431 | -26.800 | -1.430 | -26.802 |
| -1.384 | -26.632 | -1.383 | -26.710 | -1.382 | -26.687 | -1.382 | -26.692 |
| -1.336 | -26.501 | -1.335 | -26.588 | -1.336 | -26.571 | -1.336 | -26.579 |
| -1.289 | -26.377 | -1.289 | -26.473 | -1.290 | -26.458 | -1.291 | -26.472 |
| -1.243 | -26.258 | -1.243 | -26.363 | -1.243 | -26.350 | -1.243 | -26.362 |
| -1.198 | -26.125 | -1.198 | -26.242 | -1.199 | -26.236 | -1.200 | -26.252 |
| -1.153 | -25.995 | -1.152 | -26.123 | -1.154 | -26.121 | -1.155 | -26.143 |
| -1.107 | -25.854 | -1.108 | -25.998 | -1.108 | -26.003 | -1.109 | -26.026 |
| -1.063 | -25.717 | -1.062 | -25.874 | -1.062 | -25.882 | -1.062 | -25.910 |

Table 3-10: Calculation data of fitting model for herb-9% K sample.

| 10 K/min |          | 20 K/min |          | 30 K/min |          | 40 K/min |          |
|----------|----------|----------|----------|----------|----------|----------|----------|
| <i>x</i> | <i>y</i> | <i>x</i> | <i>y</i> | <i>x</i> | <i>y</i> | <i>x</i> | <i>y</i> |
| -3.366   | -31.090  | -3.368   | -31.082  | -3.370   | -31.085  | -3.368   | -31.067  |

|        |         |        |         |        |         |        |         |
|--------|---------|--------|---------|--------|---------|--------|---------|
| -3.180 | -30.739 | -3.179 | -30.742 | -3.180 | -30.731 | -3.179 | -30.706 |
| -3.015 | -30.422 | -3.016 | -30.425 | -3.016 | -30.401 | -3.018 | -30.375 |
| -2.877 | -30.157 | -2.876 | -30.147 | -2.875 | -30.114 | -2.874 | -30.079 |
| -2.749 | -29.893 | -2.749 | -29.873 | -2.750 | -29.841 | -2.749 | -29.798 |
| -2.636 | -29.655 | -2.637 | -29.625 | -2.637 | -29.589 | -2.637 | -29.545 |
| -2.534 | -29.416 | -2.532 | -29.386 | -2.534 | -29.353 | -2.534 | -29.304 |
| -2.437 | -29.194 | -2.438 | -29.165 | -2.439 | -29.131 | -2.437 | -29.077 |
| -2.350 | -28.991 | -2.350 | -28.962 | -2.349 | -28.926 | -2.349 | -28.871 |
| -2.266 | -28.777 | -2.267 | -28.755 | -2.266 | -28.723 | -2.267 | -28.673 |
| -2.191 | -28.591 | -2.190 | -28.567 | -2.189 | -28.535 | -2.190 | -28.489 |
| -2.116 | -28.396 | -2.115 | -28.381 | -2.116 | -28.355 | -2.115 | -28.306 |
| -2.048 | -28.220 | -2.046 | -28.211 | -2.046 | -28.186 | -2.046 | -28.140 |
| -1.980 | -28.039 | -1.979 | -28.037 | -1.981 | -28.021 | -1.981 | -27.976 |
| -1.915 | -27.875 | -1.916 | -27.882 | -1.917 | -27.863 | -1.916 | -27.825 |
| -1.855 | -27.722 | -1.854 | -27.730 | -1.856 | -27.716 | -1.854 | -27.677 |
| -1.795 | -27.570 | -1.796 | -27.587 | -1.796 | -27.572 | -1.796 | -27.539 |
| -1.740 | -27.432 | -1.739 | -27.449 | -1.739 | -27.439 | -1.741 | -27.408 |
| -1.684 | -27.290 | -1.684 | -27.315 | -1.686 | -27.308 | -1.685 | -27.279 |
| -1.632 | -27.166 | -1.630 | -27.189 | -1.631 | -27.184 | -1.631 | -27.156 |
| -1.579 | -27.034 | -1.579 | -27.066 | -1.579 | -27.060 | -1.580 | -27.038 |
| -1.530 | -26.916 | -1.529 | -26.950 | -1.528 | -26.944 | -1.529 | -26.925 |
| -1.479 | -26.790 | -1.479 | -26.833 | -1.478 | -26.831 | -1.478 | -26.810 |
| -1.430 | -26.671 | -1.430 | -26.722 | -1.430 | -26.719 | -1.430 | -26.703 |
| -1.383 | -26.556 | -1.382 | -26.608 | -1.382 | -26.610 | -1.382 | -26.596 |
| -1.336 | -26.439 | -1.336 | -26.497 | -1.336 | -26.502 | -1.336 | -26.490 |
| -1.288 | -26.321 | -1.289 | -26.388 | -1.289 | -26.397 | -1.289 | -26.385 |
| -1.244 | -26.207 | -1.243 | -26.281 | -1.243 | -26.288 | -1.243 | -26.281 |
| -1.198 | -26.084 | -1.197 | -26.164 | -1.197 | -26.177 | -1.199 | -26.176 |
| -1.152 | -25.957 | -1.153 | -26.051 | -1.152 | -26.067 | -1.154 | -26.069 |
| -1.108 | -25.824 | -1.107 | -25.931 | -1.107 | -25.954 | -1.108 | -25.955 |
| -1.062 | -25.679 | -1.062 | -25.805 | -1.063 | -25.834 | -1.062 | -25.836 |

### 3.5 Validation and conclusion

CHR solid waste is a special kind of lignocellulosic biomass, which mainly consists of hemicellulose, cellulose and lignin as well. It had been reported that the activation energies of

hemicellulose, cellulose and lignin were roughly in the range of 167-190 kJ/mol, 197-218 kJ/mol and 231-276 kJ/mol, respectively [194]. Thus, the average activation energies ( $E_0$ ) obtained in this paper are in the reasonable ranges, though the  $E_0$  of CHR loading catalysts is much lower than that of the raw CHR due to the catalysis of  $K_2CO_3$ . The values of  $E_0$  (Table-S2),  $A$  and  $n$  with  $D_n$ -Jader model (Table-S4) were employed to elaborate the kinetic parameters of the CHR pyrolysis in the main devolatilization stage.

With respect to TG curves (Figure 3-8), good fitting qualities are observed with  $R^2 > 0.995$  for the raw CHR at all the four heating rates. For the CHR samples with  $K_2CO_3$ , however,  $R^2$  values at lower heating rates ( $\beta \leq 20K$ ) are a little bit below 0.995, especially in the high temperatures ( $> 575K$ ). This is still a good agreement; the small deviation might be caused by the combined effects of secondary reactions due to the  $K_2CO_3$  catalysis of biomass char and lignin under high temperatures, which indicates that the catalytic pyrolysis reactions should require complex multi-step kinetic pathways and could not be perfectly described by the simple parameters of single-step kinetics.

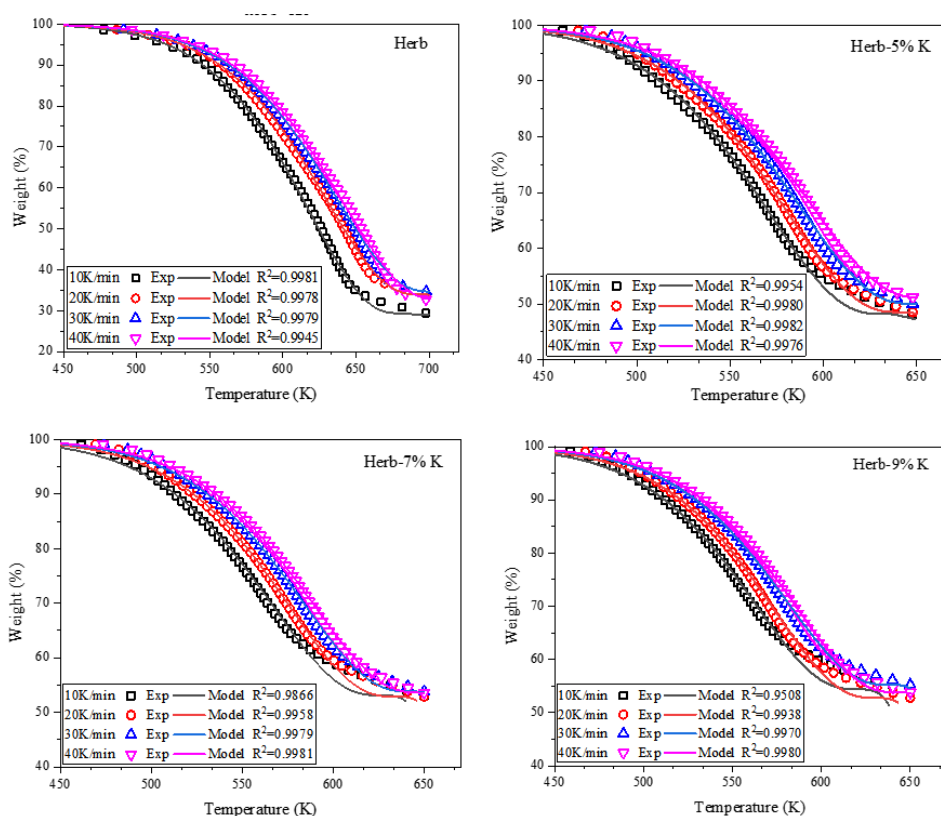


Figure 3-8: Calculated TG curves based on the  $D_n$ -Jader model compared with experimental data at various heating rates.

The catalytic pyrolysis of CHR solid waste loading  $K_2CO_3$  was studied by the non-isothermal temperature-programmed thermogravimetry. The pyrolysis temperature of the raw CHR is

higher than traditional lignocellulosic biomass without decoction.  $K_2CO_3$  catalysts significantly promote the catalytic pyrolysis reaction of the hemicellulose and cellulose of CHR samples at the main devolatilization stage from 425K to 700K, which is the major pyrolysis region as over 80.0% mass loss occurs. The pyrolysis kinetics were found to be successfully described by using the model-free Starink method. The estimated average activation energy ( $E_0$ ) of Herb, Herb-5%K, Herb-7%K and Herb-9%K are: 185.9kJ/mol, 160.6kJ/mol, 145.2kJ/mol and 143.8 kJ/mol, respectively. By using the generalized master-plots method, it was found that the CHR pyrolysis was governed by a modified  $D_n$ -Jader model  $G(\alpha) = \left[1 - (1 - \alpha)^{\frac{1}{3}}\right]^n$ , but values of  $n$  and  $A$  tend to change measurably with heating rates for the CHR samples with catalysts due to the remarkably catalytic effect of  $K_2CO_3$ . The model results using the optimized parameters were highly consistent with experimental TG data at all the four heating rates for the raw CHR, however, there is small discrepancy for that of the CHR samples with  $K_2CO_3$ , caused by the presence of multi-step complex decomposition reactions at high temperatures. Besides, cross-validation showed that the kinetic parameters can be applied not only to heating rates where they were obtained, but also to the other heating rate; which indicates that the current work provides a simple route for the kinetic analysis of catalytic pyrolysis of CHR solid waste, especially in the real scenarios with various and mutative heating rates.

## **Chapter 4. Evolution mechanism of N-containing species of product char during pyrolysis of biomass**

### **4.1 Introduction**

Biomass contains a certain amount of fuel nitrogen (N) due to its ability of nitrogen fixation during the growing process. In general, the order of N content in various types of biomass fuels is as follows: woody biomass (including forestry waste) < herbaceous biomass (including agricultural waste) < aquatic plants < industrial or domestic biomass waste [195, 196]. In the process of biomass thermochemical conversion, fuel N will form N-containing pollutants, such as gas-phase N ( $\text{NH}_3$ ,  $\text{HNCO}$ ,  $\text{HCN}$  and  $\text{NO}_x$ ). These pollutants have become the key factors affecting and restricting the clean utilization of biomass fuel [112]. This section will investigate the formation and evolution mechanisms of N-containing groups of char product of biomass pyrolysis. The pyrolysis process was carried out in rotating tubular resistance reactor, using the TGA and X-ray Photoelectron Spectroscopy (XPS) characterization methods to investigate the regulation mechanism of N-containing species during pyrolysis. There are many influencing factors in the process of biomass pyrolysis. In this experiment, three factors, biomass type, catalyst and pyrolysis temperature, were selected as experimental variables.

### **4.2 Research method**

#### **4.2.1 Materials**

This experiment selects typical woody biomass: Chinese herb residues (CHR) and bamboo shoot shell (BS). For each group of pyrolysis samples, 0.8-1.2g of CHR, BS, and BS loaded with  $\text{K}_2\text{CO}_3$  (15wt%) were taken for the comparison (marked as BS-15pc). The temperature of pyrolysis experiment is 25°C, 300°C, 500°C, 700°C and 900°C, and the heating up rate is 10°C/min.

#### **4.2.2 Experimental setup**

The rotating tubular resistance reactor is used as pyrolysis device, including the electric furnace body and the electric furnace temperature controller (Figure 4-1). There are conductors with high resistance in the furnace. When the power is turned on, the electric heating element in the furnace begins to generate heat and transfer the heat to the material. The connecting pipe was insulated with an electric heating belt to prevent tar condensing on the pipe wall. The pyrolysis carrier gas is supplied from a high-pressure cylinder, and the flow is controlled by a volumetric flowmeter. The pyrolysis atmosphere is high concentration nitrogen with a purity of 99.999%.



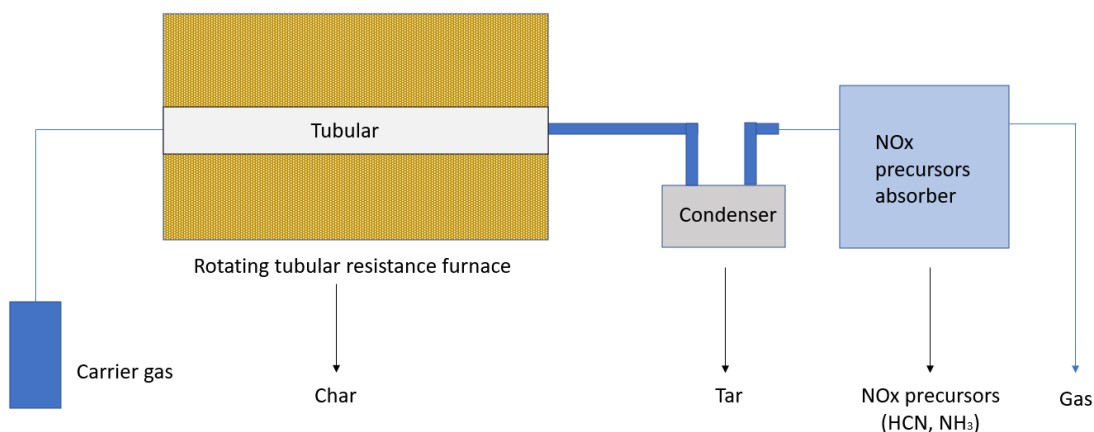


Figure 4-1: Schematic diagram of the experimental system.

#### 4.2.3 X-ray Photoelectron Spectroscopy (XPS) analysis method

The thermogravimetric analysis method has been discussed in Section 3. The N transformation mechanism of pyrolysis and the evolution characteristics of N-containing species were explored by XPS analyser [197]. The absolute yield of N-containing groups was determined from the N in the char product [118]. The char product of biomass pyrolysis was used for analysing. The XPS analyser is mainly composed of X-ray emission source, lens and analyser, detector, X-ray beam spot definition, neutralization electron source, sample operation table, and vacuum control system. At the beginning of the test, X-rays were irradiated on the surface of the biomass char product to obtain the information spectrum of electrons with a certain kinetic energy.

The relative content of N-containing groups could be obtained by the peak area of different types of N-containing groups. The N-containing groups are protein-N ( $399.7 \pm 0.4\text{eV}$ ), pyrrolic-N ( $400.2 \pm 0.3\text{eV}$ ), oxidized-N ( $402\text{-}405\text{eV}$ ), quaternary-N ( $401.2 \pm 0.3\text{eV}$ ) and pyridinic-N ( $398.5 \pm 0.3\text{eV}$ ). The obtained XPS spectrum was internally corrected by *Avantage* software for each peak. The Gaussian-Lorentzian mixture function was used for peak fitting, in which the width at half maximum of N functionalities is  $1.65\text{eV}$ . The relative content of different N-containing groups could be given by:

$$F_{N^*} = \frac{A_{N^*}}{\sum A_{N^*}}$$

Where  $F_N$  is the relative content of different N-containing species,  $A_N$  is the area of each peak.

## 4.3 Results and discussion

The XPS spectra could characterize the structure evolution of the surface of biochar product. It is considered that the distribution of the N species groups on the surface of solid char is same as that in the char body, since the uniform distribution of N [118]. The groups of N species have been introduced in Section 4.2.3. The evolution properties of N-containing groups in solid char product of CHR and BS at different temperature were explored (as shown in Figure 4-2, Figure 4-3 and Figure 4-4). By solving the peak area of each N-containing groups in the XPS (N 1s) spectrum of the solid product of biomass pyrolysis, the change in the relative content of each N-containing species can be calculated (Table 4-1, Table 4-2 and Table 4-3). Figure 4-5, Figure 4-6 and Figure 4-7 show the relative content of N species for samples: CHR, BS, and BS-15pc.

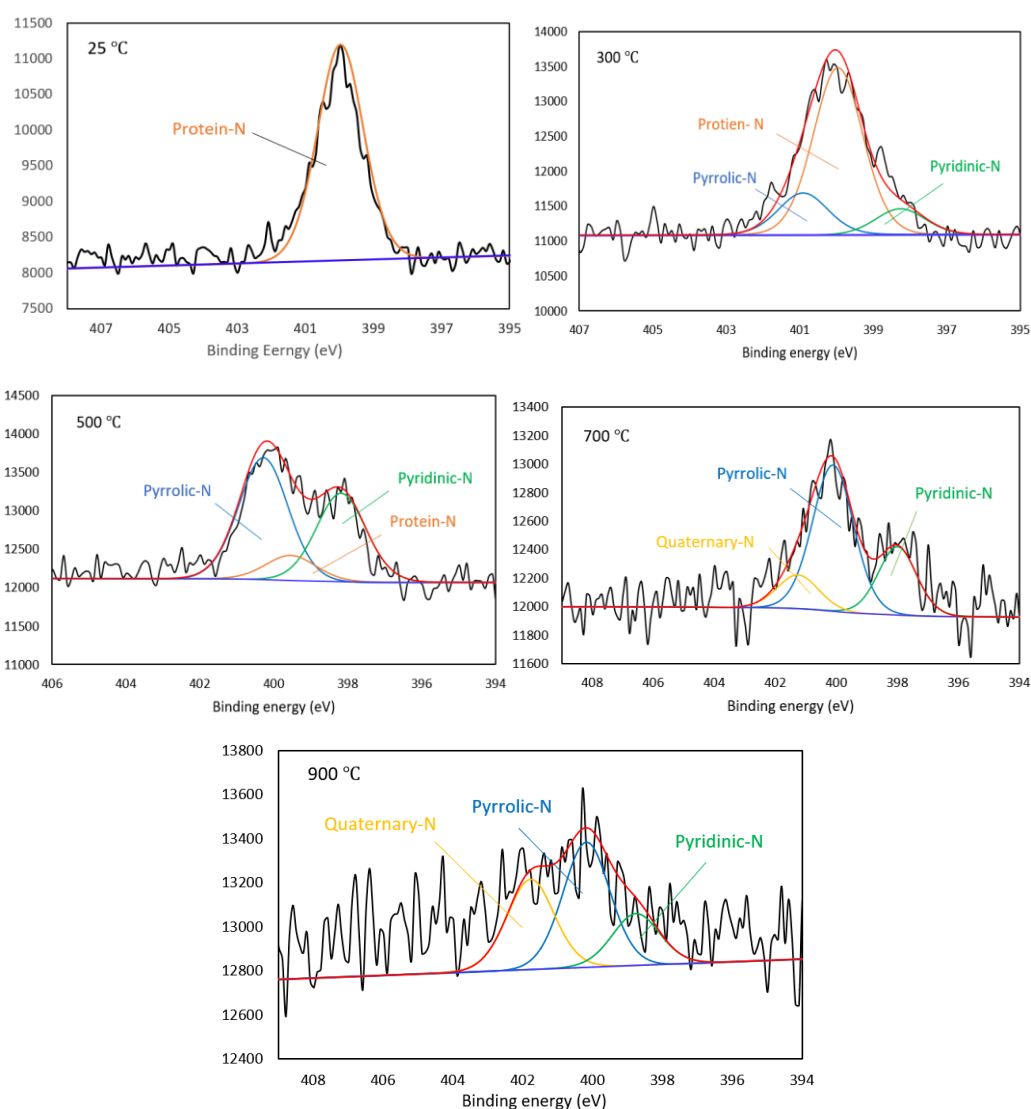


Figure 4-2: N 1s XPS spectra of CHR at different temperature.

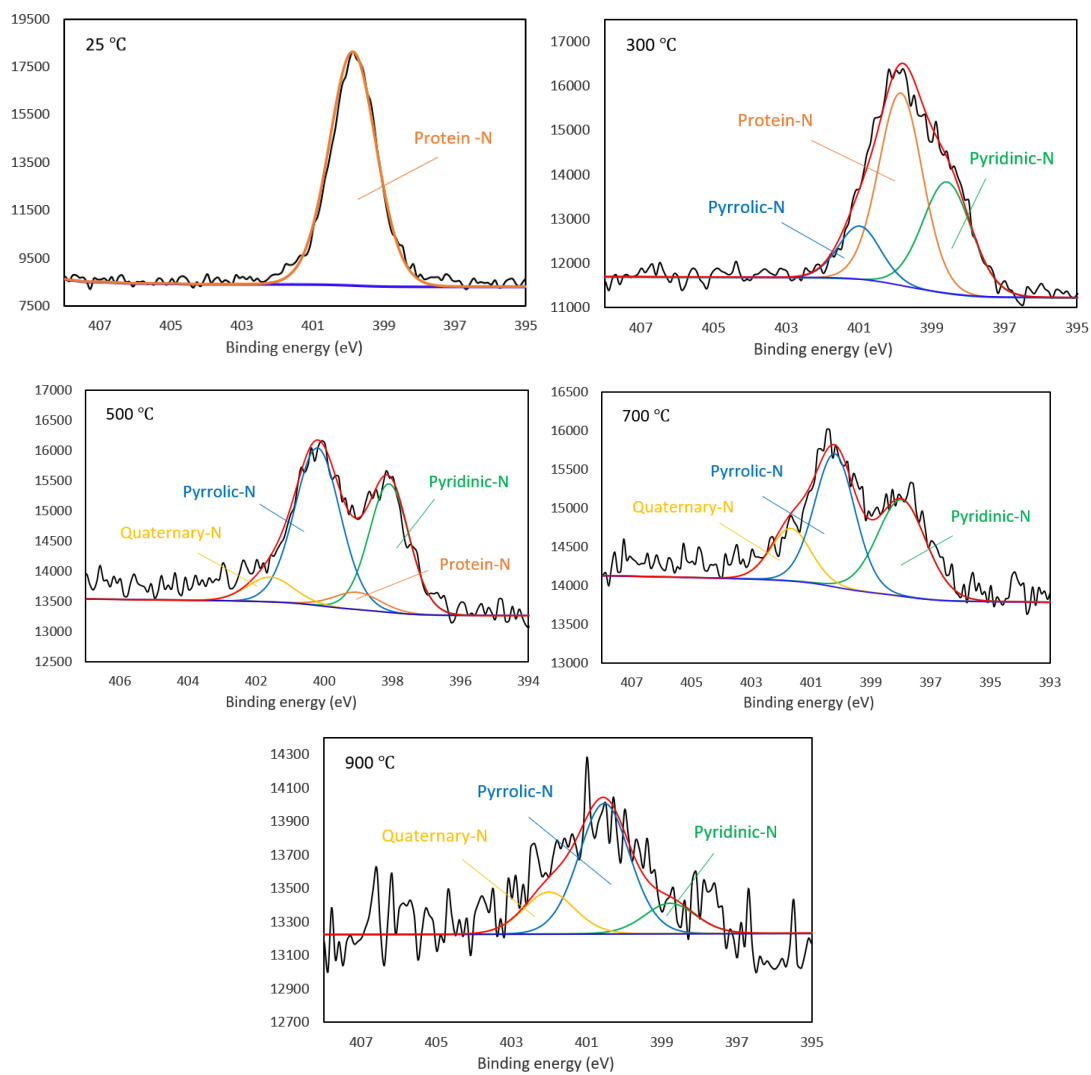


Figure 4-3: N 1s XPS spectra of BS at different temperature.

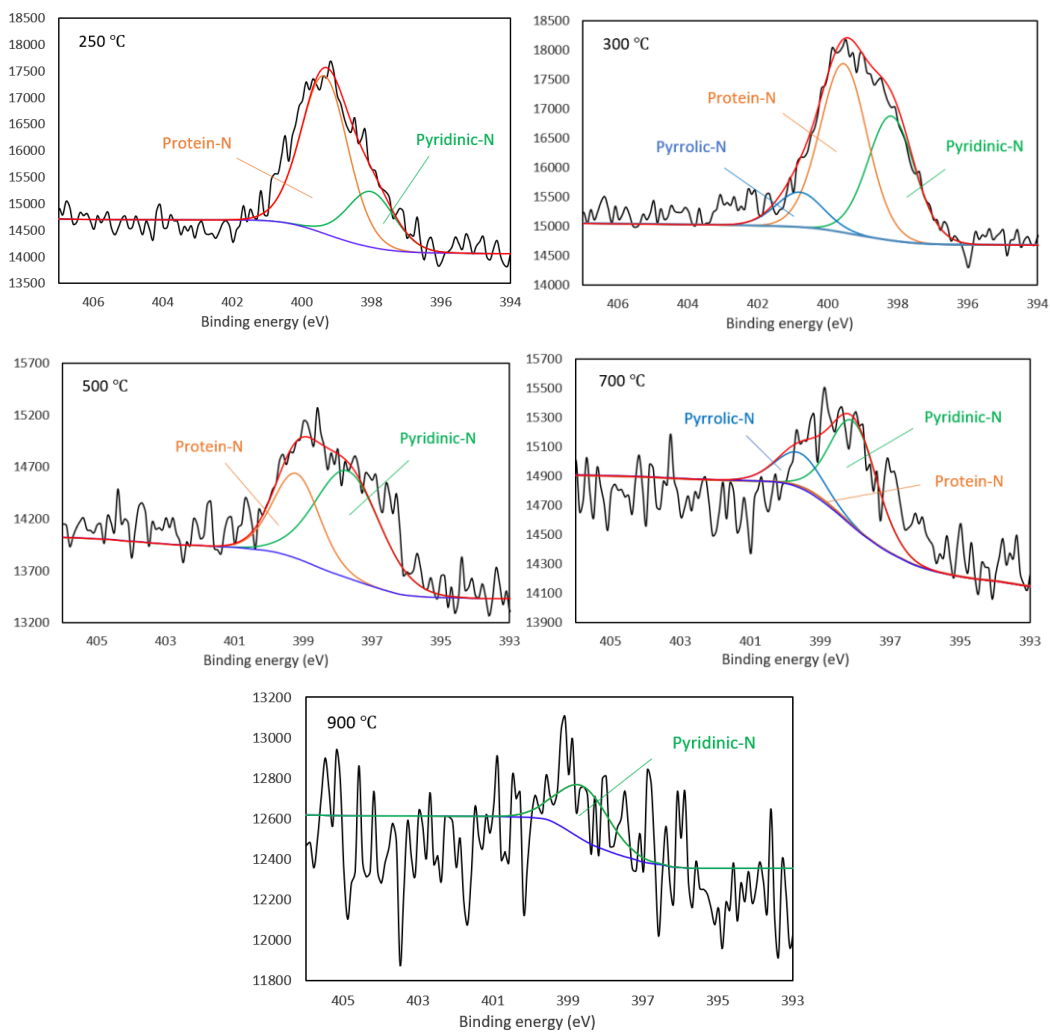


Figure 4-4: N 1s XPS spectra of BS-15pc at different temperature.

Table 4-1: The areas of each N-species of CHR at different temperature.

| Samples   | N-species | pyridinic-N | protein-N   | pyrrolic-N  | quaternary-N | Oxidized-N |
|-----------|-----------|-------------|-------------|-------------|--------------|------------|
|           | eV        | 398.5 ± 0.3 | 399.7 ± 0.4 | 400.2 ± 0.3 | 401.2 ± 0.3  | 402-405    |
| CHR-25°C  | eV        | 399.96      |             |             |              |            |
|           | Areas     | 5236.7      |             |             |              |            |
|           | Nx%       | 0           | 100         | 0           | 0            | 0          |
| CHR-300°C | eV        | 398.26      | 399.96      | 400.91      |              |            |
|           | Areas     | 648.83      | 4077.36     | 1016.74     |              |            |
|           | Nx%       | 11.30       | 71.00       | 17.70       | 0            | 0          |
| CHR-500°C | eV        | 398.18      | 399.54      | 400.28      |              |            |
|           | Areas     | 1965.02     | 565.05      | 2719.28     |              |            |
|           | Nx%       | 37.43       | 10.76       | 51.80       | 0            | 0          |
| CHR-700°C | eV        | 397.99      |             | 400.1       | 401.25       |            |
|           | Areas     | 766.08      |             | 1760.89     | 411.8        |            |
|           | Nx%       | 26.07       | 0           | 59.92       | 14.01        | 0          |
| CHR-900°C | eV        | 398.75      |             | 400.17      | 401.77       |            |
|           | Areas     | 407.61      |             | 981.32      | 707.32       |            |
|           | Nx%       | 19.44       | 0           | 46.81       | 33.74        | 0          |

Table 4-2: The areas of each N-species of BS at different temperature

| Samples  | N-species | pyridinic-N | protein-N   | pyrrolic-N  | quaternary-N | Oxidized-N |
|----------|-----------|-------------|-------------|-------------|--------------|------------|
|          | eV        | 398.5 ± 0.3 | 399.7 ± 0.4 | 400.2 ± 0.3 | 401.2 ± 0.3  | 402-405    |
| BS-25°C  | eV        | 399.88      |             |             |              |            |
|          | Areas     | 16518.67    |             |             |              |            |
|          | Nx%       | 0           | 100         | 0           | 0            | 0          |
| BS-300°C | eV        | 398.58      | 399.85      | 400.98      |              |            |
|          | Areas     | 4336.25     | 6709.44     | 1791.29     |              |            |
|          | Nx%       | 33.78       | 52.27       | 13.95       | 0            | 0          |
| BS-500°C | eV        | 398.1       | 399.04      | 400.2       | 401.58       |            |
|          | Areas     | 3189.64     | 492.21      | 4464.48     | 706.21       |            |
|          | Nx%       | 36.03       | 5.56        | 50.43       | 7.98         | 0          |
| BS-700°C | eV        | 397.97      |             | 400.21      | 401.68       |            |
|          | Areas     | 2587.44     |             | 2965.81     | 1155.42      |            |
|          | Nx%       | 38.57       | 0           | 44.21       | 17.22        | 0          |
| BS-900°C | eV        | 398.77      |             | 400.52      | 401.99       |            |
|          | Areas     | 318.45      |             | 1350.13     | 439.87       |            |
|          | Nx%       | 15.10       | 0           | 64.03       | 20.86        | 0          |

Table 4-3: The areas of each N-species of BS-15pc at different temperature.

| Samples          | N-species | pyridinic-N | protein-N   | pyrrolic-N  | quaternary-N | Oxidized-N |
|------------------|-----------|-------------|-------------|-------------|--------------|------------|
|                  | eV        | 398.5 ± 0.3 | 399.7 ± 0.4 | 400.2 ± 0.3 | 401.2 ± 0.3  | 402-405    |
| BS-15pc<br>250°C | eV        | 398.01      | 399.35      |             |              |            |
|                  | Areas     | 1814.61     | 5107.54     |             |              |            |
|                  | Nx%       | 26.21       | 73.79       | 0           | 0            | 0          |
| BS-15pc<br>300°C | eV        | 398.19      | 399.55      | 400.81      |              |            |
|                  | Areas     | 3641.11     | 4937.99     | 1033.07     |              |            |
|                  | Nx%       | 37.88       | 51.37       | 10.75       | 0            | 0          |
| BS-15pc<br>500°C | eV        | 397.7       | 399.19      |             |              |            |
|                  | Areas     | 2482.86     | 1408.96     |             |              |            |
|                  | Nx%       | 63.80       | 36.20       | 0           | 0            | 0          |
| BS-15pc<br>700°C | eV        | 398.05      | 399.09      | 399.59      |              |            |
|                  | Areas     | 1237.2      | 27.49       | 407.94      |              |            |
|                  | Nx%       | 73.97       | 1.64        | 24.39       | 0            | 0          |
| BS-15pc<br>900°C | eV        | 398.58      |             |             |              |            |
|                  | Areas     | 453.39      |             |             |              |            |
|                  | Nx%       | 100         | 0           | 0           | 0            | 0          |

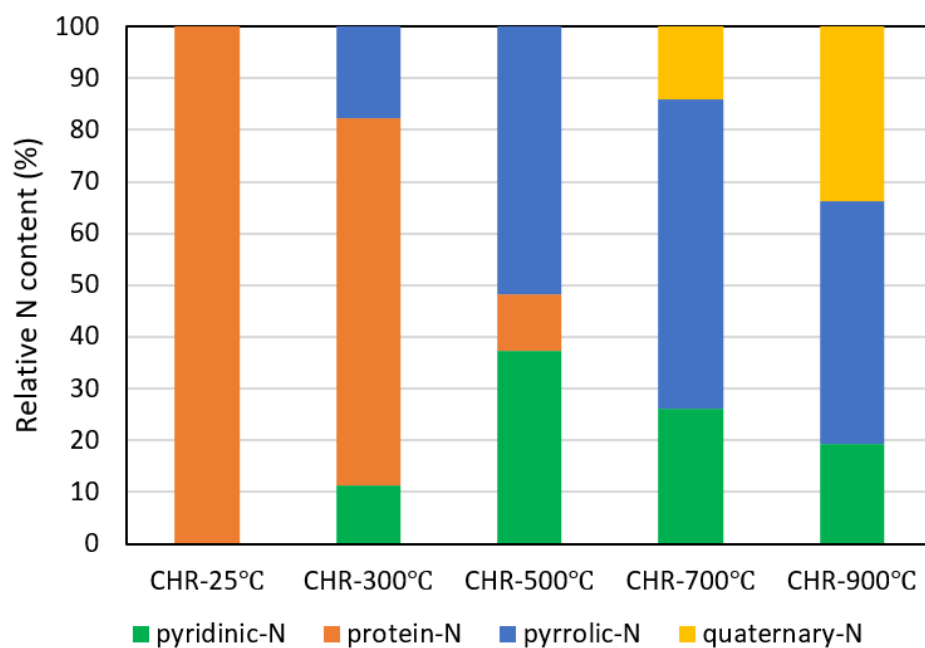


Figure 4-5: Relative N content of N-species for CHR at different temperatures.

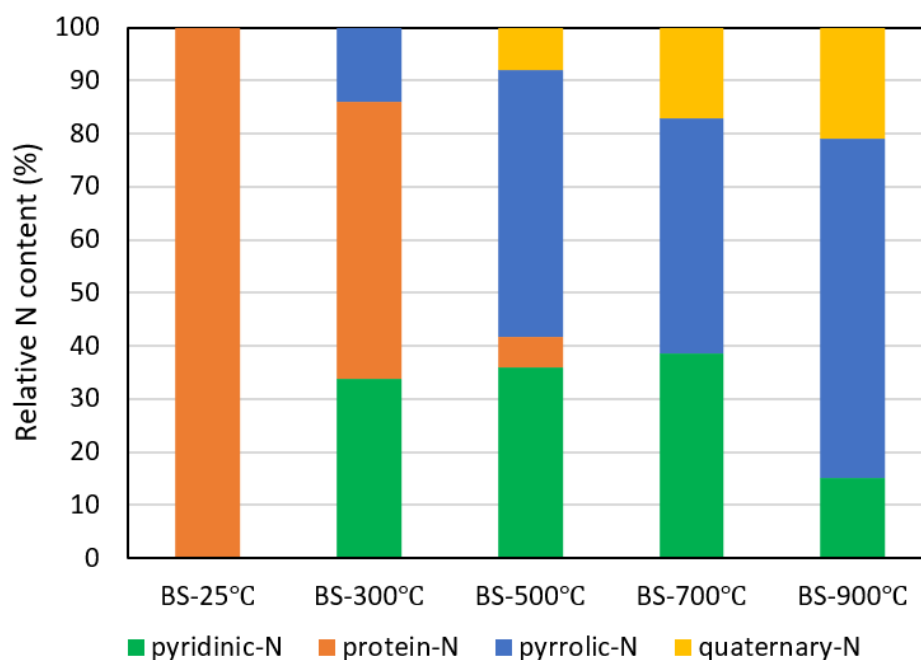


Figure 4-6: Relative N content of N-species for BS at different temperatures.

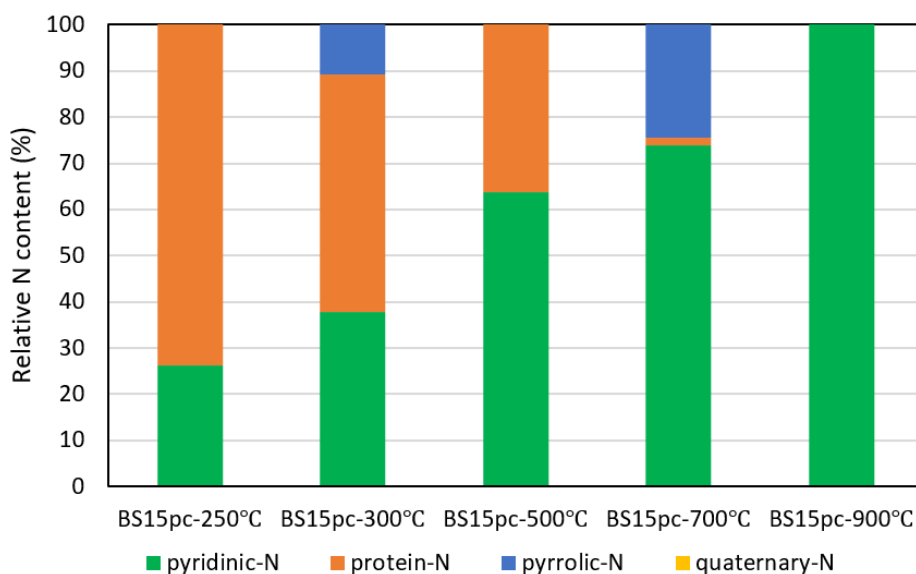


Figure 4-7: Relative N content of N-species for BS-15pc at different temperatures.

From these results, it is clear that the following 4 types of N-containing groups exist in the char product of original BS and CHR materials: pyridinic-N, protein-N, pyrrolic-N and quaternary-N. Three types of N-containing species mainly exist in the catalytic BS pyrolysis product (pyridinic-N, protein-N and pyrrolic-N). The protein-N is the main source of the N content of the original biomass material. The amount of protein-N in char product decreases as pyrolysis temperature increases, while the contents of pyridinic-N, pyrrolic-N and quaternary-N increase. This phenomenon was mainly due to the deamination and the dehydrogenation of amino acids. Compared with the original BS, the catalytic BS generated larger amount of pyridinic-N at 900°C

(100% in BS-15pc and 15% in original BS), and there was no quaternary-N exists in catalytic product. The N-containing groups showed similar distribution characteristics in original BS and CHR pyrolysis at different temperature. At the low temperature range of pyrolysis (300°C to 500°C), the protein-N converted to pyridinic-N and pyrrolic-N gradually. At the pyrolysis temperature of 700°C and 900°C, no protein-N exist in the original CHR and BS and the relative content of quaternary-N increase. The structure of quaternary-N is more stable than pyridinic-N and pyrrolic-N, thus, more pyridinic-N and pyrrolic-N convert to quaternary-N at high temperature. The effect of catalyst is obvious in BS pyrolysis. The content of pyridinic-N increased with the increasing heating temperature for catalytic BS. The structure of pyridinic-N is more stable than that of the pyrrolic-N [198]. The catalyst improved the generation of pyridinic-N but suppressed the generation of quaternary-N in high temperature range. The existence of pyridinic-N and pyrrolic-N in the biomass fuel will reduce the release of NO<sub>x</sub> pollutants during the thermochemical conversion [199]. Thus, the use of catalyst can realize the clean utilization of biomass fuel.

#### 4.4 Conclusion and recommendation

In general, the evolution of N-containing groups of biomass pyrolysis could be studied using XPS analysis method. According to the literature, the formation of each NO<sub>x</sub> precursors component depends on the characteristics of N-containing functionalities [196]. To reduce the release of N pollutants, the study of the evolution and formation mechanisms of N species in biomass is important. The existing form of N-containing functionalities in CHR and BS is protein-N. As the pyrolysis temperature increasing, the unstable protein-N experienced deamination reaction and released as NH<sub>3</sub>. The stable protein-N is gradually converted to the more stable pyridinic-N and pyrrolic-N through crosslinking reactions [196]. At high temperature condition, the content of quaternary-N increase. This is due to the N structure is easily transformed to a more stable structure at high temperature. The catalyst will increase the efficiency of transformation from protein-N to pyridinic-N.

The investigation of characteristics and influencing factors of the NO<sub>x</sub> precursors formation is important to reduce the release of N pollutants during pyrolysis process. This section only focused on the study of the evolution of N-containing functionalities during pyrolysis at different temperature condition. Different operation conditions should be investigated in the further study, such as the heating rate and reaction type. To deep understand the nitrogen reduction method, the research on the release characteristics N-containing gas (NH<sub>3</sub>, HNCO, HCN and NO<sub>x</sub>) should be developed in further study.



## Chapter 5. Modelling and experimental study of single large herb residue particle during pyrolysis

### 5.1 Introduction

This chapter introduces the simulation results of single particle model during pyrolysis process. A three-dimensional cylinder particle model was developed to investigate the heat and mass transfer within the particle. The slow pyrolysis experiment was designed to verify the simulation results. The Chinese herb residues are selected to carry out the experiment. The finite volume approach is used to describe the numerical model. This model aims to predict the heating-up behaviour of biomass particles pyrolysis and investigate the effect of particle shape on pyrolysis behaviour. A number of researchers studied the effect of particle shape on biomass thermochemical conversion behaviour [200, 201].

### 5.2 Materials and experimental methods


#### 5.2.1 Material properties

In this work, the Chinese herb residues are investigated experimentally to carry out the pyrolysis process. The proximate and ultimate analysis of the samples are presented in Table 5-1. The herb residues particles are obtained by pressure forming method (Table 5-2). To prevent cracks in the particles, 8-10% water is added to the powder to form the cylinder shape.

Table 5-1: Proximate and ultimate analysis (Dried at 105 °C) [182].

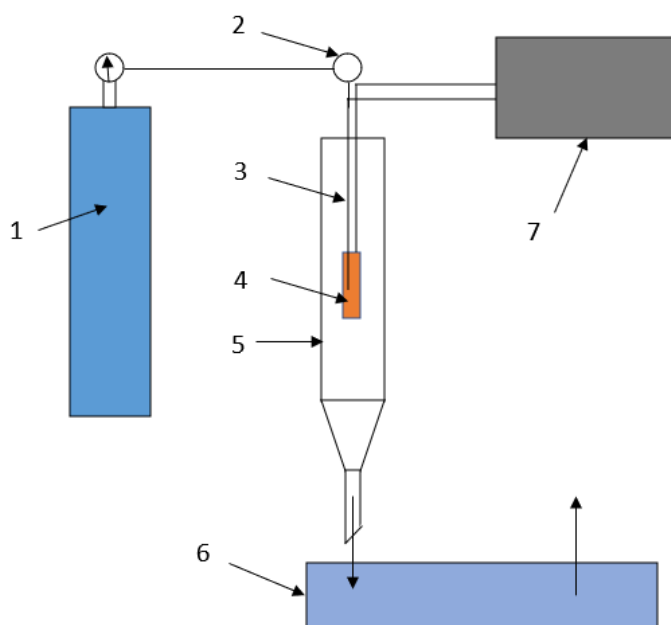
| Samples | Proximate analysis (wt%) |                |                 | Ultimate analysis (wt%) |                |                |                |                 | Heating value<br>LHV <sub>cal</sub> (MJ/kg) |
|---------|--------------------------|----------------|-----------------|-------------------------|----------------|----------------|----------------|-----------------|---|
|         | A <sub>d</sub>           | V <sub>d</sub> | FC <sub>d</sub> | C <sub>d</sub>          | H <sub>d</sub> | N <sub>d</sub> | S <sub>d</sub> | O* <sub>d</sub> |   |
| Herb    | 3.37                     | 80.87          | 15.76           | 46.91                   | 6.06           | 0.79           | --             | 42.88           | 17.27                                       |

Table 5-2: Selection of particles using in experiment.

| Particle structure  | Dimension |         |
|---|-----------|---------|
|  | Diameter  | ≈ 10 mm |
|   | Length    | ≈ 20 mm |
|   | Mass      | ≈ 2 g   |

## 5.2.2 Experimental approach

A two-stage electric furnace was used for slow pyrolysis experiments. The herb particles were dried by preheating the electric furnace at 110 °C, and the particles were rapidly cooled at different time points, then taken out for measurement and analysis. High purity nitrogen was used as protection gas to achieve an anaerobic environment for biomass pyrolysis (flow rate=100 ml/min). The temperature of the particle centre is monitored by two thermocouples (surface temperature and centre temperature). A telescopic device was used to control the descending and lifting of the particle. The herb residue particle was dried overnight at 105 °C. The herb residue particle was suspended on the top of the reactor when the furnace was heating up. The particle was dropped to the centre of the furnace after the furnace was heated to the set temperature. In the first stage of experiments, the fixed pyrolysis temperature was 550 °C, then the experiments were terminated at the time points of 250 °C, 350 °C, 450 °C, 550 °C and 550 °C (constant temperature for 30 minutes). Figure 5-2 presents the experimental setup and the measurement points. T1 is the centre temperature of the particle, T2 is the temperature of the side surface and T3 is the temperature of the heating furnace. The centre thermocouple was inserted in the depth of 5.5 mm inside the particle to measure T1. The experimental temperature sampling points are shown in Figure 5-3.



*Figure 5-1: Schematic diagram of herb particle pyrolysis system. (1) Nitrogen; (2) Flowmeter; (3) Thermocouple; (4) Herb residue particle; (5) Reactor; (6) Condenser; (7) Temperature acquisition device.*

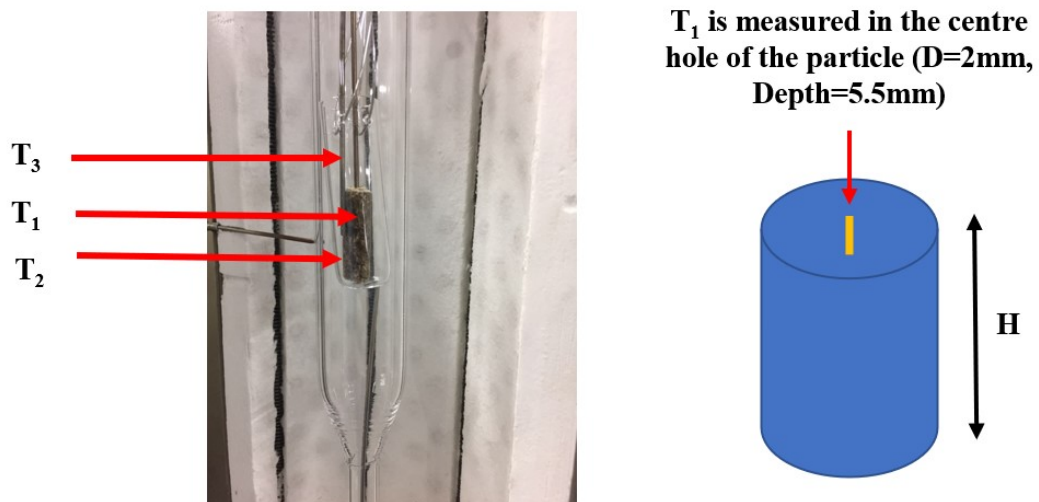


Figure 5-2: The schematic diagram of single particle pyrolysis experimental setup and measurement points.

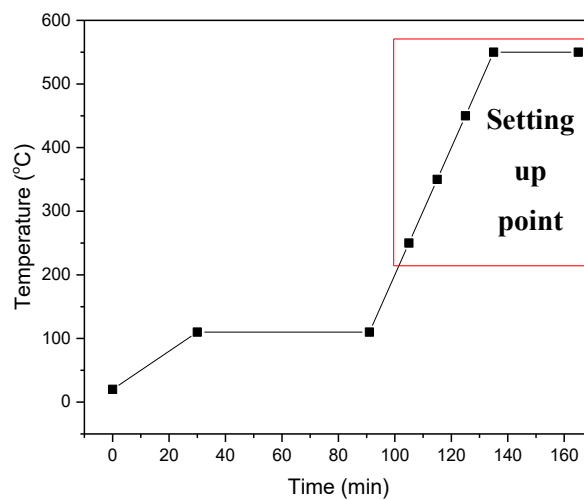














Figure 5-3: Theoretical heating curve of experimental sampling point.

The whole experiment was divided into five groups (KL-01, KL-02, KL-03, KL-04, KL-05). The experimental recordings of particle geometry are shown in Table 5-3. From Table 5-3, a clear particle size change can be seen from the figures.

Table 5-3: The change of the geometry of the herb residue particles

| 00  | 01  | 02  | 03   | 04  | 05  |
|---|---|---|--|---|---|
| Original sample-105 °C  | 280 °C-1min   | 350 °C-1min   | 450 °C-1min  | 550 °C-1min   | 550 °C-30min  |
|  |  |  |  |  |  |
|  |  |  |  |  |  |

## 5.3 Numerical model

### 5.3.1 Model description

The objective of this study is to investigate the heat and mass transfer within the single large particle. Once the particles are exposed to the high temperature furnace, the particles are heated by radiation and convection by the surrounding furnace walls, leading to the surface temperature of the particles increase. Then the heat is transferred from the surface to the centre of the particle. Considering the temperature gradient within the large particle, the devolatilization occurs once the local temperature inside the particle reaches to the reaction temperature [202].

Most of previous studies focus on isothermal model when modelling the thermochemical conversion of single particle. In fact, the results of isothermal model can only be validated in small particles ( $Bi < 1$ ). For large particles ( $Bi > 1$ ), the results are not reasonable. The results of the isothermal model predicted a shorter reaction time than the thermally-thick model [203]. Thus, the non-thermally thick model is considered in this simulation to get more accuracy results.

In this study, a three-dimensional particle model was developed in Mathematica using a finite volume approach. As the increasing temperature, the heat transfer to the central area of the particle and the biomass decomposes into char and volatiles. The moisture content within the biomass particle was ignored since the experimental particle has been dried overnight. The shrinkage and the porosity are considered in the model. The particle is modelled as three-dimensional cylinder model (diameter=10mm, length=20mm). The initial environment is 378K

(105°C), then the particle is heated to 823K (550°C).

### 5.3.2 Mass and energy conservation

From the kinetic study in Section 3.2, the thermal decomposition of solid components of the particle is described by Eq. (5-1).

$$\alpha = \frac{m_0 - m_t}{m_0 - m_\infty} \quad (5-1)$$

$$\frac{d\alpha}{dt} = A \exp\left(-\frac{E_\alpha}{RT}\right) f(\alpha) \quad (5-2)$$

Where  $\alpha$  is the conversion rate,  $m_0$ ,  $m_t$ ,  $m_\infty$  are the initial mass of the particle, mass at time t and final mass of the sample, respectively.

From the discussion of the Chapter 3, the integrated mechanism function  $G(\alpha)$  could be concluded by a modified D3-Jander model Dn:

$$G(\alpha) = \left[1 - (1 - \alpha)^{\frac{1}{3}}\right]^n \quad (5-3)$$

Where n is the reaction coefficient, which could be solved by master plot method. The  $f(\alpha)$  is the differential mechanism function of  $G(\alpha)$ .

Thus, the mass variation of the dry biomass at  $\Delta t$  could be presented as:

$$\Delta m = \Delta t m_0 A \exp\left(-\frac{E_\alpha}{RT}\right) f(\alpha) \quad (5-4)$$

The mass evolution of dry biomass at current time t is:

$$m_t = m_{t-1} + \Delta m \quad (5-5)$$

At  $t=0$ ,  $m_0 = \rho_B V_{P0}(1 - \varphi_0)$ , the  $\varphi_0$  is the initial porosity of the particle.

The energy conservation of the solid particles is expressed by considering the heat conduction, radiation, and heat release during the conversion. The energy conservation equation is described in Eq. (5-6).

$$(1 - \varphi)\rho_B C_{P(B)} \frac{\partial T_P}{\partial t} = \frac{1}{r^2} \frac{\partial}{\partial r} \left( r^2 k_{\text{eff}} \frac{\partial T_P}{\partial r} \right) + \sum \dot{r}_i \Delta H_i + \tilde{Q} \quad (5-6)$$

where  $r$  is the radius direction of the particle,  $\dot{r}_i$  represents the conversion rate ( $i=M, V, C$  representing the moisture, volatile and carbon, respectively). The initial and boundary conditions for the above equations are:

At  $t = 0$ ,  $T_p = 378K$ ;

At  $r = 0$ ,

$$\frac{\partial T_P}{\partial r} = 0 \quad (5-7)$$

At  $r = R$ ,

$$\frac{\partial T_P}{\partial r} = k_{\text{eff}} \frac{\partial T_P}{\partial r} - \omega \sigma (T_{\text{env}}^4 - T_P^4) \quad (5-8)$$

The effective thermal heat transfer coefficient is described as Eq. (5-9) [91].

$$k_{\text{eff}} = \eta \times k_B + (1 - \eta) \times k_C + \varphi \times k_V + 13.5 \sigma T_P^3 l_{\text{pore}} / \omega \quad (5-9)$$

Where  $\eta$  is the ratio of the current biomass mass to the initial mass,  $\eta = m_B/m_{B0}$ . The parameter  $\varphi$  is the local porosity of the biomass particle, which is related to the drying and devolatilization processes [129]. It varies as a linear relationship with the conversion process (Eq. (5-10)).

$$\varphi = \varphi_0 + (1 - \varphi_0) [\alpha_M (X_{M0} - X_M) + \alpha_V (X_{V0} - X_V) + \alpha_C (X_{C0} - X_C)] \quad (5-10)$$

where  $\alpha_M$ ,  $\alpha_V$  and  $\alpha_C$  are the dimensionless parameter of the particle shrinkage during each conversion processes.  $X_M$ ,  $X_V$  and  $X_C$  are the mass fraction at time  $t$ . The particle volume varies during the conversion processes are considered from the total mass conservation. In this case, the moisture part is ignored.

$$V_P = \frac{(1-\varphi_0)\rho_{B0}V_{P0}-\Delta m_B}{(1-\varphi)\rho_B} \quad (5-11)$$

Table 5-4 lists the related variables in these equations. The activation energy, pre-exponential factor and the reaction coefficient has been calculated in Section 3.

Table 5-4: Properties and kinetic data.

|            |                                 |                                  |                                    |            |
|------------|---------------------------------|----------------------------------|------------------------------------|------------|
| $\rho_B$   | Density                         | 1277.8                           | kg m <sup>-3</sup>                 |            |
| $X_{V0}$   | Volatile matter (VM)            | 70.271                           | wt. %                              |            |
| $X_{C0}$   | Fixed carbon (FC)               | 24.179                           | wt. %                              |            |
| $X_A$      | Ash                             | 5.55                             | wt. %                              |            |
| $C_{p(B)}$ | Heat Capacity of biomass        | $1112 + 4.85 \times (T_p - 273)$ | J kg <sup>-1</sup> K <sup>-1</sup> | [204]      |
| $C_{p(V)}$ | Heat Capacity of volatile       | $1050 + 0.18 \times (T_p - 273)$ | J kg <sup>-1</sup> K <sup>-1</sup> |            |
| $C_{p(C)}$ | Heat Capacity of char           | $1390 + 0.36 \times (T_p - 273)$ | J kg <sup>-1</sup> K <sup>-1</sup> | [205]      |
| $C_{p(M)}$ | Heat Capacity of moisture       | 4280                             | J kg <sup>-1</sup> K <sup>-1</sup> |            |
| A          | Pre-exponential factor          | $1.84 \times 10^{12}$            | s <sup>-1</sup>                    |            |
| E          | Activation energy               | 189.904                          | kJ mol <sup>-1</sup>               |            |
| n          | Reaction coefficient            | 2.8867                           |                                    |            |
| $k_M$      | Thermal conductivity (moisture) | 0.653                            | w m <sup>-1</sup> K <sup>-1</sup>  | [129, 206] |

|              |                                 |                       |                   |           |
|--------------|---------------------------------|-----------------------|-------------------|-----------|
| $k_v$        | Thermal conductivity (volatile) | 0.2                   | $w m^{-1} K^{-1}$ | [129]     |
| $k_c$        | Thermal conductivity (char)     | 0.15                  | $w m^{-1} K^{-1}$ | [129]     |
| $k_A$        | Thermal conductivity (ash)      | 0.1                   | $w m^{-1} K^{-1}$ | [129]     |
| $k_B$        | Thermal conductivity (biomass)  | 0.21                  | $w m^{-1} K^{-1}$ | [207]     |
| $\Delta H_m$ | Reaction heat (moisture)        | -270                  | $kJ kg^{-1}$      | [91, 208] |
| $\Delta H_v$ | Reaction heat (volatile)        | -418                  | $kJ kg^{-1}$      | [91]      |
| $\Delta H_c$ | Reaction heat (char)            | -418                  | $kJ kg^{-1}$      | [91]      |
| $\omega$     | Pore emissivity                 | 1                     | -                 | [206]     |
| $l_{pore}$   | Pore size                       | $5 \times 10^{-5}$    | m                 | [129]     |
| $\sigma$     | Stefan-Boltzmann constant       | $5.67 \times 10^{-8}$ | $w m^{-2} K^{-4}$ | [209]     |

### 5.3.3 Finite volume approach

The intra-particle mass transfer was considered by volume averaging method and the mass variation changes with the position at each time step. The simulation domain is divided into two directions: 50 volumes in x direction ( $N_x=50$ ) and 100 volumes in y direction ( $N_y=100$ ). To simplify the calculation the whole volume of the particle is divided into 5 parts in y direction and 2 parts in x direction.

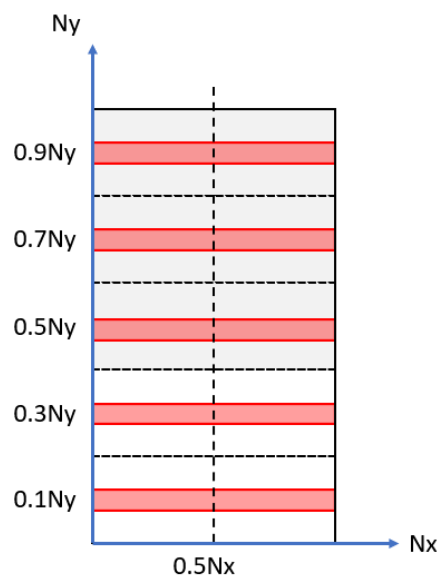


Figure 5-4: Schematic of division of cylinder particle.

The estimation of calculating averaging particle mass variation at time  $t$  is calculated by each particle volume:

$$\Delta m_i = \frac{\sum_j^{j \cdot N_y \cdot 0.5 \cdot N_x + 0.5 \cdot N_x} (2\pi \cdot r_i \cdot \Delta r \cdot L_1)}{\pi R^2 L_1} \cdot \Delta m \quad (5-12)$$

Where  $\Delta m$  is expressed in Eq. (5-12), and  $j$  is equal to 0.1, 0.3, 0.5, 0.7, 0.9. The total mass variation is calculated as the mean value of five parts. The initial conditions of the samples are at 378 K, and it is assumed that the particles exposed to the heating source at time 0.

## 5.4 Results and discussion

### 5.4.1 Mass loss

The pyrolysis of single particle model has been validated by the experimental data. The mass loss of the experiment was measured at different pyrolysis temperature points (Figure 5-5). The mass evolution of the particle is recorded in Table 5-5. The final mass variation of the whole pyrolysis process at 550 °C is 67.806 %. The remaining matter is mainly consisted by a mixture of carbonaceous solid residues (including formed char from reaction, fixed carbon and ash matter). These carbonaceous matters can produce a slow combustion reaction in an oxidization environment [210]. Once the particle exposed to the heating temperature, the heat transferred from the surface to the centre area, at the same time, the particle is decomposed while producing volatiles and char. As the temperature increasing, the volatile product gradually disappears, and the char product remains at the particle. From the Figure 5-5, the mass fraction of the particle sharply decreases at the residence time from 500s to 1500s, then, the mass fraction descends slightly. The simulated pyrolysis temperature of the single particle is 873K. The weight loss of the particle mainly occurs at 500s to 1500s, corresponding to the pyrolysis temperature 200°C to 350°C.

The results show that the simulated mass loss is overpredicted compared with the experimental results in terms of the volatile matter from 500s to 1500s. This discrepancy is because of that the kinetic parameters calculated in Section 3 is obtained within the temperature range of 150 to 377C. Thus, the kinetic parameters used in the model cannot fully describe the kinetic conversion of the model at high temperature range. The single kinetic model is used in the model, which will largely affect the simulation results. Also, the measurement methods of mass loss in experiment will lead to discrepancy, since it is necessary to cool down the furnace before removing the particle at each temperature point, the mass is continue losing during this step.



However, the simulation results cannot reflect this error.

Table 5-5: Experimental results of the geometrical parameters.

| Sample   | Diameter (mm)        |                      |                      | Height        | Hole depth (mm) | Mass                     |
|--|----------------------|----------------------|----------------------|---------------|-----------------|--------------------------|
|  | <b>D<sub>1</sub></b> | <b>D<sub>2</sub></b> | <b>D<sub>3</sub></b> | <b>H (mm)</b> |                 | <b>m<sub>1</sub> (g)</b> |
| Sample 01 (280 °C-1min), $\Delta$ Mass = 23.335 %  |                      |                      |                      |               |                 |                          |
| Initial particle-01                                | 10.10                | 10.14                | 10.11                | 19.20         | 7.97            | 1.8663                   |
| Pyrolysis particle-01                              | 9.94                 | 10.03                | 9.96                 | 18.82         | 6.55            | 1.4307                   |
| Sample 02 (350 °C-1min), $\Delta$ Mass = 55.815 %  |                      |                      |                      |               |                 |                          |
| Initial particle-02                                | 10.18                | 10.19                | 10.11                | 18.93         | 5.72            | 1.9520                   |
| Pyrolysis particle-02                              | 9.36                 | 9.13                 | 9.26                 | 16.11         | 4.35            | 0.8625                   |
| Sample 03 (450 °C-1min), $\Delta$ Mass = 63.852 %  |                      |                      |                      |               |                 |                          |
| Initial particle-03                                | 10.18                | 10.16                | 10.12                | 20.36         | 5.35            | 2.0217                   |
| Pyrolysis particle-03                              | 8.85                 | 8.72                 | 8.66                 | 16.35         | 4.03            | 0.7308                   |
| Sample 04 (550 °C-1min), $\Delta$ Mass = 67.806 %  |                      |                      |                      |               |                 |                          |
| Initial particle-04                                | 10.18                | 10.15                | 10.09                | 20.26         | 11.18           | 1.9960                   |
| Pyrolysis particle-04                              | 8.35                 | 8.33                 | 8.21                 | 15.66         | 9.15            | 0.6426                   |
| Sample 06 (550 °C-30min), $\Delta$ Mass = 69.200 % |                      |                      |                      |               |                 |                          |
| Initial particle-05                                | 10.12                | 10.19                | 10.21                | 20.27         | 5.05            | 2.0120                   |
| Pyrolysis particle-05                              | 8.40                 | 8.31                 | 8.20                 | 15.28         | 4.45            | 0.6197                   |

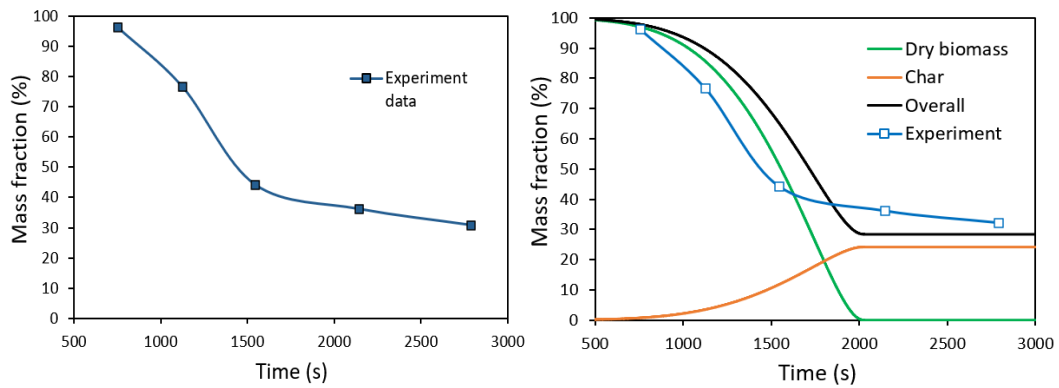


Figure 5-5: Experimental data of mass loss rate.

### 5.4.2 Temperature distribution

The cross-sectional contour plot of temperature distribution within the particle model over time is shown in Figure 5-6. As the increasing pyrolysis time, the difference of temperature between the core and surface of the particle increase as well. Figure 5-7 indicates the surface temperature and the centre temperature within the particle as a function of time. In the temperature range of 300°C and 450°C, the largest temperature difference exists between the core and surface of the particle. At high temperature range (450-550C), the temperature distribution tends to be consistent in the particle.

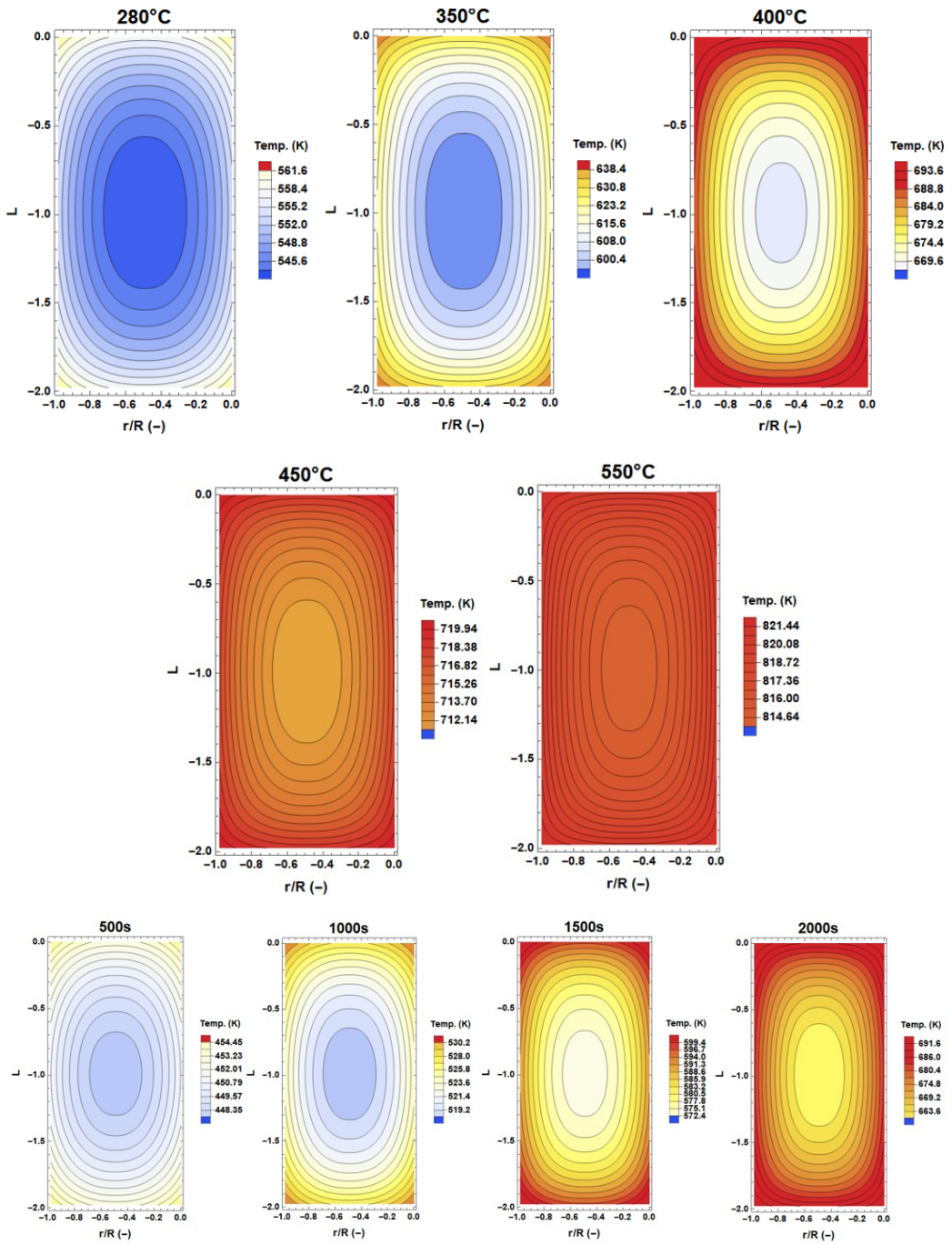


Figure 5-6: Cross sectional Contour plot of temperature distribution inside the particle at different pyrolysis temperature and measuring time.

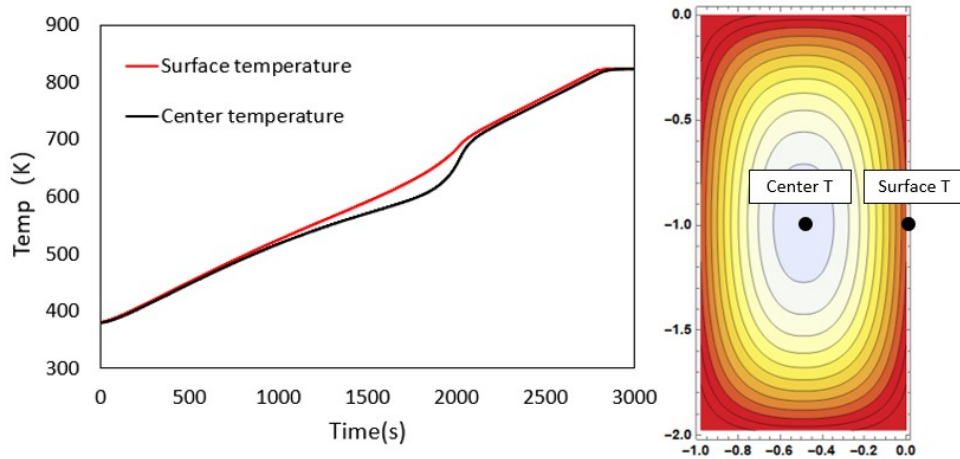


Figure 5-7: Temperature evolution of the model as a function of time (surface and centre temperature).

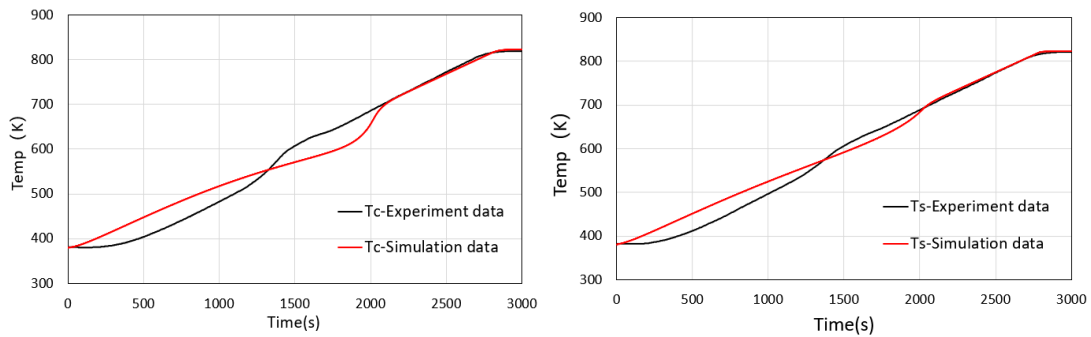


Figure 5-8: Predicted and measured centre temperature and the surface temperature of particle.

Figure 5-7 gives the temperature evolution of the surface temperature and the centre temperature of the particle model as a function of time. Figure 5-8 shows the predicted and measured the temperature distributions of the model. The simulation data increases linearly until 1800s, then suddenly rises at 2000s. From Figure 5-5, biomass material and volatile have gone away, and only char remains in the particle. the calculation of thermal heat transfer coefficient is the sum of the three components (Equation 5-7), thus, only the thermal coefficient of char plays a role in the last stage. The heating up process of the furnace is not considered in the model, which means the convective heat transfer between the furnace and particle is ignored, thus, the heat transfer within the particle will be faster than the real experiment.

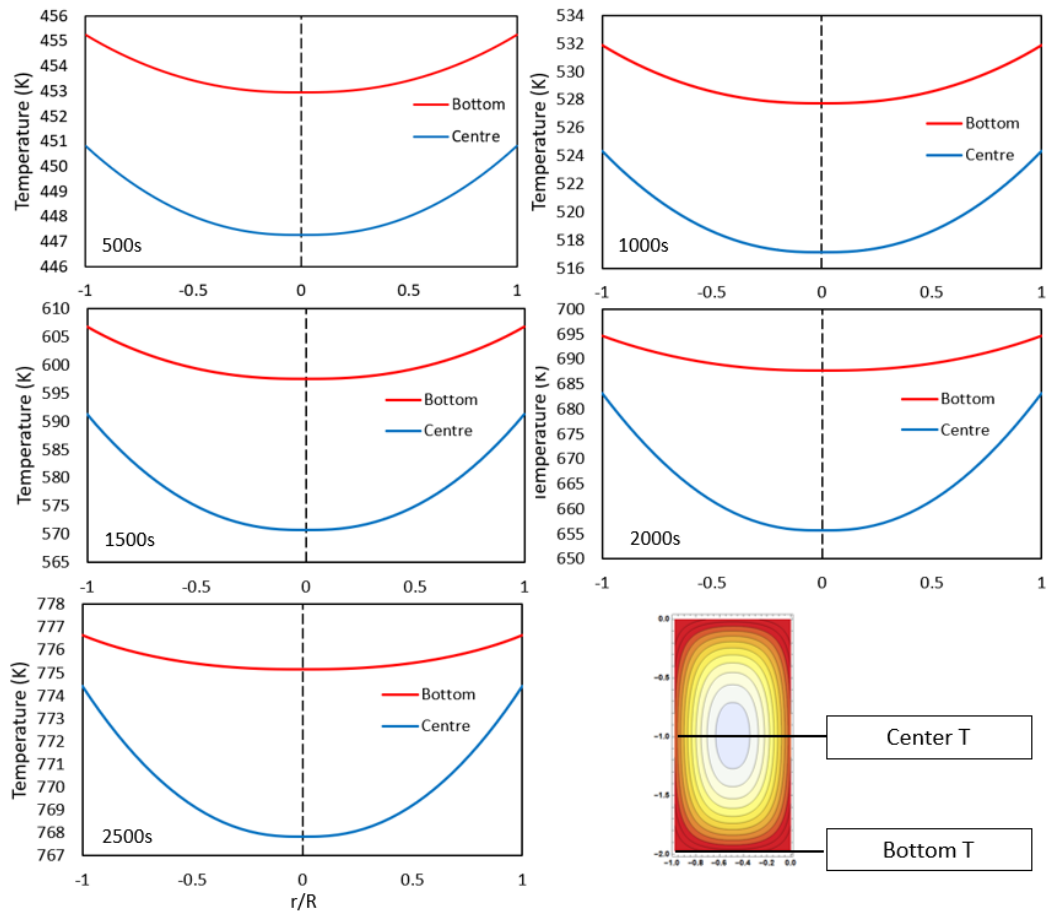


Figure 5-9: Radial temperature distribution against particle radius at different time.

Figure 5-9 and Figure 5-10 are the temperature distribution against particle radius and length at different time. The temperature difference between the core and surface of the particles increases with the increase of the reaction time.

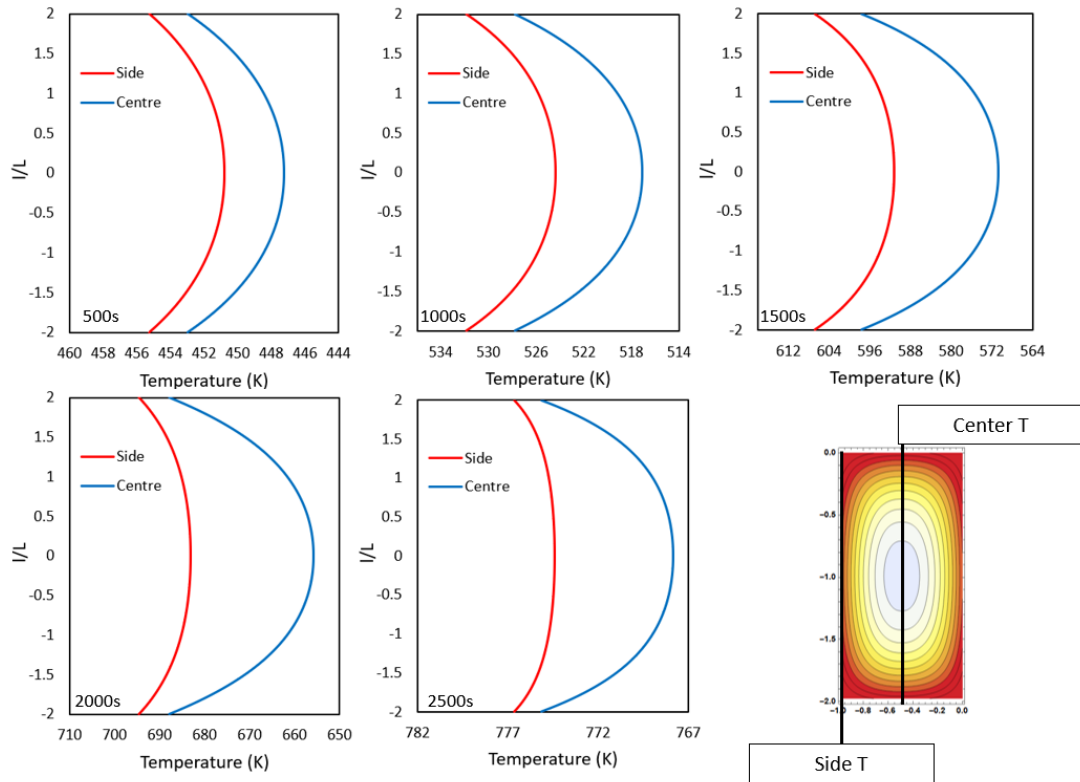


Figure 5-10: Axial temperature distribution against particle length at different time.

## 5.5 Conclusions

The model has been built with an assumption of a perfectly symmetrical cylinder biomass pellet without the shrinkage of the particle. The change of porosity is considered in the simulation. There are five individual pyrolysis experiment of the single large particle were carried out to record the mass loss and temperature results. The simulated results have been validated by the experimental data and it is found that the simulation results are overpredicted in high temperature range. For the further models, the kinetic parameters should be considered by two ranges: low temperature and high temperature. The effect of the volume shrinkage also should be considered in the model.

The particle size affects the heat and mass transfer properties during pyrolysis; thus, the influence of the particle size and aspect ratio can be considered in the simulation. Also, the experiment can be developed under different condition, including the pyrolysis temperature, and the heating up rate. Thus, the effect of the heat transfer coefficient, the heat capacity and thermal conductivity will be investigated.

## Chapter 6. Modelling the pyrolysis process of single biomass particle with a size distribution

### 6.1 Introduction

This part introduces the simulation results of the biomass pyrolysis model with non-isothermal and isothermal kinetics. The heating-up, drying and devolatilisation time at different temperatures (773K, 873K and 973K) and the conversion rate are studied. The particle size distribution obtained from the Monte Carlo sampling method are investigated and validated. Total residence time of the pyrolysis is 10 seconds (100-time steps) and 50 samples are discrete into 100 volumes in each particle. The simulation model is validated by applying the experimental parameters into the model and compared with the data obtained from experiment.

### 6.2 Particle size distribution

The particle size distribution investigated in this report was based on the lognormal distribution:

$$\ln(X) \sim N(\mu, \sigma^2) \quad (6-1)$$

The lognormal probability density function is:

$$f(x | \mu, \sigma^2) = \frac{1}{x\sqrt{2\pi} \ln \sigma} \exp \left[ -\frac{1}{2} \left( \frac{\ln\left(\frac{x}{\mu}\right)}{\ln \sigma} \right)^2 \right] \quad (6-2)$$

Where  $\mu$  is the mean value of the distribution,  $\sigma$  stands for the standard deviation. The function can be used to determine the particle size distribution. In this model, the mean particle size is  $\mu=1$ , and the standard deviation is  $\sigma=2$ . The Monte Carlo sampling method is used to generate a set of 50 particles based on this distribution randomly.

#### 6.2.1 Monte Carlo sampling method

The Monte Carlo sampling method was carried out in Mathematica software, and the Mathematica code was developed by Yu et al. [178]. The Monte Carlo sampling has been used to identify a sample of discrete particles from a probability density function. The continuous data is divided into bins and the algorithm decides how many samples should be taken from each bin to give a good representation of the overall distribution. The 50 samples were taken from the lognormal distribution randomly. The Mathematica code used in the simulation is shown in Figure 6-1.

```

Npop=50
V=N[NestWhileList[#(2)&,10,#<10000&]]
Ni=Integrate[PDF[LogNormalDistribution[Log[1000],Log[2]],u],[211]]
Ni=NIntegrate[PDF[LogNormalDistribution[Log[1000],Log[2]],u],{u,V[[#]],V[[#+1]]}&]/
@Range[Length[V]-1]
ndata=Round[Ni 50]
Total[ndata]

While[Total[ndata]<50,
ndata[[Flatten[Position[ndata,Max[ndata]]]
[[Random[Integer,{1,Length[Flatten[Position[ndata,Max[ndata]]]}]]]]+=1.]
While[Total[ndata]>50,
ndata[[Flatten[Position[ndata,Max[ndata]]]
[[Random[Integer,
{1,Length[Flatten[Position[ndata,Max[ndata]]]}]]]]-=1.]
vol=Partition[#&/@V,2,1]

mdata1=
Pi*
Power[Flatten[Table[Random[Real,Partition[#&/@V,2,1][[#]],
{ndata[[#]]}&/@Range[Length[ndata]]*10^-6,3]*1200/6;
mdata1droplet=Table[{0,mdata1[[i]]},{i,1,Length[mdata1],1}];
a=Select[mdata1,#>(5*10^-9)&]

Length[a]
Mean[a]
ClearAll[x]
PDF[LogNormalDistribution[Log[1000],Log[2]],x]
Integrate[/(x Log[2]),{212}]

Plot[1/2 (1+Erf[(Log[x/1000])/Log[4]]),{x,10^-9,10000},{AxesOrigin->{0,0}}]

LogLinearPlot[PDF[LogNormalDistribution[Log[1000],Log[2]],x],{x,1,10000},
PlotRange->{{10,10^4},{0,0.001}},ImageSize->800,
FrameLabel->{Style["L (µm)",Bold,FontSize->25],

```



```

Style["n(L) (1/μm) ",Bold,FontSize-> 25}],
BaseStyle->{FontSize->20,FontFamily->"Calibri"}]
For[n=0,n<1,n++,l=Table[0,{50}];
For[i=0,i<50,i++,c=RandomReal[];
d= Solve[1/2 (1+Erf[( Log[x/1000])/Log[4]])==c,x];
e=x/.d;
l[[i+1]]=e];
Export["50SamplesNEW-"<>ToString[n]<>".txt",l,"table"]]
```

Figure 6-1: Monte Carlo sampling code.

### 6.2.2 Particle size distribution of real case

As discussed in Section 2.2, the size distribution of biomass particles could be measured in various ways. This section will introduce another particle size distribution sampling method. The size distribution of grounded biomass particles was the cumulative distribution which was studied by Tannous et al. [213]. They screened the 1.6mm size particles of grounded wood chips and chose the particle size distribution based on the particle number instead of the distributed volume. The sizes of sieved particles were 45, 63, 74, 88, 125, 150, 210, 300, 400, 600, 800, 1000, 1410 and 1680μm. The size distribution of these particles was shown in Figure 6-2 (retained fraction).

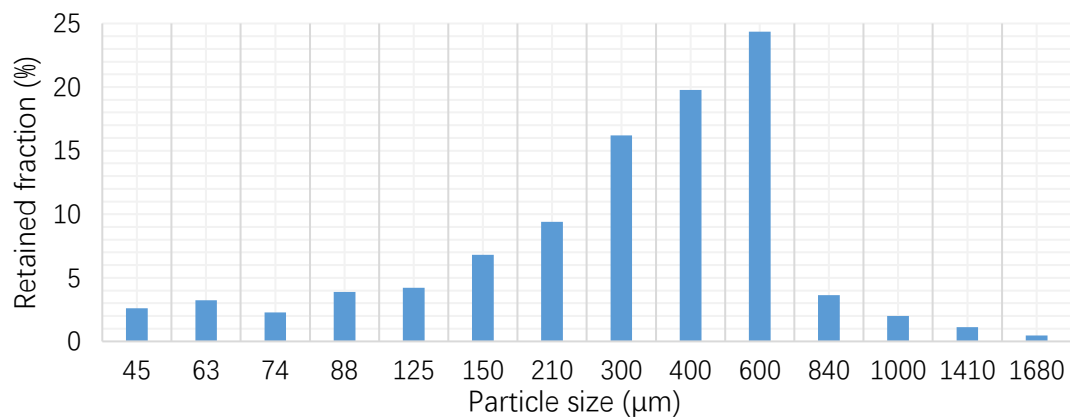


Figure 6-2: Size distribution of ground biomass particles from Douglas fir wood [213].

In order to obtain 50 samples, the retained fraction data was transformed to the cumulative fraction. The cumulative fraction graph was digitized by the *Engauge* graph digitizer software. Engauge is a software which allows the user to import an image of a graph, defining position of three main co-ordinate points, typically (0, 0), (0,  $y_{max}$ ) and ( $x_{max}$ , 0), then, the position of the curve on the graph can be marked and transferred to digital data. The obtained digital data can

be imported to Microsoft Excel. Once the obtained data was imported into Excel, the cumulative frequency data was used to calculate the frequency of particles in bins. The frequency in each bin was multiplied by 50 to determine how many particles should be sampled in each bin. A random number generator was then used to generate random particle sizes for the number of particles within each bin. Table 6-1 lists the sieved particle sizes, corresponded retained fraction and frequency bins.

*Table 6-1: Sieved particle sizes, corresponded retained fraction, and cumulative fraction.*

| <b>x (μm)</b> | <b>Retained fraction (%)</b> | <b>Cumulative fraction (%)</b> | <b>Frequency bins (%)</b> |
|---------------|------------------------------|--------------------------------|---------------------------|
| 45            | 2.61035                      | 2.61035                        | 0<2.61035                 |
| 63            | 3.24446                      | 5.85481                        | 2.61035<5.85481           |
| 74            | 2.26702                      | 8.12183                        | 5.85481<8.12183           |
| 88            | 3.88517                      | 12.007                         | 8.12183<12.007            |
| 125           | 4.2219                       | 16.2289                        | 12.007<16.2289            |
| 150           | 6.8043                       | 23.0332                        | 16.2289<23.0332           |
| 210           | 9.4081                       | 32.4413                        | 23.0332<32.4413           |
| 300           | 16.2108                      | 48.6521                        | 32.4413<48.6521           |
| 400           | 19.7789                      | 68.431                         | 48.6521<68.431            |
| 600           | 24.3441                      | 92.7751                        | 68.431<92.7751            |
| 840           | 3.647                        | 96.4221                        | 92.7751<96.4221           |
| 1000          | 1.9992                       | 98.4213                        | 96.4221<98.4213           |
| 1410          | 1.1171                       | 99.5384                        | 98.4213<99.5384           |
| 1680          | 0.4616                       | 100                            | 99.5384<100               |

## 6.3 Single particle model

### 6.3.1 Model description – spherical particle

This model aims to predict the heating-up behaviour of biomass particles pyrolysis and investigate the effect of particle size distribution and heating up temperature. The particle model developed in this research is simulated in Mathematica, using finite volume approach to describe the single particle. The size distribution of 50 particles is generated by Monte Carlo method. Biomass particles are heated up during thermochemical conversion process. The moisture content within the biomass particle vapours rapidly. Current model is simplified as spherical model with single dimension, which is easy to be solved by finite volume method. The shrinkage and the porosity are considered in the model.

The pyrolysis model is constructed under the following simplifications:

- One-dimensional spherical model;
- Ignoring the external heat transfer, only the internal heat conduction considered;
- Ash content within the particle is ignored;
- Thermal conductivity is considered as constant value;

All the particles are at ambient condition (273K, 1 atm) initially, then, heating up to 773K, 873K and 973K, separately. The difference between the isothermal model and the non-isothermal model has been discussed in Section 5.3.1. For isothermal model,  $T_p$  is the single temperature, which is same as the environment temperature (773K, 873K and 973K). Many kinetic models have been proposed to describe biomass pyrolysis kinetics.

The single first order reaction (SFOR) model has been used widely due to its simplicity, however, it is an empirical model limited to a single reaction with a single activation energy [214]. Currently, the state-of-the-art model applied to describe the thermal decomposition kinetics of solid fuels is the distributed activation energy model (DAEM) [215-219]. It has been used to analyse the thermal decomposition kinetics of solid fuels, including biomass and its lignocellulosic components, coal, oil shale, waste plastics, and polymer etc. [219]. The model assumes that biomass pyrolysis takes a large number of independent parallel first-order or  $n$ th-order reactions with their own activation energies reflecting variations in the bond strengths of biomass species [215] and that the difference in activation energy can be described by a continuous distribution function (e.g., Gaussian, Logistic, Weibull distribution functions) [194,

220].

In this study, three different kinetic models for biomass pyrolysis are considered: (1) non-isothermal model with DAEM; (2) Non-isothermal model with Arrhenius model; (3) Isothermal model. The numerical calculations are carried out in the Wolfram Mathematica software system. The finite volume approach is used to solve the energy conservation equation relating the intra-particle heat transfer. Finite volume approach has two major advantages: (a) The flux (e.g. mass, momentum, energy) entering a given volume is identical to that leaving the adjacent volume, these methods are conservative; (b) it is easily formulated to allow for unstructured meshes to approximate complex geometries [221].

Initial properties of biomass particles are shown in Table 6-2. The property of char formation is determined by the volatile production rate. Thus, the initial density of carbon is seen as zero.

Table 6-2: Proximate analysis and the ultimate analysis of the biomass material.

| Proximate analysis |                   |                   |                   |                   |
|--------------------|-------------------|-------------------|-------------------|-------------------|
| Moisture           | Volatile          | Fixed carbon      | Ash               |                   |
| 8.17 wt.%          | 79.22 wt.%        | 10.59 wt.%        | 2.02 wt.%         |                   |
| Ultimate analysis  |                   |                   |                   |                   |
| C <sup>(db)</sup>  | H <sup>(db)</sup> | O <sup>(db)</sup> | N <sup>(db)</sup> | S <sup>(db)</sup> |
| 49.51 wt.%         | 5.94 wt.%         | 41.89 wt.%        | 0.30 wt.%         | 0.16 wt.%         |

### 6.3.2 Mass and energy conservation during pyrolysis process

The pyrolysis process only considered the heating-up, drying and devolatilization process. The governing equations of the mathematical model are consisted of the conservation of mass and energy. The ash of biomass particle is assumed to be constant during pyrolysis process. This model is developed based on the research of Li et al. [158], which predicts the combustion behaviour of woody biomass under high-temperature condition. They used the Palm Kernel Shell in the experiment to validate their simulation. The conversion equations are given by the mass evolution of dry biomass (Eq. 6-3), moisture content (Eq. 6-4), volatile (Eq. 6-5) and char (Eq. 6-6). In the devolatilization process, the reaction form is considered as: Biomass → volatiles + char. Thus, the evolution of volatile and char content can be given by the fraction of column.

$$\frac{\partial m_B}{\partial t} = -k_{devo} m_B \quad (6-3)$$

$$\frac{\partial m_{moi}}{\partial t} = -k_{dry} m_{moi} \quad (6-4)$$

$$m_v = v_{vola}(m_{B0} - m_B) \quad (6-5)$$

$$m_c = v_{char}(m_{B0} - m_B) \quad (6-6)$$

where  $m_B$ ,  $m_{moi}$ ,  $m_v$ , and  $m_c$  are the mass of the dry biomass, moisture, volatile and char. The superscript 0 means the initial value of each column. At  $t=0$ ,  $m_{B0} = \rho_B V_{P0}(1 - \varphi_0)$ , the  $\varphi_0$  is the initial porosity of the particle. The conversion rate is assumed as the first order Arrhenius equation. The energy conservation of the solid particles is expressed by considering the heat conduction, radiation, and heat release during the conversion (Section 5.3.1). Table 6-3 lists the properties and kinetic data used in the simulation.

Table 6-3: Properties and kinetic data.

|                   |                                 |                                  |                                  |            |
|-------------------|---------------------------------|----------------------------------|----------------------------------|------------|
| $\rho_B$          | Density                         | 700                              | $\text{kg m}^{-3}$               | [202]      |
| $X_{M0}$          | Moisture content (M)            | 8.17                             | wt. %                            |            |
| $X_{V0}$          | Volatile matter (VM)            | 79.22                            | wt. %                            |            |
| $X_{C0}$          | Fixed carbon (FC)               | 10.59                            | wt. %                            |            |
| $X_A$             | Ash                             | 2.020                            | wt. %                            |            |
| $v_{vola}$        | $VM/(1 - M)$                    | 0.862                            | -                                |            |
| $v_{char}$        | $FC/(1 - M)$                    | 0.115                            | -                                |            |
| $C_{p(B)}$        | Heat Capacity of biomass        | $1112 + 4.85 \times (T_p - 273)$ | $\text{J kg}^{-1} \text{K}^{-1}$ | [204]      |
| $C_{p(V)}$        | Heat Capacity of volatile       | $1050 + 0.18 \times (T_p - 273)$ | $\text{J kg}^{-1} \text{K}^{-1}$ |            |
| $C_{p(C)}$        | Heat Capacity of char           | $1390 + 0.36 \times (T_p - 273)$ | $\text{J kg}^{-1} \text{K}^{-1}$ | [205]      |
| $C_{p(M)}$        | Heat Capacity of moisture       | 4280                             | $\text{J kg}^{-1} \text{K}^{-1}$ |            |
| A                 | Pre-exponential factor          | $1.1291 \times 10^{16}$          | $\text{s}^{-1}$                  |            |
| E                 | Activation energy               | 189.15                           | $\text{kJ mol}^{-1}$             |            |
| A                 | Pre-exponential factor          | $6 \times 10^5$                  | $\text{s}^{-1}$                  | [222]      |
| E                 | Activation energy               | 48.22                            | $\text{kJ mol}^{-1}$             | [222]      |
| $k_M$             | Thermal conductivity (moisture) | 0.653                            | $\text{W m}^{-1} \text{K}^{-1}$  | [129, 206] |
| $k_V$             | Thermal conductivity (volatile) | 0.2                              | $\text{W m}^{-1} \text{K}^{-1}$  | [129]      |
| $k_C$             | Thermal conductivity (char)     | 0.15                             | $\text{W m}^{-1} \text{K}^{-1}$  | [129]      |
| $k_A$             | Thermal conductivity (ash)      | 0.1                              | $\text{W m}^{-1} \text{K}^{-1}$  | [129]      |
| $k_B$             | Thermal conductivity (biomass)  | 0.21                             | $\text{W m}^{-1} \text{K}^{-1}$  | [207]      |
| $\Delta H_m$      | Reaction heat (moisture)        | -270                             | $\text{kJ kg}^{-1}$              | [91, 208]  |
| $\Delta H_v$      | Reaction heat (volatile)        | -418                             | $\text{kJ kg}^{-1}$              | [91]       |
| $\Delta H_c$      | Reaction heat (char)            | -418                             | $\text{kJ kg}^{-1}$              | [91]       |
| $\omega$          | Pore emissivity                 | 1                                | -                                | [206]      |
| $l_{\text{pore}}$ | Pore size                       | $5 \times 10^{-5}$               | m                                | [129]      |
| $\sigma$          | Stefan-Boltzmann constant       | $5.67 \times 10^{-8}$            | $\text{W m}^{-2} \text{K}^{-4}$  | [209]      |

### 6.3.3 Intraparticle heat transfer model

For non-isothermal model, the temperature distribution calculated by volume averaging method and the temperature changes with the position at each time step. Figure 6-3 gives a scheme of the intra-particle heat transfer approach. It is assumed that the biomass particle exposes to the environment temperature at  $t=0$ .

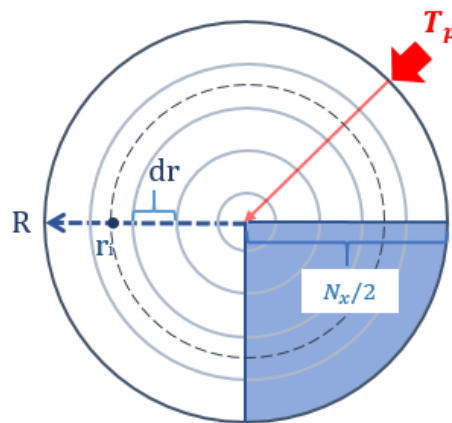


Figure 6-3: Schematic of intra-particle heat transfer.

The  $N_x$  is the division number of the finite volume approach, where  $N_x = 100$ . The estimation of calculating average particle temperature is:

$$T_{t+\Delta t} = \frac{\sum_{i=1}^{N_x/2} 2\pi r_i \times \Delta r \times T_t}{\pi R^2} \quad (6-7)$$

```
T[[n+1]] =
Total[Table[2*Pi*P1/2/(Nx*0.5)*P1/2*(50-m+0.5)/50*
G2[[m]]/(Pi*(P1/2)^2), {m, 1, Nx/2}]];
```

Figure 6-4: Mathematica code of average volume temperature.

Figure 6-4 gives the Mathematica code of the average temperature calculation.

$T_p$  is the heating temperature of the biomass particle. For isothermal model, we assume  $T_p$  is simple temperature same as temperature of exposure environment, e.g. 773K. For non-

isothermal model,  $T_p$  uses volume averaging method cross the particle every time step.

### 6.3.4 DAEM model

The DAEM equation can be derived based on the following assumptions: (1) the thermal decomposition of biomass involves a large number of independent and parallel first order reactions; (2) each reaction has its own activation energy and all reactions share the same frequency factor; (3) the activation energies of all reactions can be described by a continuous distribution [215, 223-225]. With these assumptions, the general form of the DAEM equation can be obtained [215]:

$$\alpha(t) = \int_0^{+\infty} \left\{ 1 - \exp \left[ - \int_0^t A \exp \left( - \frac{E}{RT} \right) dt \right] \right\} f(E) dE \quad (6-8)$$

$$\frac{d\alpha}{dt}(t) = \int_0^{+\infty} A \exp \left[ - \frac{E}{RT} - \int_0^t A \exp \left( - \frac{E}{RT} \right) dt \right] f(E) dE \quad (6-9)$$

where  $\alpha$  is conversion degree (dimensionless),  $A$  is the frequency factor ( $s^{-1}$ ),  $E$  is the activation energy ( $J mol^{-1}$ ),  $t$  is the time (s),  $T$  is the temperature (K), and  $f(E)$  is the activation energy distribution ( $mol J^{-1}$ ). The Logistic activation energy distribution is considered in this work because of its advantages in the representation of the kinetics of lignocellulosic biomass pyrolysis [225].

$$f(E) = \frac{\pi}{\sqrt{3}\sigma} \frac{\exp \left[ - \frac{\pi(E-\mu)}{\sqrt{3}\sigma} \right]}{\left\{ 1 + \exp \left[ - \frac{\pi(E-\mu)}{\sqrt{3}\sigma} \right] \right\}^2} \quad (6-10)$$

where  $\mu$  is the mean value ( $J mol^{-1}$ ) and  $\sigma$  is the standard deviation ( $J mol^{-1}$ ) of the activation energy distribution.

For coupling DAEM and PBM, the mass transfer of biomass and conversion rate can be obtained:

$$\alpha = 1 - \frac{\rho}{\rho_0} \quad (6-11)$$

$$\frac{d\alpha}{dt}(t) = \frac{d \left( 1 - \frac{\rho}{\rho_0} \right)}{dt}(t) = - \frac{1}{\rho_0} \frac{d\rho}{dt}(t) \quad (6-12)$$

$$\frac{d\rho}{dt}(t) = -\rho_0 \int_0^{+\infty} A \exp \left[ - \frac{E}{RT} - \int_0^t A \exp \left( - \frac{E}{RT} \right) dt \right] f(E) dE \quad (6-13)$$

where  $\rho$  is the density of biomass particle at time  $t$ , and  $\rho_0$  is the initial density of biomass

particle.

### 6.3.5 Results and discussion

#### 6.3.5.1 Population balance model

Figure 6-5 shows particle size sampling from a normal distribution with mean particle size,  $\mu_p = 1000 \mu\text{m}$  and standard deviation,  $\sigma_p = 200 \mu\text{m}$ . The lines represent the continuous probability of selecting a particle of a given size. The discrete 50 points represent the particles which were randomly selected from the distribution using the Monte Carlo method.

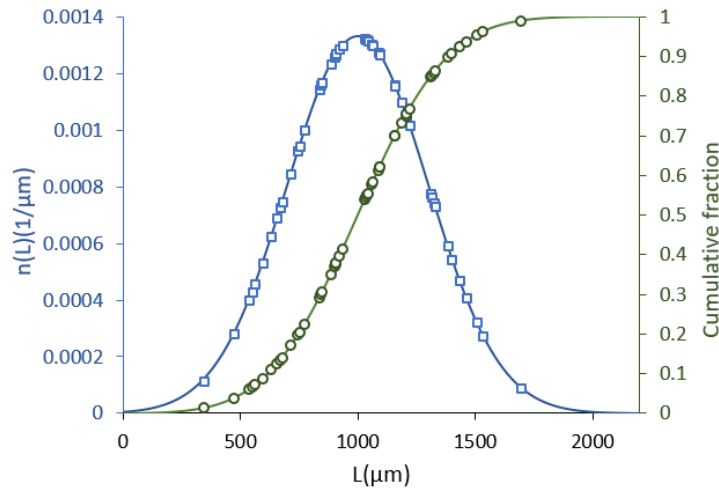


Figure 6-5: Particle size sampling from a normal distribution ( $\mu_p = 1000 \mu\text{m}$ ,  $\sigma_p = 200$ ).

The Biot number (defined by Eq. 5-3) is a dimensionless number which describes the ratio of internal heat resistance of a body (which occurs through conduction) to the external heat resistance of a body (which occurs through convection).

$$Bi = \frac{h L_p}{k'} \quad (6-14)$$

where  $h$  is the external heat transfer co-efficient,  $k'$  is the thermal conductivity, and  $L_p$  is the characteristic length of the particle. As the heat transfer coefficient has not been considered in this model, assumed values for the heat transfer coefficient and thermal conductivity have been used in calculating the Biot number. The thermal properties were assumed as:  $h = 650 \text{ W/m}^2 \text{ K}$  and  $k' = 0.25 \text{ W/m K}$  [226]. Figure 6-6 shows the relationship between Biot number and particle size to be able to convert between the two values if necessary. It should be noted that, in a real process, the relationship between the Biot number and particle size is not linear as the heat transfer coefficient of biomass is affected by particle size.



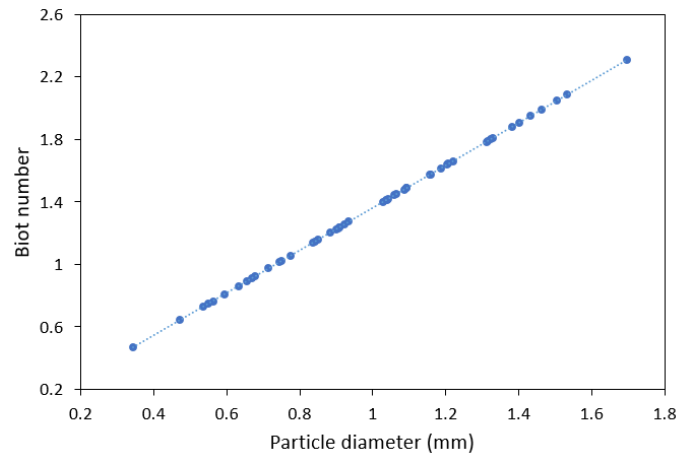
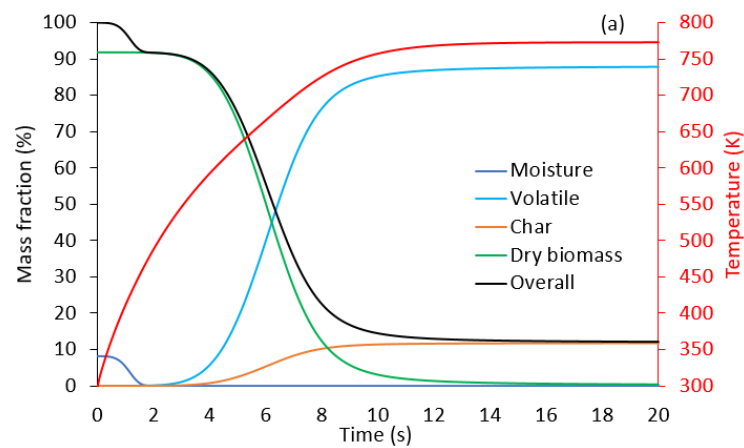


Figure 6-6: Biot number against particle diameter.

### 6.3.5.2 Mass loss rates

It has been discussed that the heat, mass and kinetic transfer processes occur simultaneously during the pyrolysis until the particle dried completely [161]. As the increasing of the particle temperature, the drying and devolatilisation rates increases as well. Once the biomass particle exposed to the environmental temperature, the particle is heated up immediately and the surface temperature is raised due to the intra-particle convection and the radiation form the furnace wall [158]. Figure 6-7 presents the mass loss rate predicted from two different model.



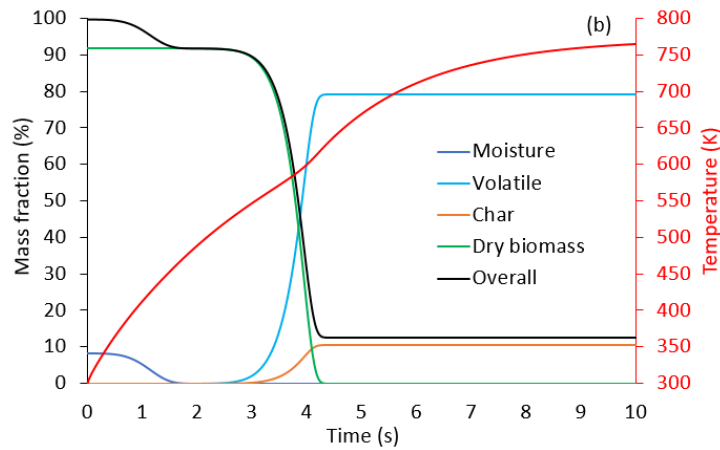


Figure 6-7: Mass loss rate predicted from two different models ( $d=1.03\text{mm}$ ,  $773\text{K}$ ): (a) Non-isothermal model with DAEM; (b) Non-isothermal model without DAEM.

From the perspective of mathematical modelling, the heat, mass and kinetic transfer phenomenon occur simultaneously in the thermochemical conversion process of lignocellulosic biomass [161]. Once the particle exposed to the heating source, the biomass particle is heated up and the temperature transferred from the surface. In the heating process, the biomass particle is decomposed while producing volatiles and char, at the same time, the moisture content within the particle is vaporized in a short time period [227]. The mass loss rate of the pyrolysis stage strongly depends on the temperature distribution inside the biomass particles [161].

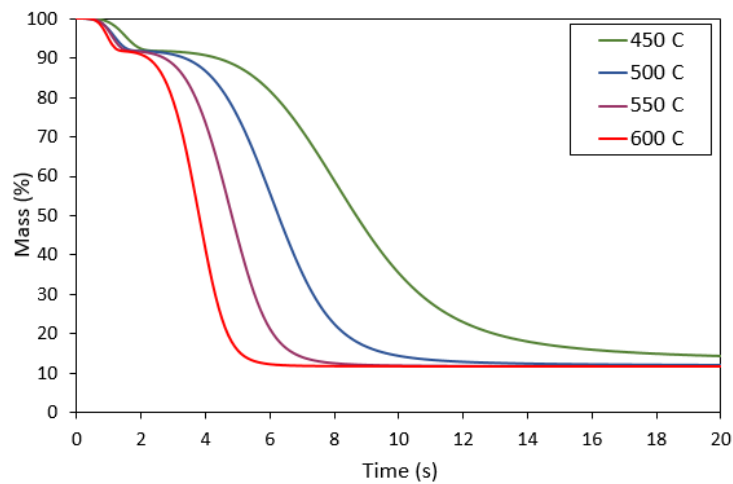


Figure 6-8: Influence of temperature on mass loss rate predicted from non-isothermal model with DAEM ( $1.03\text{mm}$ ).

Figure 6-8 presents the individual mass change prediction of  $1.03\text{mm}$  spherical biomass particle, which refers the progress of drying and devolatilization known as the two main stages occurred during biomass fast pyrolysis. Therefore, the rate of mass change reflects the accuracy and capture ability of the different models. The drying process terminates quickly less than 2s in the numerical prediction of both non-isothermal models and predicted high devolatilization rate of

non-isothermal model with DEAM appears at 4~8 seconds, which is relatively delayed compared to that of non-isothermal model with DEAM. DAEM predicted the mass loss rate in function of environment temperature (450~600 °C) is shown in Figure 6-9.

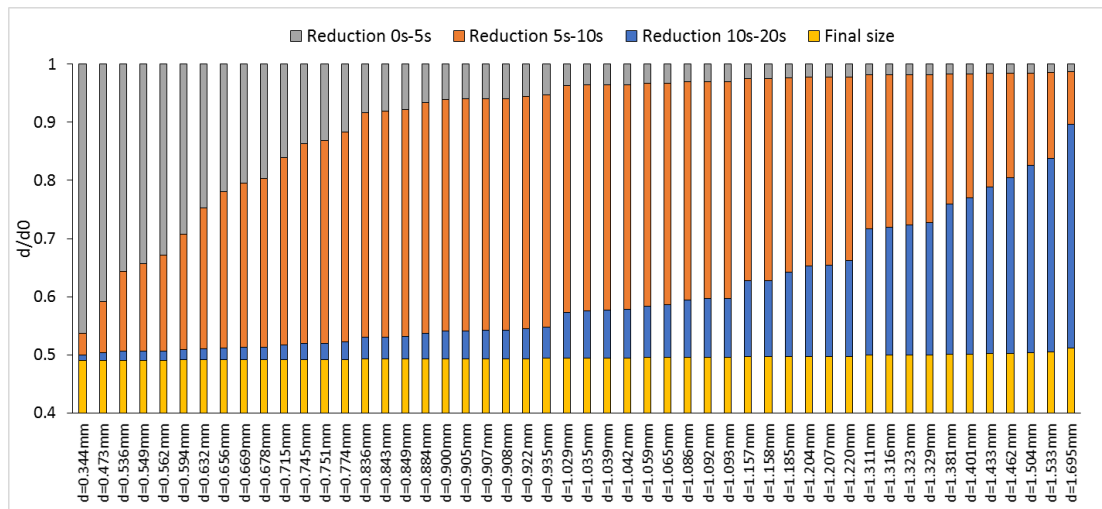
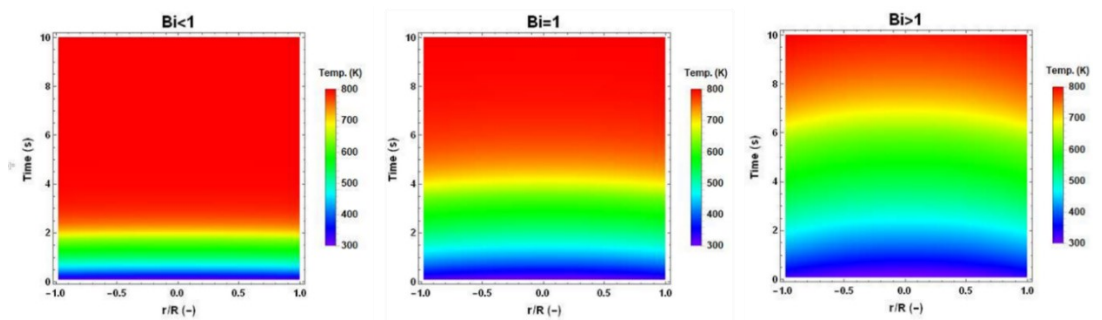


Figure 6-9: the extent of size reduction at different time periods for whole particle population (non-isothermal model with DAEM).

### 6.3.5.3 Temperature distribution

Figure 6-10 shows contour plot of radial temperature distribution over time at different Biot number. Fine particle with  $Bi < 1$  have achieved uniform temperature cross radial direction over the whole process. There is slight difference between core temperature and surface temperature of wood particle with  $Bi=1$ . At  $Bi > 1$ , the radial temperature distribution within particle is symmetrical and parabolic. The heating up time increases with particle size.



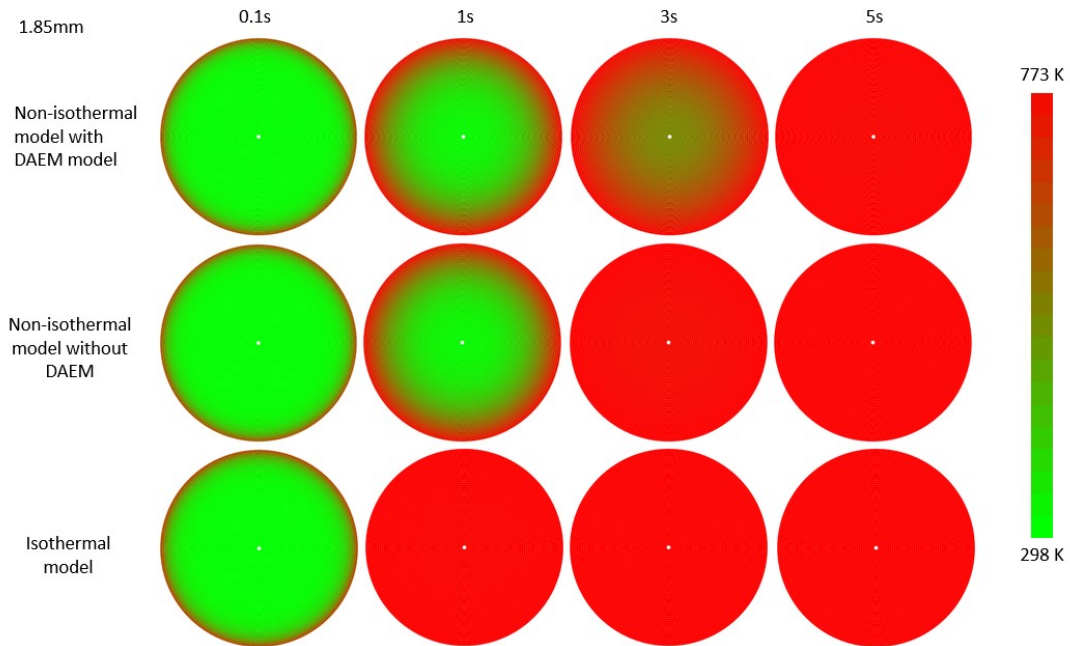


Figure 6-10: Contour plot of radial temperature distribution over time at different Biot number.

The temperature distribution graphs show that it seems that the isothermal model may over-predicted the temperature transfer efficiency. It is proved that the average temperature model calculates a lower temperature value than the surrounding temperature.

#### 6.3.5.4 Size reduction and porosity

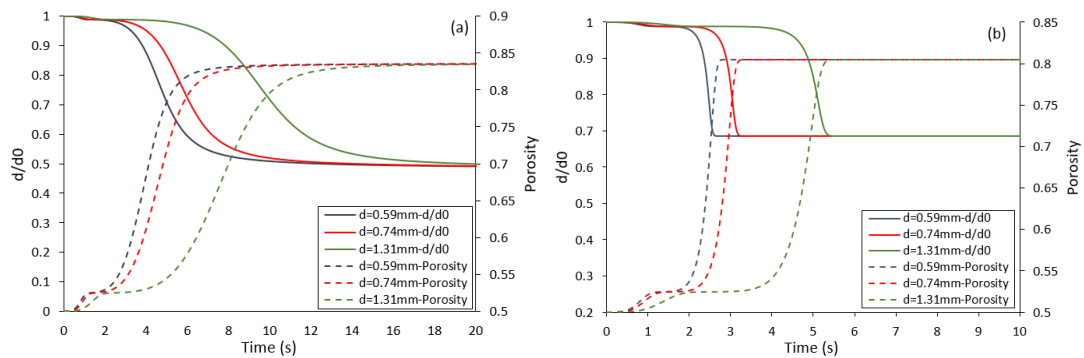


Figure 6-11: Particle diameter and porosity variation for different particles:  $d=0.59\text{mm}$  ( $Bi < 1$ ),  $d=0.74\text{mm}$  ( $Bi = 1$ ),  $d=1.31\text{mm}$  ( $Bi > 1$ ) at  $773\text{K}$ . (a) Non-isothermal with DAEM. (b) Non-isothermal model without DAEM.

The variation of the pore structure within particle might be another reason for the low mass loss rate when shrinkage is tiny. Figure 6-11 shows the porosity and size reduction over time under two different kinetic models, respectively. It could be observed that rapid increase of porosity synchronize with rapid decrease of the wood mass as the increase of pore size could benefit the releasing rate of gas and tar.

### 6.3.5.5 Temporal evolution of particle size distribution

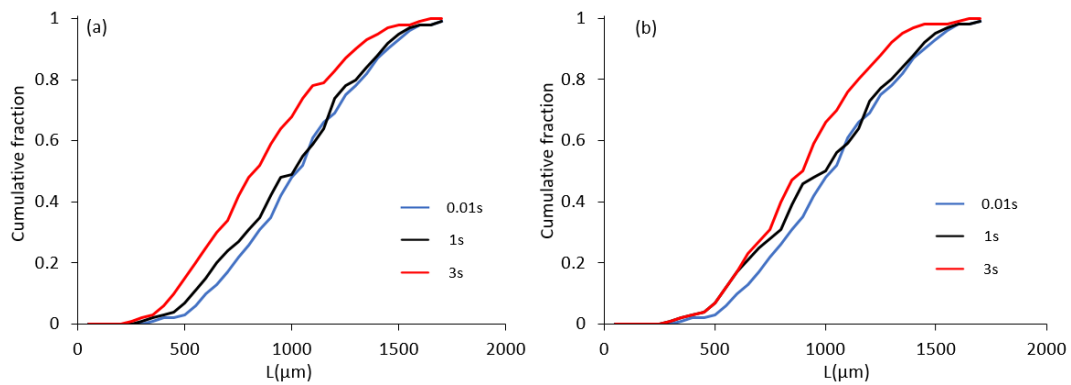


Figure 6-12: Temporal evolution of particle size distribution at 773K. (a) Non-isothermal with DAEM. (b) Non-isothermal model without DEAM.

Particle shrinkage of biomass leads to temporal evolution of particle size distribution, which is predicted and shown in Figure 6-12. The partially left shift of cumulative curve of population size distribution at 1 s in Figure 6-12 shows relatively smaller particles completed the decomposition and size reduction. The overall left shift of cumulative curve population size distribution at 3 s in Figure 6-12 demonstrates most particles completed the decomposition and size reduction.

### 6.3.5.6 Effect of surrounding temperature on centre temperature of particle

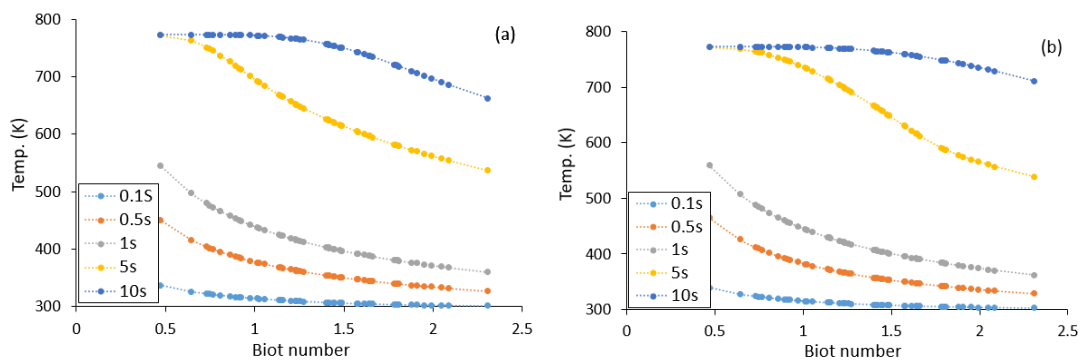


Figure 6-13: Temperature at centre of particle at pyrolysis temperature of 773K. (a) Non-isothermal with DAEM. (b) Non-isothermal model without DEAM.

Figure 6-13 shows the temperature of particle centre,  $T_c$ , for particle population (presented as Bi number) at different times. There is always a decrease in  $T_c$  with increasing particle size. At 1 s, the smallest particle ( $Bi = 0.47$ ) has achieved a temperature 545K, whilst  $T_c$  of the largest particle ( $Bi = 2.3$ ) is only at 360K. The initial heating rate of the smallest particle indicated rapid heating up occurring at fine particles in fast pyrolysis processes, which well agreed with the experimental observation. Furthermore, all particles with  $Bi < 1$  have achieved some extent

of increase in temperature after just 0.1 s, with  $T_c$  decreasing as Biot number increases up. At  $Bi > 1$ ,  $T_c$  has not increased significantly from its initial temperature, and does not appear to be affected by particle size above  $Bi > 1$ . This builds upon the idea that the critical Biot number is  $Bi = 1$  ([228], [229] and [86]), as above  $Bi = 1$ , there is evidence that the heat transfer resistance of the particle has prevented  $T_c$  from being significantly increased. After 10 s, we see that  $T_c$  of particles with a  $Bi$  up to 1.2 have achieved the temperature of the surroundings, 773K. Above  $Bi = 1.2$ , there is again a decline in  $T_c$  with increasing particle size. Figure 6-14 shows high pyrolysis temperature advantages heat transfer through the particle.

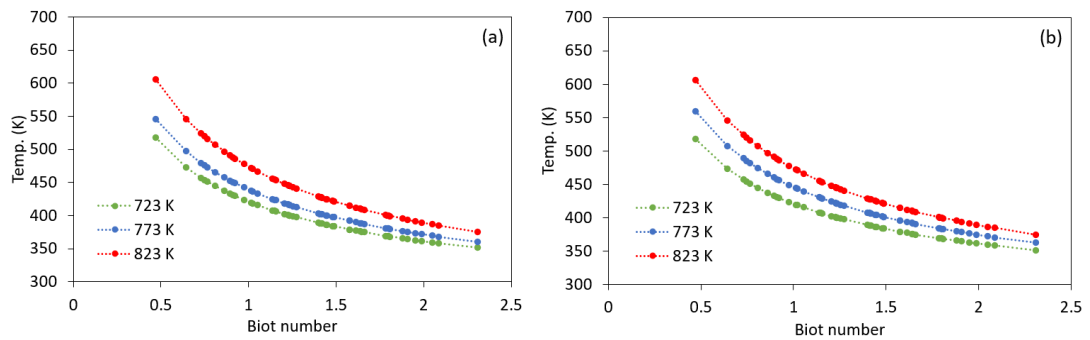


Figure 6-14: Effect of pyrolysis temperature on temperature of Centre of Particles after 1 Second. (a) Non-isothermal with DAEM. (b) Non-isothermal model.

### 6.3.5.7 Percentage of particles reach to set temperature

Figure 6-15 demonstrates the capability of PBM to predict the temporal percentage of particle population to complete heating up process. The PBM model enables proper particle size of biomass feedstock to be selected for satisfying the affirmatory resident time distribution of pre-installed reactor. In Figure 17 (a), the numerical prediction of pyrolysis at 723K indicates that only 38% of particles have undergone complete heating-up process after 10 s. It takes 17.2 s for all of the particles in the size distribution to complete heating-up process. At 823K, we see that a significantly higher proportion of the particles have achieved complete thermal transfer after 10s, around 98%.

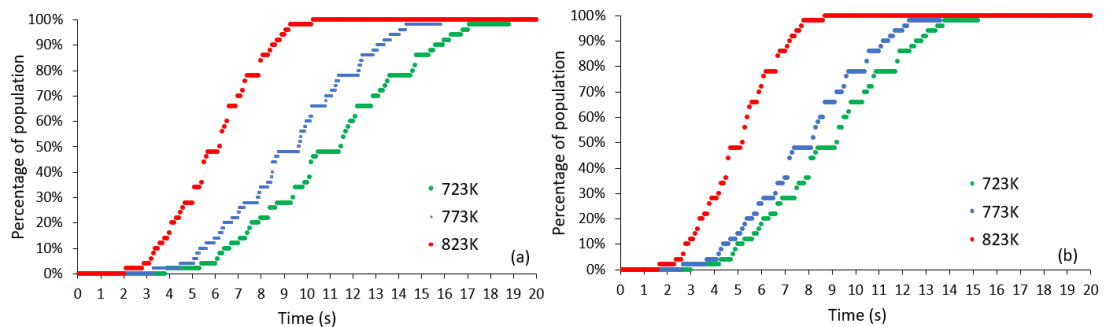


Figure 6-15: Percentage of PSD to complete heating up process predicted from different models under temperature. (a) Non-isothermal with DAEM. (b) Non-isothermal model.

### 6.3.5.8 Heating-up time of normal size distribution

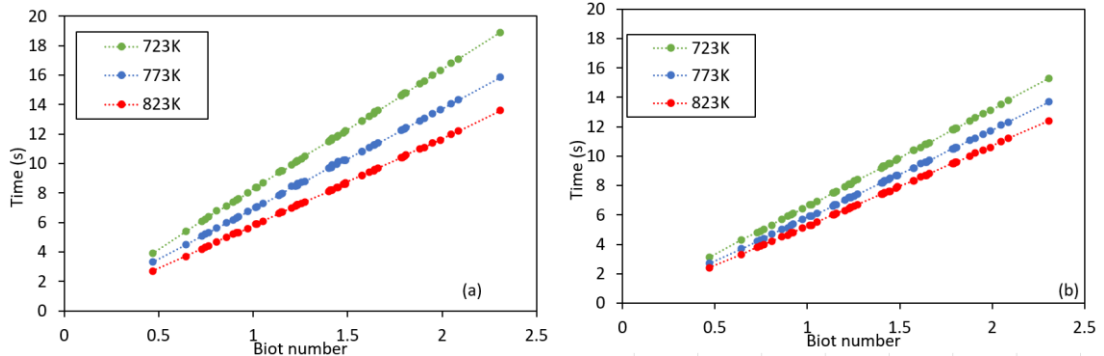


Figure 6-16: Heat up time under different surrounding temperature. (a) Non-isothermal with DAEM. (b) Non-isothermal model.

Figure 6-16 shows the dependence of heat-up time on the size of particle at different pyrolysis temperature of 723K~823K. As the particle diameter increases, so does the time taken for  $T_c$  to achieve surrounding temperature, which is in agreement with what has been reported in the literature [230]. For both non-isothermal kinetic models, the increase of exposure temperature accelerates heating up of biomass feedstock, especially for thermally thick particle.

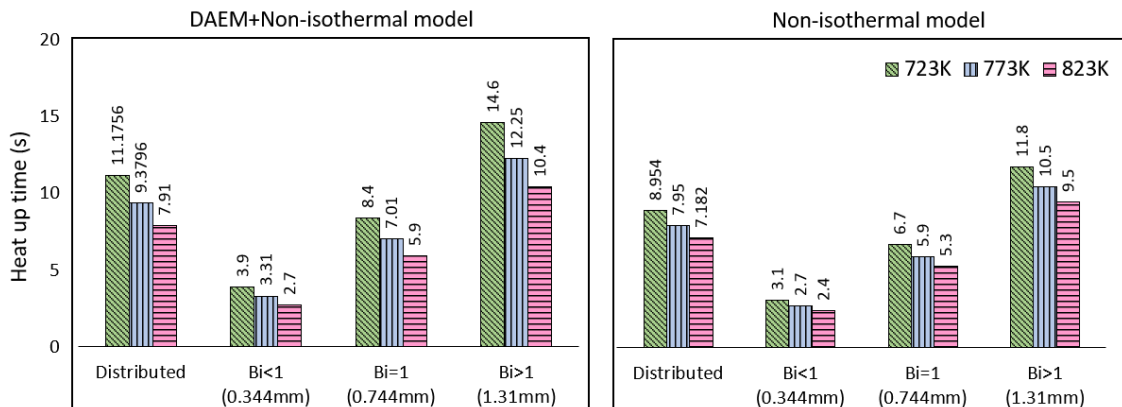


Figure 6-17: Comparison of heating up time prediction between single and distributed particle size using different kinetics models.

Figure 6-17 shows the comparison of heating-up time between single and distributed particle size using different kinetics models. The order of predicted heating up time is: Non-isothermal without DEAM < Non-isothermal with DEAM. The heating up time of normal size distribution is always larger compared to that of single size for all three models. For non-isothermal model with DEAM, the heat-up time for single size of 1mm in is found to be 11.1 and 9.0 s, respectively. This is in good agreement with the work of Wiggins, et al. [231], who found the time taken for the surface of a 1mm spherical particle to reach 773K to be 3 seconds. Figure



6-18 shows the comparison of heating-up time between single and distributed particle size under different surrounding temperatures.

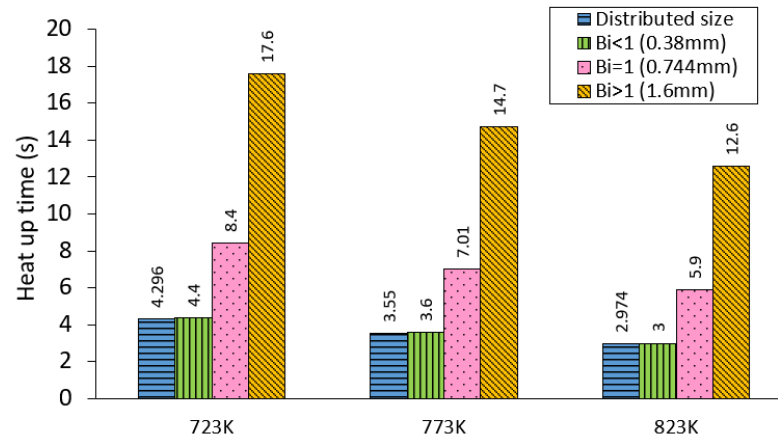


Figure 6-18: Comparison of heating up time prediction between single and distributed particle size under different temperature.

### 6.3.6 Validation and Conclusion

The developed model framework is firstly validated with a comparison of the numerical results (surface temperature, mass loss and size reduction) to corresponding experimental data obtained from pyrolysis of spherical wood particle [222]. The experiment was carried out by Huang et al. [222], utilising a fixed-bed reactor integrating a high-transparency quartz tube with an electrically heated furnace to study the pyrolysis behaviour of wood particle in spherical shape. The surface temperature of woody biomass in Figure 6-19 displays the comparison between the experimental data and the model predictions. It is clear that the trend of the numerical predictions (from non-isothermal model without DEAM and with DEAM model) are consistent with the experimental data at 150~400 s meanwhile a bit over-prediction can be observed before 150 s. The increase of surface temperature are predominantly controlled by boundary conditions, consisting of convective and radiative heat transfer from surrounding pyrolysis environment. The mass loss shown in Figure 6-20 demonstrates the pyrolysis characteristics, with the weight loss mainly happened at 150 to 250 s, corresponding to surface temperature at 700–750K. The numerical curve of mass loss largely fits the experimental data, with a slight over-prediction of decomposition speed.



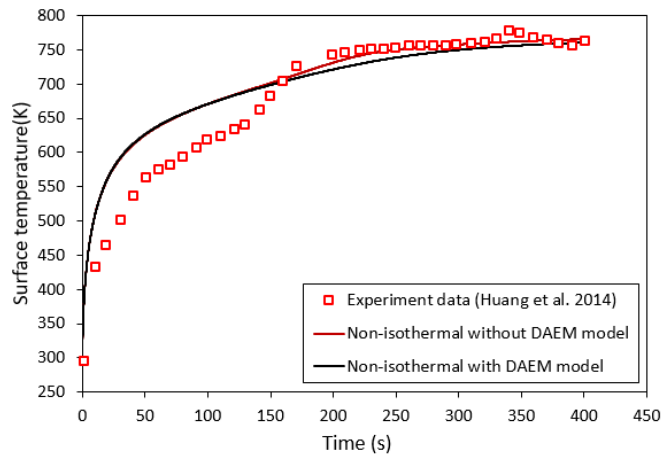


Figure 6-19: Particle surface temperature. Experiment data obtained from [222]. ( $d=20\text{mm}$ ,  $773\text{K}$ ).

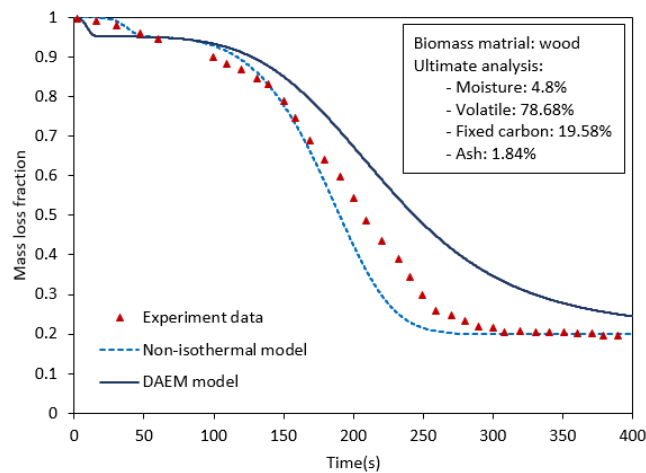


Figure 6-20: Residue mass fraction ( $d=20\text{mm}$ ,  $773\text{K}$ ). Experimental data from Huang et al. [222]. Ultimate analysis data obtained from Sadhukhan et al. [134].

Shrinkage percentage is a ratio of instantaneous diameter to initial diameter of the wood sphere. There is no uniform standard of shrinkage model in the literatures. Contradictive experimental phenomenon was also found that such as, wood pellets shrinkage increases with temperature in the range  $300\text{--}1000\text{ }^{\circ}\text{C}$  [232], but on another side, wood spheres shrinkage decreases with temperature in the range of  $673\text{ to }973\text{K}$  [222]. Two shrinkage models were incorporated into the model framework to simulate the size reduction of wood sphere with  $20\text{mm}$  during pyrolysis at  $773\text{K}$ . As shown in Figure 6-21, the shrinkage model developed by Huang et al. [222] using a mathematical function based on Boltzmann fitting, agrees the experimental data fairly well, as the case specific parameters are directly regressed from investigational data size reduction. The shrinkage model developed by Yang et al. [129] are based on mass balance, which could directly apply to this validation with successful prediction of final size, but the accuracy of temporal size reduction is less than the shrinkage model of Huang et al.

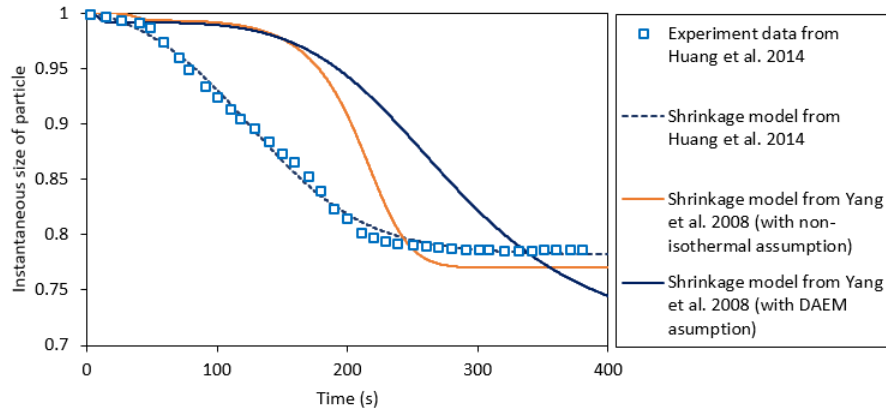


Figure 6-21: Size reduction comparison. Shrinkage model from: Huang et al. [222] and Yang et al. [129]

The developed model successfully predicted the conversion performance of biomass feedstock with a size distribution. The PBM is used to present biomass particle population of normal size distribution and irregular size distribution. The finite volume approach is used to develop the model. Three cases are developed to make the comparison in terms of the size reduction, porosity change and the heating-up time during pyrolysis process of biomass particles. The heat-up time of the particle has been calculated as the time taken for the surface of the particle to reach the set temperature. In literature, the heat-up time is often based on the volume-averaged temperature of the particle, however due to the number of particles sampled in these models, it is not possible to do this with the computer software easily.

## Chapter 7. Conclusion and Recommendation

### 7.1 Conclusions

This thesis experimentally and modelling studied the pyrolysis behaviour of herb residues in terms of kinetic analysis and particle modelling approach. The experiment and modelling methods and the results were discussed in Chapter 3 to Chapter 6. This work has improved the investigation of pyrolysis behaviours of herb residues, in terms of the thermogravimetric characteristics and kinetic analysis and mathematical modelling methods. The kinetic analysis method has been improved compared with the current research method, using an updated Dn model to determine the kinetic parameters (Section 3.4). The obtained results of kinetic parameters of herb residues have been successfully used in the particle model. The three-dimensional single large cylindrical particle model was developed to study the slow pyrolysis characteristics. For single particles with a size distribution (Chapter 6), the PBM-DEAM coupled model is first developed to investigate the pyrolysis behaviour of biomass. The developed model has been well validated with the experiment data.

The thermogravimetric characteristics and kinetics of CHR and catalytic CHR were investigated. The TG and DTG curves illustrated the catalysts make the mass loss curve to the lower temperature range compared with the raw material. The  $K_2CO_3$  catalysts significantly promote the pyrolysis reaction of the hemicellulose and cellulose of CHR samples at the main devolatilization stage (over 80.0% mass loss). The validation results showed that the model-free Starink method and the master-plot method were successfully used in calculating the kinetic parameters of CHR and catalytic CHR. The model results using the optimized parameters were highly consistent with experimental TG data at all the four heating rates for the raw CHR, however. There is small discrepancy for that of the CHR samples with  $K_2CO_3$ , which caused by the presence of multi-step complex decomposition reactions at high temperatures.

The formation and evolution of N-containing groups of char product obtained from biomass pyrolysis were investigated in Chapter 4. The CHR and BS were selected to carry out the pyrolysis process. As the increasing pyrolysis temperature, the existing form of N-containing functionalities transformed from protein-N to pyridinic-N and pyrrolic-N. The catalyst increased the efficiency of this transformation. The N content in the pyrolysis products of biomass related to the release of N pollutants. To better studying the nitrogen reduction method, the research on the release characteristics N-containing gas ( $NH_3$ ,  $HNCO$ ,  $HCN$  and  $NO_x$ ) should be developed in further study.

The model developed in Mathematica is able to predict the temperature distribution within a single particle and the heat transfer character during biomass pyrolysis. The finite volume approach was used to develop the single particle model. Chapter 5 is the single large pellet model of CHR pyrolysis and Chapter 6 is the particle model with a size distribution. The PBM-DAEM coupled model was firstly developed to predict the pyrolysis of biomass. The isothermal kinetics only works well in thermally thin particle since the intra-particle temperature gradient was ignored. The non-isothermal kinetics was suitable for the thermally thick particles, the intra-particle heat transfer was considered in this model. However, the model numerically simply presents biomass decomposition with single reaction and single activation energy, which is unable to reveal the true mechanism during biomass fast pyrolysis process. The DEAM kinetics considered a large number of independent parallel first-order or  $n$ th-order reactions with their own activation energies. Thus, the non-isothermal with DAEM model could successfully describe the intra-particle heat transfer and the decomposition mechanism. The predicted heating times for hot thick particles are: Isothermal model < non-isothermal without DEAM < non-isothermal model with DEAM, since non-isothermal models (with and without DEAM) depend primarily on the temperature distribution within the particle. The developed model successfully predicts the conversion performance of biomass feedstocks with a size

distribution. The particle size of biomass feedstock has a significant impact on heating up time. The beneficial results will support the design of the pyrolysis reactor and the determination of the optimal feedstock particle size.

## 7.2 Future work plan

The work accomplished in this PhD research has contributed to the reaction mechanisms and characteristics of biomass pyrolysis. The calculation method of kinetic parameters was validated in this research. The heat and mass transfer behaviour within the single particle was predicted using the numerical model. The suggestions below describe the future work based on this research:

- The biomass material has the ability of nitrogen fixation during growth. The N content will be released during the thermochemical conversion process which will lead to the N pollutants. Chapter 4 only studied the N contents in char product of pyrolysis. The future work should focus on the N-containing species in gas phase, which related to the NO<sub>x</sub> precursors formation. Different operation conditions and varying catalyst loading should be investigated in the further study, such as the heating rate and reaction type.
- The cylinder biomass pellet model was validated with the experimental results. However, the simulation results cannot be fully consistent with the experiment. Thus, to obtain more accurate results, the future model should consider the effect of the pyrolysis temperature on the kinetic parameters (low temperature kinetic and high temperature kinetic). The effect of shrinkage should be considered in this model. Also, the effect of particle size, aspect ratio and heating up rate can be considered in the future simulation.
- The PBM-DAEM coupled particle model was successfully used to describe the biomass pyrolysis behaviour. This model framework should be further developed to enhance the real particle morphology. The biomass particles exhibit irregular shapes with different surface area to volume ratios. This will lead to different thermal conversion performance of different particles. Thus, the more detailed particle geometry could be considered in the further study.

## References

- [1] M. Tripathi, J. N. Sahu, and P. Ganesan, "Effect of process parameters on production of biochar from biomass waste through pyrolysis : A review," *Renewable and Sustainable Energy Reviews*, vol. 55, pp. 467-481, 2016.
- [2] L. Capuano, "International Energy Outlook 2018 (IEO2018)," 2018, vol. 2018 Available: [www.eia.gov](http://www.eia.gov).

- [3] C. C. Enweremadu and M. M. Mbarawa, "Technical aspects of production and analysis of biodiesel from used cooking oil-A review," *Renewable and Sustainable Energy Reviews*, vol. 13, no. 9, pp. 2205-2224, 2009.
- [4] H. Lu, W. Robert, G. Peirce, B. Ripa, and L. L. Baxter, "Comprehensive study of biomass particle combustion," *Energy and Fuels*, vol. 22, no. 4, pp. 2826-2839, 2008.
- [5] O. Ellabban, H. Abu-Rub, and F. Blaabjerg, "Renewable energy resources: Current status, future prospects and their enabling technology," *Renewable and Sustainable Energy Reviews*, vol. 39, pp. 748-764, 2014.
- [6] P. McKendry, "Energy production from biomass (part 2): Conversion technologies," *Bioresource Technology*, vol. 83, no. 1, pp. 47-54, 2002.
- [7] D. L. Klass, *Biomass for Renewable Energy, Fuels, and Chemicals*. Elsevier Science, 1998.
- [8] A. V. Bridgwater and G. V. C. Peacocke, "Fast pyrolysis processes for biomass," *Renewable and sustainable energy reviews*, vol. 4, no. 1, pp. 1-73, 2000.
- [9] A. V. Bridgwater, "Review of fast pyrolysis of biomass and product upgrading," *Biomass and Bioenergy*, vol. 38, pp. 68-94, 2012.
- [10] T. Kan, V. Strezov, and T. J. Evans, "Lignocellulosic biomass pyrolysis : A review of product properties and effects of pyrolysis parameters," *Renewable and Sustainable Energy Reviews*, vol. 57, pp. 1126-1140, 2016.
- [11] Q. Lu, W. Z. Li, and X. F. Zhu, "Overview of fuel properties of biomass fast pyrolysis oils," *Energy Conversion and Management*, vol. 50, no. 5, pp. 1376-1383, 2009.
- [12] Y. Vanwonterghem, "Bio-oil production by biomass fast pyrolysis," University of Gent, 2012.
- [13] R. Sindhu, P. Binod, and A. Pandey, "Biological pretreatment of lignocellulosic biomass - An overview," *Bioresource Technology*, vol. 199, pp. 76-82, 2016.
- [14] G. Brodeur, E. Yau, K. Badal, J. Collier, K. B. Ramachandran, and S. Ramakrishnan, "Chemical and Physicochemical Pretreatment of Lignocellulosic Biomass: A Review," *Enzyme Research*, vol. 2011, pp. 1-17, 2011.
- [15] A. Waheed *et al.*, "Insight into progress in pre-treatment of lignocellulosic biomass," *Energy*, vol. 122, pp. 724-745, 2017.
- [16] H. Bennadji, K. Smith, M. J. Serapiglia, and E. M. Fisher, "Effect of particle size on low-temperature pyrolysis of woody biomass," *Energy and Fuels*, vol. 28, no. 12, pp. 7527-7537, 2014.
- [17] R. B. Bates and A. F. Ghoniem, "Modeling kinetics-transport interactions during biomass torrefaction: The effects of temperature, particle size, and moisture content," *Fuel*, vol. 137, pp. 216-229, 2014.
- [18] J. Shen, X. S. Wang, M. Garcia-Perez, D. Mourant, M. J. Rhodes, and C. Z. Li, "Effects of particle size on the fast pyrolysis of oil mallee woody biomass," *Fuel*, vol. 88, no. 10, pp. 1810-1817, 2009.
- [19] A. Gupta and J. P. Verma, "Sustainable bio-ethanol production from agro-residues: A review," *Renewable and Sustainable Energy Reviews*, vol. 41, pp. 550-567, 2015.
- [20] S. Kumar and S. Dasappa, "Modeling and analysis of single particle conversion of biomass in a packed bed gasification system," *Applied Thermal Engineering*, vol. 112, pp. 1382-1395, 2017.
- [21] P. E. Mason, L. I. Darvell, J. M. Jones, M. Pourkashanian, and A. Williams, "Single particle flame-combustion studies on solid biomass fuels," *Fuel*, vol. 151, pp. 21-30, 2015.
- [22] A. Califice, F. Michel, G. Dislaire, and E. Pirard, "Influence of particle shape on size distribution measurements by 3D and 2D image analyses and laser diffraction," *Powder Technology*, vol. 237, pp. 67-75, 2013.
- [23] G. Wiggins, S. Daw, and P. Ciesielski, "Particle-scale computational modeling of woody biomass pyrolysis," 2014.
- [24] !!! INVALID CITATION !!! [2, 6, 19-21].

- [25] S.-k. Han, H.-s. Han, J. A. Bisson, and T. D. Montgomery, "Effects of grate size on grinding productivity , fuel consumption , and particle size distribution," 2012.
- [26] H. J. Park *et al.*, "Effects of the operating parameters on the production of bio-oil in the fast pyrolysis of Japanese larch," *Chemical Engineering Journal*, vol. 143, no. 1-3, pp. 124-132, 2008.
- [27] Q. Xue and R. O. Fox, "Computational Modeling of Biomass Thermochemical Conversion in Fluidized Beds: Particle Density Variation and Size Distribution," *Industrial & Engineering Chemistry Research*, vol. 54, no. 16, pp. 4084-4094, 2015.
- [28] A. M. C. Janse, R. W. J. Westerhout, and W. Prins, "Modelling of flash pyrolysis of a single wood particle," vol. 39, pp. 239-252, 2000.
- [29] H. Luo, H. Wu, W. Lin, K. Dam-Johansen, and H. Luo, "Heat transfer corrected isothermal model for devolatilization of thermally-thick biomass particles," 2017.
- [30] K. Papadikis, A. V. Bridgwater, and S. Gu, "CFD modelling of the fast pyrolysis of biomass in fluidised bed reactors, Part A: Eulerian computation of momentum transport in bubbling fluidised beds," *Chemical Engineering Science*, vol. 63, no. 16, pp. 4218-4227, 2008.
- [31] K. Papadikis, S. Gu, and A. V. Bridgwater, "CFD modelling of the fast pyrolysis of biomass in fluidised bed reactors. Part B. Heat, momentum and mass transport in bubbling fluidised beds," *Chemical Engineering Science*, vol. 64, no. 5, pp. 1036-1045, 2009.
- [32] Q. Xue, T. J. Heindel, and R. O. Fox, "A CFD model for biomass fast pyrolysis in fluidized-bed reactors," *Chemical Engineering Science*, vol. 66, no. 11, pp. 2440-2452, 2011.
- [33] X. Yu, P. H. Blanco, Y. Makkawi, and A. V. Bridgwater, "CFD and experimental studies on a circulating fluidised bed reactor for biomass gasification," *Chemical Engineering and Processing - Process Intensification*, vol. 130, no. June, pp. 284-295, 2018.
- [34] X. Yu, M. Hassan, R. Ocone, and Y. Makkawi, "A CFD study of biomass pyrolysis in a downer reactor equipped with a novel gas-solid separator-II thermochemical performance and products," *Fuel Processing Technology*, vol. 133, pp. 51-63, 2015.
- [35] D. National Energy Education, "Biomass at a glance," 2006.
- [36] J. Cai *et al.*, "Review of physicochemical properties and analytical characterization of lignocellulosic biomass," *Renewable and Sustainable Energy Reviews*, vol. 76, no. March, pp. 309-322, 2017.
- [37] M. P, "Energy production from biomass (part 1): overview of biomass. Bioresour," *Technol*, vol. 83, no. July 2001, pp. 37-46, 2002.
- [38] D. Mohan, C. U. Pittman, and P. H. Steele, "Pyrolysis of wood/biomass for bio-oil: A critical review," *Energy and Fuels*, vol. 20, no. 3, pp. 848-889, 2006.
- [39] S. Malherbe and T. E. Cloete, "Lignocellulose biodegradation: Fundamentals and applications," *Reviews in Environmental Science and Biotechnology*, vol. 1, no. 2, pp. 105-114, 2002.
- [40] F. H. Isikgor and C. R. Becer, "Lignocellulosic biomass: a sustainable platform for the production of bio-based chemicals and polymers," *Polymer Chemistry*, vol. 6, no. 25, pp. 4497-4559, 2015.
- [41] M. P, "Energy production from biomass (part 1): overview of biomass.," *Technol*, vol. 83, no. July 2001, pp. 37-46, 2002.
- [42] Y. Zhu, Y. Y. Lee, and R. T. Elander, "Optimization of Dilute-Acid Pretreatment of Corn Stover Using a High-Solids Percolation Reactor," in *Twenty-Sixth Symposium on Biotechnology for Fuels and Chemicals*, B. H. Davison, B. R. Evans, M. Finkelstein, and J. D. McMillan, Eds. Totowa, NJ: Humana Press, 2005, pp. 1045-1054.
- [43] P. Bajpai, "Pretreatment of Lignocellulosic Biomass for Biofuel Production," 2016.
- [44] P. Kumar *et al.*, "Methods for Pretreatment of Lignocellulosic Biomass for Efficient Hydrolysis and Biofuel Production," *Industrial and Engineering Chemistry (Analytical*

- Edition*), vol. 48, no. 8, pp. 3713-3729, 2009.
- [45] E. M. Rubin, "Genomics of cellulosic biofuels," *Nature*, vol. 454, no. 7206, pp. 841-845, 2008.
- [46] V. B. Agbor, N. Cicek, R. Sparling, A. Berlin, and D. B. Levin, "Biomass pretreatment: Fundamentals toward application," *Biotechnology Advances*, vol. 29, no. 6, pp. 675-685, 2011.
- [47] C. T. W. J. R. H. Jaya Shankar Tumuluru and L. K. Kevin, "A review of biomass densification systems to develop uniform feedstock commodities for bioenergy application†," *Biofuels, Bioproducts and Biorefining*, vol. 6, no. 3, pp. 683-707, 2011.
- [48] M. S. Mettler, D. G. Vlachos, and P. J. Dauenhauer, "Top ten fundamental challenges of biomass pyrolysis for biofuels," *Energy & Environmental Science*, vol. 5, no. 7, pp. 7797-7797, 2012.
- [49] P. S. Lam and S. Sokhansanj, "Engineering Properties of Biomass," 2014.
- [50] M. Changmai and M. K. Purkait, "Chapter 10 - Membrane adsorption," in *Interface Science and Technology*, vol. 33, M. Ghaedi, Ed.: Elsevier, 2021, pp. 629-653.
- [51] H. Hartmann, T. Bo, and P. Daugbjerg, "Methods for size classification of wood chips," vol. 30, pp. 944-953, 2006.
- [52] M. R. Wu, D. L. Schott, and G. Lodewijks, "Physical properties of solid biomass," vol. 5, 2011.
- [53] M. Momeni, "Fundamental study of single biomass particle combustion," Doctor of, 2012.
- [54] M. Selim, "Evaluation of moisture content in wood fiber and recommendation of the best method for its determination," 2006.
- [55] S. V. Vassilev, D. Baxter, L. K. Andersen, and C. G. Vassileva, "An overview of the chemical composition of biomass," *Fuel*, vol. 89, no. 5, pp. 913-933, 2010/05/01/ 2010.
- [56] S. L. Graham, "DEGRADATION OF BIOMASS FUELS DURING LONG TERM STORAGE IN INDOOR AND OUTDOOR ENVIRONMENTS," 2015.
- [57] T. Lin *et al.*, "Biomass feedstock preprocessing and long-distance transportation logistics," *GCB Bioenergy*, vol. 8, no. 1, pp. 160-170, 2016.
- [58] F. Guo, Y. Dong, T. Zhang, L. Dong, C. Guo, and Z. Rao, "Experimental Study on Herb Residue Gasification in an Air-Blown Circulating Fluidized Bed Gasifier," *Industrial & Engineering Chemistry Research*, vol. 53, no. 34, pp. 13264-13273, 2014/08/27 2014.
- [59] T. T. Li *et al.*, "Characterization of herb residue and high ash-containing paper sludge blends from fixed bed pyrolysis," (in English), *Waste Management*, Article vol. 76, pp. 544-554, Jun 2018.
- [60] P. Wang, S. H. Zhan, H. B. Yu, X. F. Xue, and N. Hong, "The effects of temperature and catalysts on the pyrolysis of industrial wastes (herb residue)," (in English), *Bioresource Technology*, Article vol. 101, no. 9, pp. 3236-3241, May 2010.
- [61] T. P. Wang, L. Peng, Y. N. Ai, R. H. Zhang, and Q. Lu, "Pyrolytic behaviors of decocting residues of *Rhodiola rosea*," (in English), *Journal of Analytical and Applied Pyrolysis*, Article vol. 129, pp. 61-65, Jan 2018.
- [62] A. Z. Xu *et al.*, "Gas production by catalytic pyrolysis of herb residues using Ni/CaO catalysts," (in English), *Journal of Analytical and Applied Pyrolysis*, Article vol. 130, pp. 216-223, Mar 2018.
- [63] B. F. Zhao *et al.*, "Catalytic Pyrolysis of Herb Residues for the Preparation of Hydrogen-Rich Gas," (in English), *Energy & Fuels*, Article; Proceedings Paper vol. 34, no. 2, pp. 1131-1136, Feb 2020.
- [64] J. H. Park, Y. K. Park, and Y. M. Kim, "Kinetic analysis and catalytic pyrolysis of spent medicinal herb over HZSM-5 and HY," (in English), *Environmental Research*, Article vol. 187, Aug 2020, Art. no. 109632.
- [65] B. Zhang and J. Zhang, "Influence of Reaction Atmosphere (N-2, CO, CO2, and H-2) on ZSM-5 Catalyzed Microwave-Induced Fast Pyrolysis of Medicinal Herb Residue

- for Biofuel Production," (in English), *Energy & Fuels*, Article vol. 31, no. 9, pp. 9627-9632, Sep 2017.
- [66] W. J. Ding *et al.*, "TG-FTIR and thermodynamic analysis of the herb residue pyrolysis with in-situ CO<sub>2</sub> capture using CaO catalyst," (in English), *Journal of Analytical and Applied Pyrolysis*, Article vol. 134, pp. 389-394, Sep 2018.
- [67] B. F. Zhao *et al.*, "A study of the in-situ CO<sub>2</sub> removal pyrolysis of Chinese herb residue for syngas production," (in English), *Science of the Total Environment*, Article vol. 626, pp. 703-709, Jun 2018.
- [68] R. H. Venderbosch, "A Critical View on Catalytic Pyrolysis of Biomass," *ChemSusChem*, <https://doi.org/10.1002/cssc.201500115> vol. 8, no. 8, pp. 1306-1316, 2015/04/24 2015.
- [69] W. H. Zhou, B. Bai, G. Y. Chen, L. L. Ma, D. W. Jing, and B. B. Yan, "Study on catalytic properties of potassium carbonate during the process of sawdust pyrolysis," (in English), *International Journal of Hydrogen Energy*, Article; Proceedings Paper vol. 43, no. 30, pp. 13829-13841, Jul 2018.
- [70] W. Tao, J. Jin, Y. Zheng, and S. Li, "Current Advances of Resource Utilization of Herbal Extraction Residues in China," *Waste and Biomass Valorization*, vol. 12, 11/01 2021.
- [71] S. Jia, S. Ning, H. Ying, Y. Sun, W. Xu, and H. Yin, "High quality syngas production from catalytic gasification of woodchip char," *Energy Conversion and Management*, vol. 151, pp. 457-464, Nov 1 2017.
- [72] M. Safar *et al.*, "Catalytic effects of potassium on biomass pyrolysis, combustion and torrefaction," (in English), *Applied Energy*, vol. 235, pp. 346-355, Feb 1 2019.
- [73] X. Y. Liu *et al.*, "Synergy of steam reforming and K<sub>2</sub>CO<sub>3</sub> modification on wood biomass pyrolysis," (in English), *Cellulose*, vol. 26, no. 10, pp. 6049-6060, Jul 2019.
- [74] B. Zhao *et al.*, "Catalytic Pyrolysis of Herb Residues for the Preparation of Hydrogen-Rich Gas," *Energy & Fuels*, vol. 34, no. 2, pp. 1131-1136, Feb 2020.
- [75] H. B. Zhao, W. T. Xu, Q. Song, J. K. Zhuo, and B. Yao, "Effect of Steam and SiO<sub>2</sub> on the Release and Transformation of K<sub>2</sub>CO<sub>3</sub> and KCl during Biomass Thermal Conversion," (in English), *Energy & Fuels*, vol. 32, no. 9, pp. 9633-9639, Sep 2018.
- [76] H. J. Fan, X. L. Chang, J. Wang, and Z. X. Zhang, "Catalytic pyrolysis of agricultural and forestry wastes in a fixed-bed reactor using K<sub>2</sub>CO<sub>3</sub> as the catalyst," (in English), *Waste Management & Research*, vol. 38, no. 1, pp. 78-87, Jan 2020.
- [77] G. M. Wiggins, P. N. Ciesielski, and C. S. Daw, "Low-Order Modeling of Internal Heat Transfer in Biomass Particle Pyrolysis," *Energy and Fuels*, vol. 30, no. 6, pp. 4960-4969, 2016.
- [78] M. Gil, E. Teruel, and I. Arauzo, "Analysis of standard sieving method for milled biomass through image processing. Effects of particle shape and size for poplar and corn stover," *Fuel*, vol. 116, pp. 328-340, 2014.
- [79] A. Trubetskaya, G. Beckmann, J. Wadenbäck, J. K. Holm, S. P. Velaga, and R. Weber, "One way of representing the size and shape of biomass particles in combustion modeling," *Fuel*, vol. 206, pp. 675-683, 2017.
- [80] P. N. Ciesielski *et al.*, "Biomass particle models with realistic morphology and resolved microstructure for simulations of intraparticle transport phenomena," *Energy and Fuels*, vol. 29, no. 1, pp. 242-254, 2015.
- [81] A. K. Biswas and K. Umeki, "Simplification of devolatilization models for thermally-thick particles: Differences between wood logs and pellets," *Chemical Engineering Journal*, vol. 274, pp. 181-191, 2015.
- [82] P. N. Ciesielski, G. M. Wiggins, J. E. Jakes, and C. S. Daw, "Simulating Biomass Fast Pyrolysis at the Single Particle Scale," 2017, pp. 231-253.
- [83] G. Wiggins, S. Daw, and P. Ciesielski, "Modeling the Impact of Biomass Particle Size Distribution and Shape on Heating Behavior During Fast Pyrolysis," 2016.
- [84] H. Lu, E. Ip, J. Scott, P. Foster, M. Vickers, and L. L. Baxter, "Effects of particle shape



- and size on devolatilization of biomass particle," *Fuel*, vol. 89, no. 5, pp. 1156-1168, 2010.
- [85] S. Radl, F. Krainer, T. Puffitsch, and C. Kloss, *Biot Number Effects on the Local Heat and Mass Transfer Rate in Fixed and Fluidized Beds*. 2015.
- [86] K. Papadikis, S. Gu, A. V. Bridgwater, and H. Gerhauser, "Application of CFD to model fast pyrolysis of biomass," *Fuel Processing Technology*, vol. 90, no. 4, pp. 504-512, 2009.
- [87] A. Gagliano, F. Nocera, and M. Bruno, "2 - Simulation Models of Biomass Thermochemical Conversion Processes, Gasification and Pyrolysis, for the Prediction of the Energetic Potential," in *Advances in Renewable Energies and Power Technologies*, I. Yahyaoui, Ed.: Elsevier, 2018, pp. 39-85.
- [88] B. J. R. Mungyeke Bisulandu and F. Marias, "Modeling of the Thermochemical Conversion of Biomass in Cement Rotary Kiln," *Waste and Biomass Valorization*, vol. 12, no. 2, pp. 1005-1024, 2021/02/01 2021.
- [89] P. Bernada, F. Marias, A. Deydier, F. Couture, and A. Fourcalt, "Modelling of a Traveling Bed WASTE Gasifier," *Waste and Biomass Valorization*, vol. 3, no. 3, pp. 333-353, 2012/09/01 2012.
- [90] R. K. Jalan and V. K. Srivastava, "Studies on pyrolysis of a single biomass cylindrical pellet - Kinetic and heat transfer effects," *Energy Conversion and Management*, vol. 40, no. 5, pp. 467-494, 1999.
- [91] C. Di Blasi, "Heat, momentum and mass transport through a shrinking biomass particle exposed to thermal radiation," *Chemical Engineering Science*, vol. 51, no. 7, pp. 1121-1132, 1996.
- [92] C. Di Blasi, "Modeling chemical and physical processes of wood and biomass pyrolysis," *Progress in Energy and Combustion Science*, vol. 34, no. 1, pp. 47-90, 2008.
- [93] T. Liliedahl and K. Sjöström, "Heat transfer controlled pyrolysis kinetics of a biomass slab, rod or sphere," *Biomass and Bioenergy*, vol. 15, no. 6, pp. 503-509, 1998.
- [94] A. V. Bridgwater, D. Meier, and D. Radlein, "An overview of fast pyrolysis of biomass," *Organic Geochemistry*, vol. 30, no. 12, pp. 1479-1493, 1999.
- [95] A. V. Bridgwater, "Challenges and Opportunities in Fast Pyrolysis of Biomass : Part I," *Johnson Matthey Technol. Rev*, vol. 62, no. 1, pp. 118-130, 2018.
- [96] E. F. J. M. B. I. S.-R. B. R. N.Ferrera-Lorenzo, "Conventional and microwave pyrolysis of a macroalgae waste from the Agar-Agar industry. Prospects for bio-fuel production," *Bioresource Technology*, vol. 206, pp. 199-206, 2014.
- [97] M. Balat, M. Balat, E. Kirtay, and H. Balat, "Main routes for the thermo-conversion of biomass into fuels and chemicals. Part 1: Pyrolysis systems," *Energy Conversion and Management*, vol. 50, no. 12, pp. 3147-3157, 2009.
- [98] M. I. Jahirul, M. G. Rasul, A. A. Chowdhury, and N. Ashwath, "Biofuels production through biomass pyrolysis- A technological review," *Energies*, vol. 5, no. 12, pp. 4952-5001, 2012.
- [99] J. Lédé, "Biomass Fast Pyrolysis Reactors: A Review of a Few Scientific Challenges and of Related Recommended Research Topics," *Oil & Gas Science and Technology – Revue d'IFP Energies nouvelles*, vol. 68, no. 5, pp. 801-814, 2013.
- [100] S. Hameed, A. Sharma, V. Pareek, H. Wu, and Y. Yu, "A review on biomass pyrolysis models: Kinetic, network and mechanistic models," *Biomass and Bioenergy*, vol. 123, pp. 104-122, 2019/04/01/ 2019.
- [101] N. Prakash and T. Karunanithi, "Kinetic Modeling in Biomass Pyrolysis - A Review," *Journal of Applied Sciences Research*, vol. 4, no. 12, pp. 1627-1636, 2008.
- [102] P. Abelha, I. Gulyurtlu, and I. Cabrita, "Release Of Nitrogen Precursors From Coal And Biomass Residues in a Bubbling Fluidized Bed," *Energy & Fuels*, vol. 22, no. 1, pp. 363-371, 2008/01/01 2008.
- [103] Q. Ren *et al.*, "Formation of NO<sub>x</sub> precursors during wheat straw pyrolysis and gasification with O<sub>2</sub> and CO<sub>2</sub>," *Fuel*, vol. 89, no. 5, pp. 1064-1069, 2010/05/01/ 2010.

- [104] M. A. Wójtowicz, J. R. Pels, and J. A. Moulijn, "Combustion of coal as a source of N<sub>2</sub>O emission," *Fuel Processing Technology*, vol. 34, no. 1, pp. 1-71, 1993/06/01/ 1993.
- [105] P. R. Solomon and M. B. Colket, "Evolution of fuel nitrogen in coal devolatilization," *Fuel*, vol. 57, no. 12, pp. 749-755, 1978/12/01/ 1978.
- [106] X. Ke *et al.*, "Prediction and minimization of NO<sub>x</sub> emission in a circulating fluidized bed combustor: A comprehensive mathematical model for CFB combustion," *Fuel*, vol. 309, p. 122133, 2022/02/01/ 2022.
- [107] X. Niu and L. Shen, "Evolution of carbon and nitrogen during chemical looping gasification of rapeseed cake with Ca-Fe oxygen carrier," *Chemical Engineering Journal*, vol. 431, p. 134232, 2022/03/01/ 2022.
- [108] O. Karlström, E. Vainio, M. Engblom, A. Brink, and M. Hupa, "Effect of air staging on NO<sub>x</sub> emissions in biomass combustion in a bubbling fluidized bed," *Fuel*, vol. 330, p. 125565, 2022/12/15/ 2022.
- [109] H. Zhan *et al.*, "Characteristics of NO<sub>x</sub> precursors and their formation mechanism during pyrolysis of herb residues," *Journal of Fuel Chemistry and Technology*, vol. 45, no. 3, pp. 279-288, 2017/03/01/ 2017.
- [110] H. Zhan, X. Yin, Y. Huang, H. Yuan, and C. Wu, "NO<sub>x</sub> precursors evolving during rapid pyrolysis of lignocellulosic industrial biomass wastes," *Fuel*, vol. 207, pp. 438-448, 2017/11/01/ 2017.
- [111] X. Zhu *et al.*, "Tracking the conversion of nitrogen during pyrolysis of antibiotic mycelial fermentation residues using XPS and TG-FTIR-MS technology," *Environmental Pollution*, vol. 211, pp. 20-27, 2016/04/01/ 2016.
- [112] F. Winter, C. Wartha, and H. Hofbauer, "NO and N<sub>2</sub>O formation during the combustion of wood, straw, malt waste and peat," *Bioresource Technology*, vol. 70, no. 1, pp. 39-49, 1999/10/01/ 1999.
- [113] K.-M. Hansson, L.-E. Åmand, A. Habermann, and F. Winter, "Pyrolysis of poly-l-leucine under combustion-like conditions ☆," *Fuel*, vol. 82, no. 6, pp. 653-660, 2003/04/01/ 2003.
- [114] W. Chen, H. Yang, Y. Chen, M. Xia, X. Chen, and H. Chen, "Transformation of Nitrogen and Evolution of N-Containing Species during Algae Pyrolysis," *Environmental science & technology*, vol. 51 11, pp. 6570-6579, 2017.
- [115] J. Leppälähti and T. Koljonen, "Nitrogen evolution from coal, peat and wood during gasification: Literature review," *Fuel Processing Technology*, vol. 43, no. 1, pp. 1-45, 1995/05/01/ 1995.
- [116] J. R. Pels, F. Kapteijn, J. A. Moulijn, Q. Zhu, and K. M. Thomas, "Evolution of nitrogen functionalities in carbonaceous materials during pyrolysis," *Carbon*, vol. 33, no. 11, pp. 1641-1653, 1995/01/01/ 1995.
- [117] R. M. Davidson, "Nitrogen in coal," IEA Coal Research, London (United Kingdom), United Kingdom1994-01-01 1994.
- [118] W. Chen, H. Yang, Y. Chen, K. Li, M. Xia, and H. Chen, "Influence of Biochar Addition on Nitrogen Transformation during Copyrolysis of Algae and Lignocellulosic Biomass," *Environmental Science & Technology*, vol. 52, no. 16, pp. 9514-9521, 2018/08/21 2018.
- [119] W. Chen *et al.*, "Co-pyrolysis of lignocellulosic biomass and microalgae: Products characteristics and interaction effect," *Bioresource Technology*, vol. 245, pp. 860-868, 2017/12/01/ 2017.
- [120] H. Schmiers, J. Friebel, P. Streubel, R. Hesse, and R. Köpsel, "Change of chemical bonding of nitrogen of polymeric N-heterocyclic compounds during pyrolysis," *Carbon*, vol. 37, no. 12, pp. 1965-1978, 1999/01/01/ 1999.
- [121] N. Tsubouchi, "Effects of Solid Residence Time and Inherent Metal Cations on the Fate of the Nitrogen in Coal during Rapid Pyrolysis," *Energy & Fuels*, vol. 28, no. 9, pp. 5721-5728, 2014/09/18 2014.
- [122] N. Tsubouchi and Y. Ohtsuka, "Nitrogen chemistry in coal pyrolysis: Catalytic roles of

- metal cations in secondary reactions of volatile nitrogen and char nitrogen," *Fuel Processing Technology*, vol. 89, no. 4, pp. 379-390, 2008/04/01/ 2008.
- [123] S. R. Kelemen *et al.*, "Nitrogen Transformations in Coal during Pyrolysis," *Energy & Fuels*, vol. 12, no. 1, pp. 159-173, 1998/01/01 1998.
- [124] Q. Ren and C. Zhao, "NO<sub>x</sub> and N<sub>2</sub>O precursors (NH<sub>3</sub> and HCN) from biomass pyrolysis: interaction between amino acid and mineral matter," *Applied Energy*, vol. 112, pp. 170-174, 2013/12/01/ 2013.
- [125] A. Gómez-Barea and B. Leckner, "Modeling of biomass gasification in fluidized bed," *Progress in Energy and Combustion Science*, vol. 36, no. 4, pp. 444-509, 2010.
- [126] A. K. Thakur, "Model: Mechanistic vs Empirical," in *New Trends in Pharmacokinetics*, A. Rescigno and A. K. Thakur, Eds. Boston, MA: Springer US, 1991, pp. 41-51.
- [127] R. A. Cottis, "13 - Modelling corrosion in nuclear power plant systems," in *Nuclear Corrosion Science and Engineering*, D. Féron, Ed.: Woodhead Publishing, 2012, pp. 438-448.
- [128] J. Montoya, B. Pecha, F. C. Janna, and M. Garcia-Perez, "Single particle model for biomass pyrolysis with bubble formation dynamics inside the liquid intermediate and its contribution to aerosol formation by thermal ejection," *Journal of Analytical and Applied Pyrolysis*, vol. 124, pp. 204-218, 2017.
- [129] Y. B. Yang *et al.*, "Combustion of a Single Particle of Biomass," *Energy*, no. 8, pp. 306-316, 2008.
- [130] P. N. Ciesielski, G. M. Wiggins, J. E. Jakes, and C. S. Daw, "CHAPTER 11 Simulating Biomass Fast Pyrolysis at the Single Particle Scale," in *Fast Pyrolysis of Biomass: Advances in Science and Technology*: The Royal Society of Chemistry, 2017, pp. 231-253.
- [131] X. Jiang, D. Chen, Z. Ma, and J. Yan, "Models for the combustion of single solid fuel particles in fluidized beds: A review," *Renewable and Sustainable Energy Reviews*, vol. 68, no. October 2016, pp. 410-431, 2017.
- [132] M. Bidabadi, M. R. Moghaddam, S. A. Mostafavi, F. F. Dizaji, and H. B. Dizaji, "An analytical model for pyrolysis of a single biomass particle," *Journal of Central South University*, vol. 22, no. 1, pp. 350-359, 2015.
- [133] B. Liu *et al.*, "CFD modelling of particle shrinkage in a fluidized bed for biomass fast pyrolysis with quadrature method of moment," *Fuel Processing Technology*, vol. 164, pp. 51-68, 2017.
- [134] A. K. Sadhukhan, P. Gupta, and R. K. Saha, "Modelling of pyrolysis of large wood particles," *Bioresource Technology*, vol. 100, no. 12, pp. 3134-3139, 2009.
- [135] C. Choi, W. Zhang, K. Fukumoto, H. Machida, and K. Norinaga, "A Review on Detailed Kinetic Modeling and Computational Fluid Dynamics of Thermochemical Processes of Solid Fuels," *Energy & Fuels*, vol. 35, no. 7, pp. 5479-5494, 2021/04/01 2021.
- [136] K. M. L. S. F. L. T. F. W. P. Walawender, "A Mathematical Model for Pyrolysis of a Solid Particle - Effects of the Heat of Reaction," *The Canadian Journal of Chemical Engineering*, vol. 55, no. 3, 1977.
- [137] F. Thurner and U. Mann, "Kinetic Investigation of Wood Pyrolysis," *Industrial and Engineering Chemistry Process Design and Development*, vol. 20, no. 3, pp. 482-488, 1981.
- [138] A. G. W. Bradbury, Y. Sakai, and F. Shafizadeh, "A kinetic model for pyrolysis of cellulose," *Journal of Applied Polymer Science*, vol. 23, no. 11, pp. 3271-3280, 1979.
- [139] F. Thurner, U. Mann, and S. R. Beck, "Kinetic investigation of wood pyrolysis," United States 1980-06-01 1980, Available: <https://www.osti.gov/biblio/6809951>  
<https://www.osti.gov/servlets/purl/6809951>.
- [140] Q.-V. Bach and W.-H. Chen, "Pyrolysis characteristics and kinetics of microalgae via thermogravimetric analysis (TGA): A state-of-the-art review," *Bioresource Technology*, vol. 246, pp. 88-100, 12/01 2017.

- [141] R. K. Mishra and K. Mohanty, "Pyrolysis kinetics and thermal behavior of waste sawdust biomass using thermogravimetric analysis," *Bioresource Technology*, vol. 251, pp. 63-74, 2018/03/01/ 2018.
- [142] M. J. Starink, "The determination of activation energy from linear heating rate experiments: a comparison of the accuracy of isoconversion methods," *Thermochimica Acta*, vol. 404, no. 1-2, pp. 163-176, 2003.
- [143] L. Xu, Y. Jiang, and L. Wang, "Thermal decomposition of rape straw: Pyrolysis modeling and kinetic study via particle swarm optimization," *Energy Conversion and Management*, vol. 146, pp. 124-133, 2017/08/15/ 2017.
- [144] A. Khawam and D. R. Flanagan, "Solid-state kinetic models: Basics and mathematical fundamentals," (in English), *Journal of Physical Chemistry B*, Review vol. 110, no. 35, pp. 17315-17328, Sep 2006.
- [145] Y. S. Lin *et al.*, "Thermal behavior and general distributed activation energy model kinetics of Lignite-Chinese herb residues blends during co-pyrolysis," (in English), *Bioresource Technology*, Article vol. 304, May 2020, Art. no. 122991.
- [146] Y. Lin *et al.*, "General distributed activation energy model (G-DAEM) on co-pyrolysis kinetics of bagasse and sewage sludge," *Bioresource Technology*, vol. 273, pp. 545-555, 2019/02/01/ 2019.
- [147] M. Radojević, B. Janković, V. Jovanović, D. Stojiljković, and N. Manić, "Comparative pyrolysis kinetics of various biomasses based on model-free and DAEM approaches improved with numerical optimization procedure," *PLOS ONE*, vol. 13, no. 10, p. e0206657, 2018.
- [148] X. Shi, F. Ronsse, and J. G. Pieters, "Finite element modeling of intraparticle heterogeneous tar conversion during pyrolysis of woody biomass particles," *Fuel Processing Technology journal*, vol. 148, pp. 302-316, 2016.
- [149] K. U. C. Perera and M. Narayana, "Finite volume analysis of biomass particle pyrolysis," in *2017 Moratuwa Engineering Research Conference (MERCon)*, 2017, pp. 379-384.
- [150] M. Bellais, K. O. Davidsson, T. Liliedahl, K. Sjöström, and J. B. C. Pettersson, "Pyrolysis of large wood particles: A study of shrinkage importance in simulations," *Fuel*, vol. 82, no. 12, pp. 1541-1548, 2003.
- [151] M. A. Gómez, J. Porteiro, D. Patiño, and J. L. Míguez, "Fast-solving thermally thick model of biomass particles embedded in a CFD code for the simulation of fixed-bed burners," vol. 105, pp. 30-44, 2015.
- [152] F. Taghipour, N. Ellis, and C. Wong, "Experimental and computational study of gas-solid fluidized bed hydrodynamics," *Chemical Engineering Science*, vol. 60, no. 24, pp. 6857-6867, 2005.
- [153] J. E. Macías-Díaz, R. E. Landry, and A. Puri, "A finite-difference scheme in the computational modelling of a coupled substrate-biomass system," *International Journal of Computer Mathematics*, vol. 91, no. 10, pp. 2199-2214, 2014.
- [154] Y. Pan and S.-c. Kong, "Simulation of biomass particle evolution under pyrolysis conditions using lattice Boltzmann method," *Combustion and Flame*, vol. 178, pp. 21-34, 2017.
- [155] S. Succi, M. Sbragaglia, and S. Ubertini, "Lattice Boltzmann Method," *Scholarpedia*, vol. 5, no. 5, pp. 9507-9507, 2010.
- [156] J. Porteiro, J. L. Míguez, E. Granada, and J. C. Moran, "Mathematical modelling of the combustion of a single wood particle," *Fuel Processing Technology*, vol. 87, no. 2, pp. 169-175, 2006.
- [157] J. Porteiro, E. Granada, J. Collazo, D. Patiño, and J. C. Morán, "A Model for the Combustion of Large Particles of Densified Wood," no. 8, pp. 3151-3159, 2010.
- [158] J. Li, M. C. Paul, P. L. Younger, I. Watson, M. Hossain, and S. Welch, "Characterization of biomass combustion at high temperatures based on an upgraded single particle model," *Applied Energy*, vol. 156, pp. 749-755, 2015.

- [159] Y. Haseli, J. A. van Oijen, and L. P. H. de Goey, "A detailed one-dimensional model of combustion of a woody biomass particle," *Bioresource Technology*, vol. 102, no. 20, pp. 9772-9782, 2011.
- [160] K. M. Bryden and M. J. Hage, "Modeling the combined impact of moisture and char shrinkage on the pyrolysis of a biomass particle," *Fuel*, vol. 82, no. 13, pp. 1633-1644, 2003.
- [161] H. Rezaei, S. Sokhansanj, X. Bi, C. J. Lim, and A. Lau, "A numerical and experimental study on fast pyrolysis of single woody biomass particles," *Applied Energy*, vol. 198, pp. 320-331, 2017.
- [162] G. Gentile, P. E. A. Debiagi, A. Cuoci, A. Frassoldati, E. Ranzi, and T. Faravelli, "A computational framework for the pyrolysis of anisotropic biomass particles," *Chemical Engineering Journal*, vol. 321, pp. 458-473, 2017.
- [163] J. Larfeldt, B. Leckner, and M. C. Melaaen, "Modelling and measurements of heat transfer in charcoal from pyrolysis of large wood particles," *Biomass and Bioenergy*, vol. 18, no. 6, pp. 507-514, 2000.
- [164] M. Mohseni, B. Peters, and M. Baniasadi, "Conversion analysis of a cylindrical biomass particle with a DEM-CFD coupling approach," *Case Studies in Thermal Engineering*, vol. 10, no. September, pp. 343-356, 2017.
- [165] N. Sousa and J. L. T. Azevedo, "Model simplifications on biomass particle combustion," *Fuel*, vol. 184, pp. 948-956, 2016.
- [166] K. M. Bryden, K. W. Ragland, and C. J. Rutland, "Modeling thermally thick pyrolysis of wood," *Biomass and Bioenergy*, vol. 22, no. 1, pp. 41-53, 2002.
- [167] Y. Haseli, J. A. Van Oijen, and L. P. H. De Goey, "Modeling biomass particle pyrolysis with temperature-dependent heat of reactions," *Journal of Analytical and Applied Pyrolysis*, vol. 90, no. 2, pp. 140-154, 2011.
- [168] C. D. Blasi, "Physico-chemical processes occurring inside a degrading two-dimensional anisotropic porous medium," *International Journal of Heat and Mass Transfer*, vol. 41, no. 24, pp. 4139-4150, 1998.
- [169] P. Wang and B. H. Howard, "Impact of Thermal Pretreatment Temperatures on Woody Biomass Chemical Composition, Physical Properties and Microstructure," *Energies*, vol. 11, p. 20, 2017 2017.
- [170] J. C. Wurzenberger, S. Wallner, H. Raupenstrauch, and J. G. Khinast, "Thermal conversion of biomass: Comprehensive reactor and particle modeling," *AIChE Journal*, vol. 48, no. 10, pp. 2398-2411, 2002.
- [171] M. J. Hounslow, "The Population Balance as a Tool for Understanding Particle Rate Processes," *KONA Powder and Particle Journal*, pp. 179-193, 1998.
- [172] J. U. h. b. g. c. u. b. i. t. k. Litster, *Design and Processing of Particulate Products*. Cambridge University Press, 2016.
- [173] H. M. Hulburt and S. Katz, "Some problems in particle technology: A statistical mechanical formulation," *Chemical Engineering Science*, vol. 19, no. 8, pp. 555-574, 1964.
- [174] A. D. Randolph, "A population balance for countable entities," *The Canadian Journal of Chemical Engineering*, vol. 42, no. 6, pp. 280-281, 1964.
- [175] B. G. Lakatos, "Population balance modelling of crystallisation processes," *Hungarian Journal of Industrial Chemistry*, vol. 35, pp. 7-17, 2007.
- [176] X. Yu, M. J. Hounslow, G. K. Reynolds, A. Rasmuson, I. Niklasson Björn, and P. J. Abrahamsson, "A compartmental CFD-PBM model of high shear wet granulation," *AIChE Journal*, vol. 63, no. 2, pp. 438-458, 2017.
- [177] M. Gil, E. Luciano, and I. Arauzo, "Population balance model for biomass milling," *Powder Technology*, vol. 276, pp. 34-44, 2015.
- [178] M. J. H. G. K. R. Xi Yu, "Accuracy and Optimal Sampling in Monte Carlo Solution of Population Balance Equations," *Particle Technology and Fluidization*, vol. 61, no. 8, pp. 3-194, 2015.

- [179] G. Natale, A. Galgano, and C. Di Blasi, "Modeling particle population balances in fluidized-bed wood gasifiers," *Biomass and Bioenergy*, vol. 62, pp. 123-137, 2014.
- [180] X. Yu, M. Hounslow, and G. Reynolds, "Accuracy and optimal sampling in Monte Carlo solution of population balance equations," *AIChE Journal*, vol. 61, pp. 2394-2402, 09/15 2015.
- [181] Y. Hu, Z. Wang, X. Cheng, and C. Ma, "Non-isothermal TGA study on the combustion reaction kinetics and mechanism of low-rank coal char," *RSC Advances*, vol. 8, pp. 22909-22916, 06/21 2018.
- [182] H. Zhu *et al.*, "Thermogravimetric characteristics and kinetics of herb residues catalyzed by potassium carbonate," *Journal of Analytical and Applied Pyrolysis*, vol. 156, p. 105170, 2021/06/01/ 2021.
- [183] W.-H. Chen, B.-J. Lin, M.-Y. Huang, and J.-S. Chang, "Thermochemical conversion of microalgal biomass into biofuels: A review," *Bioresource Technology*, vol. 184, pp. 314-327, 2015/05/01/ 2015.
- [184] S. Vyazovkin, A. K. Burnham, J. M. Criado, L. A. Pérez-Maqueda, C. Popescu, and N. Sbirrazzuoli, "ICTAC Kinetics Committee recommendations for performing kinetic computations on thermal analysis data," *Thermochimica Acta*, vol. 520, no. 1-2, pp. 1-19, 2011.
- [185] M. J. Starink, "A new method for the derivation of activation energies from experiments performed at constant heating rate," *Thermochimica Acta*, vol. 288, no. 1, pp. 97-104, 1996/10/10/ 1996.
- [186] N. Koga and J. M. Criado, "Kinetic Analyses of Solid-State Reactions with a Particle-Size Distribution," *Journal of the American Ceramic Society*, <https://doi.org/10.1111/j.1151-2916.1998.tb02712.x> vol. 81, no. 11, pp. 2901-2909, 1998/11/01 1998.
- [187] F. J. Gotor, J. M. Criado, J. Malek, and N. Koga, "Kinetic Analysis of Solid-State Reactions: The Universality of Master Plots for Analyzing Isothermal and Nonisothermal Experiments," *The Journal of Physical Chemistry A*, vol. 104, no. 46, pp. 10777-10782, 2000/11/01 2000.
- [188] M. Nishimura, S. Iwasaki, and M. Horio, "The role of potassium carbonate on cellulose pyrolysis," (in English), *Journal of the Taiwan Institute of Chemical Engineers*, vol. 40, no. 6, pp. 630-637, Nov 2009.
- [189] Z. Luo, S. Wang, and X. Guo, "Selective pyrolysis of Organosolv lignin over zeolites with product analysis by TG-FTIR," *Journal of Analytical and Applied Pyrolysis*, vol. 95, pp. 112-117, 2012/05/01/ 2012.
- [190] J. Wannapeera and N. Worasuwannarak, "Examinations of chemical properties and pyrolysis behaviors of torrefied woody biomass prepared at the same torrefaction mass yields," *Journal of Analytical and Applied Pyrolysis*, vol. 115, pp. 279-287, 2015/09/01/ 2015.
- [191] M. Q. Chen *et al.*, "Catalytic characteristic and kinetic modeling of cotton stalk pyrolysis," *Ranliao Huaxue Xuebao/Journal of Fuel Chemistry and Technology*, vol. 39, pp. 585-589, 08/01 2011.
- [192] A. Anca-Couce, A. Berger, and N. Zobel, "How to determine consistent biomass pyrolysis kinetics in a parallel reaction scheme," *Fuel*, vol. 123, pp. 230-240, 2014/05/01/ 2014.
- [193] S. Vyazovkin, A. K. Burnham, J. M. Criado, L. A. Perez-Maqueda, C. Popescu, and N. Sbirrazzuoli, "ICTAC Kinetics Committee recommendations for performing kinetic computations on thermal analysis data," *Thermochimica Acta*, vol. 520, no. 1-2, pp. 1-19, Jun 10 2011.
- [194] J. Cai, W. Wu, R. Liu, and G. W. Huber, "A distributed activation energy model for the pyrolysis of lignocellulosic biomass," *Green Chemistry*, vol. 15, no. 5, pp. 1331-1340, 2013.
- [195] M. Becidan, Ø. Skreiberg, and J. E. Hustad, "NO<sub>x</sub> and N<sub>2</sub>O Precursors (NH<sub>3</sub> and HCN)

- in Pyrolysis of Biomass Residues," *Energy & Fuels*, vol. 21, no. 2, pp. 1173-1180, 2007/03/01 2007.
- [196] K.-M. Hansson, J. Samuelsson, C. Tullin, and L.-E. Åmand, "Formation of HNCO, HCN, and NH<sub>3</sub> from the pyrolysis of bark and nitrogen-containing model compounds," *Combustion and Flame*, vol. 137, no. 3, pp. 265-277, 2004/05/01/ 2004.
- [197] W. Chen, H. Yang, Y. Chen, M. Xia, X. Chen, and H. Chen, "Transformation of Nitrogen and Evolution of N-Containing Species during Algae Pyrolysis," (in eng), *Environ Sci Technol*, vol. 51, no. 11, pp. 6570-6579, Jun 6 2017.
- [198] L. Wei, L. Wen, T. Yang, and N. Zhang, "Nitrogen Transformation during Sewage Sludge Pyrolysis," *Energy & Fuels*, vol. 29, no. 8, pp. 5088-5094, 2015/08/20 2015.
- [199] H. Zhan *et al.*, "Comparisons of Formation Characteristics of NO<sub>x</sub> Precursors during Pyrolysis of Lignocellulosic Industrial Biomass Wastes," *Energy & Fuels*, vol. 31, pp. 9557-9567, 2017.
- [200] P. Okekunle, T. Pattanotai, H. Watanabe, and K. Okazaki, "Numerical and Experimental Investigation of IntraParticle Heat Transfer and Tar Decomposition during Pyrolysis of Wood Biomass," *Journal of Thermal Science and Technology - J THERM SCI TECHNOL*, vol. 6, pp. 360-375, 08/12 2011.
- [201] I. Bonefacic, B. Frankovic, and A. Kazagic, "Cylindrical particle modelling in pulverized coal and biomass co-firing process," *Applied Thermal Engineering*, vol. 78, pp. 74-81, 2015/03/05/ 2015.
- [202] J. Li, M. C. Paul, P. L. Younger, I. Watson, M. Hossain, and S. Welch, "Prediction of high-temperature rapid combustion behaviour of woody biomass particles," *Fuel*, vol. 165, pp. 205-214, 2016.
- [203] D. L. Pyle and C. A. Zaror, "Heat transfer and kinetics in the low temperature pyrolysis of solids," *Chemical Engineering Science*, vol. 39, no. 1, pp. 147-158, 1984.
- [204] E. Grieco and G. Baldi, "Analysis and modelling of wood pyrolysis," *Chemical Engineering Science*, vol. 66, no. 4, pp. 650-660, 2011.
- [205] C. A. Koufopoulos, N. Papayannakos, G. Maschio, and A. Lucchesi, "Modelling of the pyrolysis of biomass particles. Studies on kinetics, thermal and heat transfer effects," *The Canadian Journal of Chemical Engineering*, vol. 69, no. 4, pp. 907-915, 1991.
- [206] W.-C. R. Chan, M. Kelbon, and B. B. Krieger, "Modelling and experimental verification of physical and chemical processes during pyrolysis of a large biomass particle," *Fuel*, vol. 64, no. 11, pp. 1505-1513, 1985/11/01/ 1985.
- [207] A. Galgano and C. D. Blasi, "Modeling Wood Degradation by the Unreacted-Core-Shrinking Approximation," *Industrial & Engineering Chemistry Research*, vol. 42, no. 10, pp. 2101-2111, 2003/05/01 2003.
- [208] J. Porteiro, E. Granada, J. Collazo, D. Patiño, and J. C. Morán, "A Model for the Combustion of Large Particles of Densified Wood," *Energy & Fuels*, vol. 21, no. 6, pp. 3151-3159, 2007/11/01 2007.
- [209] W. C. Park, A. Atreya, and H. Baum, *Experimental and theoretical investigation of heat and mass transfer processes during wood pyrolysis*. 2010, pp. 481-494.
- [210] S. Hu, X. Ma, Y. Lin, Z. Yu, and S. Fang, "Thermogravimetric analysis of the co-combustion of paper mill sludge and municipal solid waste," *Energy Conversion and Management*, vol. 99, pp. 112-118, 2015/07/15/ 2015.
- [211] X. Zeng *et al.*, "Assessment of char property on tar catalytic reforming in a fluidized bed reactor for adopting a two-stage gasification process," (in English), *Applied Energy*, Article vol. 248, pp. 115-125, Aug 2019.
- [212] W. Xu, L. J. Gao, H. M. Yang, G. M. Xiao, K. Q. Ding, and G. D. Wu, "Catalytic pyrolysis of distilled lemon grass over Ni-Al based oxides supported on MCM-41," (in English), *Energy Sources Part a-Recovery Utilization and Environmental Effects*, Article; Early Access.
- [213] K. Tannous, P. S. Lam, S. Sokhansanj, and J. R. Grace, "Physical properties for flow characterization of ground biomass from douglas fir wood," *Particulate Science and*

- Technology*, vol. 31, no. 3, pp. 291-300, 2013.
- [214] A. K. Burnham, *Global Chemical Kinetics of Fossil Fuels: How to Model Maturation and Pyrolysis*. Springer International Publishing, 2017.
- [215] J. Cai, W. Wu, and R. Liu, "An overview of distributed activation energy model and its application in the pyrolysis of lignocellulosic biomass," *Renewable and Sustainable Energy Reviews*, vol. 36, pp. 236-246, 2014.
- [216] B. R. Hough, D. A. C. Beck, D. T. Schwartz, and J. Pfaendtner, "Application of machine learning to pyrolysis reaction networks: Reducing model solution time to enable process optimization," *Computers and Chemical Engineering*, vol. 104, pp. 56-63, 2017.
- [217] X. Li, Q. Mei, X. Dai, and G. Ding, "Effect of anaerobic digestion on sequential pyrolysis kinetics of organic solid wastes using thermogravimetric analysis and distributed activation energy model," *Bioresource Technology*, vol. 227, pp. 297-307, 2017.
- [218] B. Stankovic, J. Jovanovic, S. Ostojic, and B. Adnadjevic, "Kinetic analysis of non-isothermal dehydration of poly(acrylic acid)-g-gelatin hydrogel using distributed activation energy model," *Journal of Thermal Analysis and Calorimetry*, vol. 129, no. 1, pp. 541-551, 2017.
- [219] Z. Dong *et al.*, "Theoretical Analysis of Double Logistic Distributed Activation Energy Model for Thermal Decomposition Kinetics of Solid Fuels," *Industrial & Engineering Chemistry Research*, vol. 57, no. 23, pp. 7817-7825, 2018.
- [220] J. Cai and R. Liu, "New distributed activation energy model: Numerical solution and application to pyrolysis kinetics of some types of biomass," *Bioresource Technology*, vol. 99, no. 8, pp. 2795-2799, 2008.
- [221] O. Kolditz, "Finite Volume Method," in *Computational Methods in Environmental Fluid Mechanics*, O. Kolditz, Ed. Berlin, Heidelberg: Springer Berlin Heidelberg, 2002, pp. 173-190.
- [222] Q. X. Huang, R. P. Wang, W. J. Li, Y. J. Tang, Y. Chi, and J. H. Yan, "Modeling and Experimental Studies of the Effects of Volume Shrinkage on the Pyrolysis of Waste Wood Sphere," *Energy & Fuels*, vol. 28, no. 10, pp. 6398-6406, 2014/10/16 2014.
- [223] A. Bhavanam and R. C. Sastry, "Kinetic study of solid waste pyrolysis using distributed activation energy model," *Bioresource Technology*, vol. 178, pp. 126-131, 2015.
- [224] A. K. Burnham, "Global kinetic analysis of complex materials," *Energy Fuels*, vol. 13, no. 1, pp. 1-22, 1999.
- [225] J. Cai, C. Jin, S. Yang, and Y. Chen, "Logistic distributed activation energy model – Part 1: Derivation and numerical parametric study," *Bioresource Technology*, vol. 102, no. 2, pp. 1556-1561, 2011.
- [226] X. Yu, M. Hassan, R. Ocone, and Y. Makkawi, "A CFD study of biomass pyrolysis in a downer reactor equipped with a novel gas–solid separator-II thermochemical performance and products," *Fuel Processing Technology*, vol. 133, pp. 51-63, 2015/05/01/ 2015.
- [227] J. Cai *et al.*, "Processing thermogravimetric analysis data for isoconversional kinetic analysis of lignocellulosic biomass pyrolysis: Case study of corn stalk," *Renewable and Sustainable Energy Reviews*, Review vol. 82, pp. 2705-2715, 2018.
- [228] H. Luo, H. Wu, W. Lin, and K. Dam-Johansen, "Heat transfer corrected isothermal model for devolatilization of thermally-thick biomass particles," Stockholm, 2017: Technical University of Denmark.
- [229] G. Gauthier *et al.*, "Pyrolysis of Thick Biomass Particles: Experimental and Kinetic Modelling," *Chemical Engineering Transactions*, vol. 23, pp. 601-606, 2013.
- [230] H. Bennadji, K. Smith, M. J. Serapiglia, and E. M. Fisher, "Effect of Particle Size on Low-Temperature Pyrolysis of Woody Biomass," *Energy & Fuels*, vol. 28, no. 12, pp. 7527-7537, 2014/12/18 2014.
- [231] G. M. Wiggins, P. N. Ciesielski, and C. S. Daw, "Low-Order Modeling of Internal Heat



- Transfer in Biomass Particle Pyrolysis," *Energy & Fuels*, vol. 30, no. 6, pp. 4960-4969, 2016/06/16 2016.
- [232] R. Paulauskas, A. Džiugys, and N. Striugas, "Experimental investigation of wood pellet swelling and shrinking during pyrolysis," *Fuel*, vol. 142, pp. 145-151, 2015.